# Spatio-Temporal Image Correlation Spectroscopy: Development and Implementation in Living Cells

Benedict Hébert
Biological Physics
Department of Physics
McGill University
Montréal, Québec
Canada

May 2006

A thesis submitted to

McGill University
in partial fulfillment of the requirements of the degree of

Doctor of Philosophy

© Benedict Hébert, 2006



Library and Archives Canada

Branch

Published Heritage

395 Wellington Street Ottawa ON K1A 0N4 Canada Bibliothèque et Archives Canada

Direction du Patrimoine de l'édition

395, rue Wellington Ottawa ON K1A 0N4 Canada

> Your file Votre référence ISBN: 978-0-494-27788-1 Our file Notre référence ISBN: 978-0-494-27788-1

#### NOTICE:

The author has granted a non-exclusive license allowing Library and Archives Canada to reproduce, publish, archive, preserve, conserve, communicate to the public by telecommunication or on the Internet, loan, distribute and sell theses worldwide, for commercial or non-commercial purposes, in microform, paper, electronic and/or any other formats.

#### AVIS:

L'auteur a accordé une licence non exclusive permettant à la Bibliothèque et Archives Canada de reproduire, publier, archiver, sauvegarder, conserver, transmettre au public par télécommunication ou par l'Internet, prêter, distribuer et vendre des thèses partout dans le monde, à des fins commerciales ou autres, sur support microforme, papier, électronique et/ou autres formats.

The author retains copyright ownership and moral rights in this thesis. Neither the thesis nor substantial extracts from it may be printed or otherwise reproduced without the author's permission.

L'auteur conserve la propriété du droit d'auteur et des droits moraux qui protège cette thèse. Ni la thèse ni des extraits substantiels de celle-ci ne doivent être imprimés ou autrement reproduits sans son autorisation.

In compliance with the Canadian Privacy Act some supporting forms may have been removed from this thesis.

While these forms may be included in the document page count, their removal does not represent any loss of content from the thesis.

Conformément à la loi canadienne sur la protection de la vie privée, quelques formulaires secondaires ont été enlevés de cette thèse.

Bien que ces formulaires aient inclus dans la pagination, il n'y aura aucun contenu manquant.



a ma mère sans qui cette thèse n'aurait jamais existé moi non plus, d'ailleurs.

#### Abstract

The object of this thesis is to develop a new extension of Image Correlation Spectroscopy (ICS) that can measure velocity vectors for flowing protein populations in living cells. This new technique, called Spatio-Temporal Image Correlation Spectroscopy (STICS), allows measurement of both diffusion coefficients and velocity vectors (magnitude and direction) from fluorescence microscopy image time series of fluorescently labeled cellular proteins via monitoring of the time evolution of the full space-time correlation function of the intensity fluctuations. By using filtering in Fourier space to remove frequencies associated with immobile or slow components, it is possible to measure the protein transport even in the presence of a large fraction of immobile species that are static in the image series. The STICS method can generate complete transport maps of proteins within subregions of the basal membrane even if the protein concentration is too high to perform single particle tracking measurements, and it can be applied to any type of fluorescence microscopy image time series. This thesis presents the background theory, computer simulations, and analysis of measurements on fluorescent microspheres and fixed cell samples to demonstrate proof of principle, capabilities, and limitations of the method. Visible fluorescent proteins (VFPs) were used to label a variety of the proteins involved in cell-to-extracellular-matrix adhesions, including focal adhesion kinase, paxillin,  $\alpha$ -actinin,  $\alpha$ 5-integrin, talin, vinculin and actin. Various fusion protein pairs were transfected in living cells and imaged using both laser scanning microscopy and total internal reflection microscopes. Using STICS analysis, co-transport maps of proteins were generated within protruding sub-regions of the basal membrane. The new space time image correlation method can probe the mechanistic details of the hypothesized molecular clutch that regulates the extra cellular matrix/cytoskeletal interactions during migration. The technique was also applied to mapping fluid flow in migrating keratocytes in order to elucidate the role that fluid flow plays in migrating cells.

#### Résumé

L'objet de cette thèse est de développer une nouvelle extension de la spectroscopie par corrélation d'images (ICS) qui peut mesurer les vecteurs vitesse de flux de protéines dans des cellules vivantes. Cette nouvelle technique, appelée spectroscopie spatio-temporelle par corrélation d'images (STICS), permet la détermination des coefficients de diffusion et des vecteurs vitesse (grandeur et direction) à partir de séries d'images de microscopie par fluorescence, en suivant l'évolution temporelle des corrélations spatiales des fluctuations d'intensités. En filtrant dans l'espace de Fourier les fréquences associées aux composantes immobiles ou lentes, il est possible de mesurer le transport des protéines même en présence d'un grand pourcentage d'espèces immobiles qui sont statiques dans la série d'images. La méthode STICS peut générer une cartographie complète du transport des protéines dans la membrane basale, même quand la densité de protéines est trop grande pour y performer des mesure par suivi de particule unique. De plus cette méthode peut être appliquée à tout type de microscopie par fluorescence. Cette thèse présente la théorie sous-jacente à STICS, des simulations par ordinateur, et l'analyse d'expériences avec des microsphères fluorescentes et des échantillons de cellules fixées pour démontrer la preuve de principe, les capacités et les limitations de cette méthode. Des protéines fluorescentes visibles ont été utilisées pour marquer diverses protéines impliquées dans le lien entre la matrice extra cellulaire et le cytosquelette d'actine, incluant la kinase d'adhésion focale, la paxilline, l' $\alpha$ -actinine, l' $\alpha$ 5-integrine, la taline, la vinculine et l'actine. Ces paires de protéines ont été transfectées dans des cellules vivantes et imagée avec des microscopes a balayage laser et des microscopes à réflexion totale interne. En utilisant l'analyse STICS, des cartes de co-transport de ces protéines ont été générées pour des zones de protrusion dans la membrane basale. Cette nouvelle méthode de corrélation spatio-temporelle d'images peut questionner les détails mécanistique de l'hypothétique embrayage moléculaire qui régularise les interactions entre la matrice extra cellulaire et le cytosquelette pendant la migration des cellules. La technique a aussi été appliquée a la cartographie de flux de fluide a l'intérieur de keratocytes migrants, afin d'élucider le rôle que joue le flux de fluide dans la migration des cellules.

## Contents

A	bstra	ct	i
$\mathbf{R}$	ésum	é	įi
Ta	able (	of Contents	v
Li	st of	Figures	X
Li	st of	Tables	i
St	aten	nent of Originality xi	ii
A	ckno	wledgements xvi	ίi
1	Intr	oduction	1
	1.1	Motivation	1
	1.2		3
	1.3		5
	1.4		8
			9
		1.4.2 Semiconductor Nanocrystals	
	1.5	Current Image Analysis Methods	
		1.5.1 Fluorescence Recovery After Photobleaching 1	
		1.5.2 Single Particle Tracking	
		1.5.3 Optical Flow	9
		1.5.4 Fluorescent Speckle Microscopy	1
	1.6	Spatio Temporal Image Correlation Spectroscopy 2	3
2	The	ory 28	5
	2.1	Introduction	5
	2.2	Fluorescence and Jabloński Energy Diagrams	6
	2.3	Fluorescence Microscopy	8
		2.3.1 General Microscope Instrumentation	8
		2.3.2 Wide Field Fluorescence	
		2.3.3 Laser scanning microscopy	

		2.3.4 Total Internal Reflection Microscopy	35
	2.4	Fluorescence Correlation Spectroscopy	
	2.5	Image Correlation Spectroscopy	
		2.5.1 Generalized Spatio-Temporal Correlation Function	
		2.5.2 Spatial Correlation and Cross-Correlation	43
		2.5.3 Temporal Correlation and Cross-Correlation	44
		2.5.4 Decay Models for Correlation Functions	45
	2.6	Space-Time Image Correlation Spectroscopy	47
	2.7	Immobile Population Removal in STICS Analysis	52
		2.7.1 Zero Frequency Filtering	53
		2.7.2 Windowed Average Filtering	53
	2.8	Chapter Conclusions	56
3	Mat	terials and Methods	59
	3.1	Microscopy Instrumentation	59
		3.1.1 Wide Field Fluorescence Microscopy	59
		3.1.2 Confocal Microscopy	59
		3.1.3 Two-Photon Microscopy	60
		3.1.4 Total Internal Reflection Microscopy	61
	3.2	Image Auto-Correlation and Cross-Correlation Analysis	63
	3.3	Cell Culture	63
		3.3.1 Plasmids	63
		3.3.2 Cell culture of the 3T3, MEF and CHO lines	64
		3.3.3 Keratocyte cell culture	65
	3.4	Computer Simulations	66
	3.5	Vector Flow Fields Comparison for Two Population Measure-	
		ments	70
	3.6	Chapter Conclusion	73
4	In S	Silico Characterization	75
	4.1	Introduction	75
	4.2	STICS characterization	76
		4.2.1 Photobleaching	76
		4.2.2 Sampling and Signal to Noise Considerations	80
	4.3	Immobile Filtering Characterization	84
		4.3.1 Immobile Population Filtering Artifacts	85
		4.3.2 Dynamic Range of Immobile Filtering	91

		4.3.3	Window Filtering Correction for ICS	
		4.3.4	Window Filtering and STICS	
	4.4	Chapt	er Conclusion	. 103
5	In S	Situ Ch	naracterization	105
	5.1	Introd	$\operatorname{uction}$	. 105
	5.2	Image	treatment	. 106
		5.2.1	Noise and Immobile Population Removal	. 106
		5.2.2	Drift Correction	. 109
	5.3	STICS	Applied to Cells	. 112
		5.3.1	Fixed Controls	
		5.3.2	Diffusion, Non Directed Flow and Directed Flow in	
			Living Cells	. 115
	5.4	STICO	CS Applied to cells	. 121
		5.4.1	Fluorescent Microsphere Control Experiments	. 121
		5.4.2	STICCS Measurement of Concerted Flow of Labeled	
			Proteins in Cells	. 125
	5.5	Chapte	er Conclusion	. 127
6	Vel	ocity N	Sapping applications in living cells	129
		•		100
	6.1	The M	lolecular Clutch	. 129
	6.1	The M 6.1.1	Iolecular Clutch	
	6.1			. 129
	6.1	6.1.1	Cell Adhesion Mechanisms	. 129 . 132
	6.1	6.1.1 6.1.2	Cell Adhesion Mechanisms	<ul><li>. 129</li><li>. 132</li><li>. 135</li></ul>
	6.1	6.1.1 6.1.2 6.1.3	Cell Adhesion Mechanisms	<ul><li>. 129</li><li>. 132</li><li>. 135</li><li>. 138</li></ul>
	6.1	6.1.1 6.1.2 6.1.3 6.1.4 6.1.5	Cell Adhesion Mechanisms	<ul><li>. 129</li><li>. 132</li><li>. 135</li><li>. 138</li><li>. 144</li></ul>
		6.1.1 6.1.2 6.1.3 6.1.4 6.1.5	Cell Adhesion Mechanisms	<ul><li>. 129</li><li>. 132</li><li>. 135</li><li>. 138</li><li>. 144</li><li>. 147</li><li>. 147</li></ul>
		6.1.1 6.1.2 6.1.3 6.1.4 6.1.5 Fluid	Cell Adhesion Mechanisms	<ul><li>. 129</li><li>. 132</li><li>. 135</li><li>. 138</li><li>. 144</li><li>. 147</li><li>. 148</li></ul>
		6.1.1 6.1.2 6.1.3 6.1.4 6.1.5 Fluid 1 6.2.1 6.2.2 6.2.3	Cell Adhesion Mechanisms	. 129 . 132 . 135 . 138 . 144 . 147 . 148 . 153
		6.1.1 6.1.2 6.1.3 6.1.4 6.1.5 Fluid 1 6.2.1 6.2.2 6.2.3	Cell Adhesion Mechanisms	. 129 . 135 . 135 . 144 . 147 . 147 . 148
7	6.2	6.1.1 6.1.2 6.1.3 6.1.4 6.1.5 Fluid 1 6.2.1 6.2.2 6.2.3 Chapte	Cell Adhesion Mechanisms	. 129 . 135 . 135 . 144 . 147 . 147 . 148
7	6.2 6.3 Con	6.1.1 6.1.2 6.1.3 6.1.4 6.1.5 Fluid 1 6.2.1 6.2.2 6.2.3 Chapte	Cell Adhesion Mechanisms	. 129 . 132 . 135 . 138 . 144 . 147 . 148 . 153 . 156

# List of Figures

1.1	Current cell migration paradigm
1.2	Molecular players involved in cell migration 6
1.3	The fluid mosaic model
1.4	GFP structure
1.5	Transfection scheme
1.6	Example of FRAP data
1.7	Example of single particle tracking data
2.1	Jabloński Diagram
2.2	Alexa dye spectra
2.3	Optical microscope schematic
2.4	Imaging plane in wide field microscopy
2.5	Light pathway in confocal microscopy
2.6	Total Internal Reflection Microscopy
2.7	Schematic diagram of the fluorescence correlation spectroscopy
	method
2.8	STICS correlation function examples
2.9	STICS algorithm
3.1	Construction of simulation images 69
3.2	Example of flow field scoring
4.1	Photobleaching effects on ICS
4.2	Photobleaching effects on STICS
4.3	Simulated images with varying signal to noise 80
4.4	STICS characterization
4.5	Immobile population filtering example 84
4.6	Effects of immobile filtering on $r'_{ab}(\xi, \eta, \Delta t)$
4.7	Effects of immobile filtering with varying diffusion 89
4.8	Example of signal and noise generation 95
4.9	Autocorrelation curves for windowed immobile filtering 96
4.10	Recovered diffusion with window immobile filtering 99
4.11	Effects of window filtering on STICS velocities
5.1	Example of white noise correction
5.2	In situ immobile population removal
5.3	Drift correction
5.4	Fixed cells control analysis
5.5	Fixed cells photobleaching curves
5.6	Regions of interest for STICS analysis in vivo

5.7	STICS analysis on a diffusive population
5.8	STICS analysis on a non-directional population 119
5.9	STICS analysis on a directional population
5.10	STICCS on fluorescent microspheres
5.11	Fluid flow field comparison
6.1	$\alpha$ -actinin velocity mapping and analysis
6.2	Co-velocity maps before and after perturbation
6.3	Analysis of co-velocity maps before and after perturbation $$ 137
6.4	Co-velocity mapping of adhesion proteins
6.5	Analysis of co-velocity maps of adhesion proteins
6.6	Paxillin/ $\alpha$ -actinin velocity map
6.7	Two-level clutch model
6.8	STICS fluid flow maps in keratocytes
6.9	Parallel retrograde fluid flow as a function of cell speed $\dots$ 151
6.10	Perpendicular retrograde fluid flow as a function of cell rota-
	tional speed
6.11	Diagramatic physical model of fluid flow

## List of Tables

3.1	Adjustable computer simulation parameters	67
4.1	STICS performance with no immobile fraction	83
4.2	STICS performance with an immobile fraction	93
4.3	Window immobile filtering characterization results	100
4.4	Effects of window filtering on STICS velocities	102
5.1	STICS analysis of microspheres, original populations	124
5.2	STICS analysis of microspheres, interacting populations	124

## Statement of Originality

The author claims the following aspects of the thesis constitute original scholarship and an advancement of knowledge. Some of these findings have been published [1, 2].

- 1. The design, development, characterization and live cell implementation of a new fluorescence microscopy based biophysical method called spatio-temporal image correlation spectroscopy (STICS) for extracting velocities of labeled proteins inside cells. The STICS approach is based on spatial and temporal correlation analysis of intensity fluctuations within a time series acquired via fluorescence microscopy imaging of a sample. The following points detail the major advantages of the novel STICS technique.
  - This method has relatively high spatial mapping resolution and can be used to analyze microscopy image sub-regions that are as small as 16×16 pixels. It also has the advantage that it is computationally fast compared to related techniques such as Fluorescent Speckle Microscopy: a single region of interest of 16×16 pixels and 200 images is analyzed in under 3 seconds.
  - The STICS technique is also very adaptable since it can be applied to virtually any fluorescence microscope image time series. It has the ability to map protein velocities in cells that are simply transfected with any type of fluorescently labeled macromolecule and does not require overly sophisticated sample preparation or computer hardware (it is PC based).
  - Most importantly it can accurately measure protein translational motions under conditions of very high protein densities, such as in adhesions or along actin filaments in cells, or at very low protein densities where the distribution of labeled macromolecules is

homogeneous and diffuse, and no directed flow is apparent to the eye upon viewing the image series.

- 2. The design and characterization of a novel filtering technique intended to remove the immobile protein population fraction intensity contribution from the space-time correlation function.
  - This filtering in Fourier space can remove the intensity contributions from the fully static (zero frequency) or slowly moving (low frequency) labeled protein population by adjustment of the filter window size.
  - The filtering also removes long range spatial correlations from the images. This is especially useful in cases where the protein density is high and they are located in large spatially extended structures, such as in adhesions or along actin filaments. Such extended cellular structures that are larger than the optical diffraction limit can cause deviations in the STICS analysis if they are not filtered.
- 3. The first study of the actin-integrin linkage in the lamella of living cells by using STICS to measure velocity maps of integrin, actin, and adhesion related proteins.
  - Measurements of flow velocities for a number of adhesion components ( $\alpha$ 5-integrin,  $\alpha$ -actinin, paxillin, FAX, talin and vinculin) were compared with those measured for actin to identify which proteins within the linkage are potential sites of regulation via transient decoupling or slippage.
  - Experimental determination that actin polymerization is not a determining factor in the regulation of the  $\alpha$ -actinin-actin linkage. On the other hand, myosin II generated tension in the actin cables was implicated in regulation of the actin- $\alpha$ -actinin interactions.

- Experimental determination that there exists a linkage complex in migratory cells, comprising: vinculin, talin, paxillin and focal adhesion kinase (and possibly other proteins). This linkage complex links the integrin to the actin cytoskeleton in a dynamic manner, with the STICS experiments suggesting that it is connected to the actin 70% of the time, and to the integrins 30% of the time.
- 4. The first measurements of cytosolic fluid flow through the dense actin meshwork in the lamellipodium of migrating keratocyte cells.
  - Experimental determination that an overall rearward fluid flow exists in the cell frame of reference during migration with water influx at the leading edge, consistent with the localization of aquaporin channels at the leading edge.
  - Novel measurements of fluid flow velocities in a large population of cells using various markers (655 nm  $\lambda$  and 545 nm  $\lambda$  quantum dots, as well as green fluorescent protein) that consistently show that this retrograde fluid flow is approximately one third of the cell migration speed in all cases studied.
  - Biophysical modeling of the fluid flow in the lamella shows that water influx at the leading edge partially relieves the membrane load, leading to an increase in the rate of actin protrusion.

The complexity of trying to unravel the quantitative details of the molecular basis of cell migration entails cross-disciplinary collaborators. Some of the measurements presented in this thesis were done in the context of a larger collaborative scientific effort involving physicists, chemists, cell biologists and theorists from McGill University, University of Virginia, Stanford University and University of California Davis. Essential procedures in this thesis not performed by the author are the following.

- 1. Keratocyte cell culture preparation, quantum dot loading and imaging for the experiments in Chapter 6, for which the procedure was presented in section 3.3.3. Prepared and imaged by Dr. Kinneret Keren, Department of Biochemistry, Stanford University (California, USA).
- 2. Preparation and imaging of the CHO cells analyzed in section 5.3.2. Prepared and imaged by Dr. Paul Wiseman, Department of Physics and Chemistry, McGill University (Quebec, Canada).
- 3. Preparation and imaging of the cells analyzed in section 6.1 was done jointly by the author and Dr. Claire Brown, Department of Cell Biology, University of Virginia (Virginia, USA).
- 4. The biophysical fluid flow model in section 6.2.3 was developed by Dr. Alex Mogilner, Department of Mathematics and Center for Genetics and Development University of California Davis (California, USA). It was applied to the experimental findings of this thesis as part of a collaborative effort.

## Acknowledgements

Acknowledgements are underrated. They are the most important part of this thesis. Without the constant help and moral support of the fabulous group of people listed below, I would never have made it through. Never.

First, due thanks to my supervisor: Prof. Paul W. Wiseman, for being the angel on my shoulder, while I was being the devil on his. For the Captain Morgan special memories and the Zoolander looks. For the great scientific advisor he has been. I wouldn't have gone very far without him. I thank him for being human first and foremost.

I want to acknowledge the numerous collaborators who have helped during this journey. Dr. Claire Brown and Prof. Rick Horwitz at the University of Virginia, for accepting me into their lab on numerous occasion, and for being my patient cell biology teachers. I also want to thank Dr. Kinneret Keren and Prof. Julie Theriot of Stanford University, and Prof. Ido Braslavsky for suggesting and initiating the scientific encounter with Kinneret. At McGill University, nothing would get done without the extraordinary support staff in the physics department: Paula, Sonia, Louise, Diane and Elizabeth. They are the best team of grad student stress relief. I also want to thank Michel for being so much fun in the student labs.

I want to acknowledge the moral support of my family, especially my mother. Although my mother cannot perform a simple proportionality rule by herself, she has certainly been a great advice giver when things weren't going as planned. Thanks for being such a model of perseverance. I also thank my sisters for being so fresh and reminding of how simple things are when you think they're over-complicated.

Someone very close to my heart that I wish to thank is Mireille. Although we've had our share of adverse circumstances, she's been with me through the good and the bad times; she's been a listening ear and the best friend I could have asked for. Thank you.

Of course I cannot thank enough the Wiseman lab members, past and present, for their advice, help, and just plain fun, especially at conferences... In no particular order: Jon "Beslislele" Belisle, Antoine "wrong day" Godin, Santiago "el latin lover" Costantino, Richard "Dr" Naud, Alexia "Ben you scare me" Bachir, Nela "the female member" Durisic, Katrin "the nice german" Heinze, Chris "I am clinically insane" McQuinn, David "summer student" Kolin, Elvis "has left the building" Pandzic, Jon "comou" Comeau, Mikhails "Russian mafia" Sergeyev, Stephanie "do you like Ligers?" Wong, Charles "I should've been born in the 18th century" DeLannoy...

There are many other friends/family/colleagues/random encounters that touched my life during the years I spend at McGill. They include: Mathieu, Simon bad boy, Simon Kentuck, Val et leur petite Eloise, Martin, Julien, Annie Lepitre, Marco, Nic, Genevieve, Jess, Anna Maria, Oli scout, Alex, Catou, JF, Annie Lec, Oli Leblond, Maxence. My office mate Jens. My next door office neighbors Rene, Kelsey and Marjorie. Chris the procrastinator. My uncle and physicist Jean-Claude, for his precious advice of coming to McGill to work with Paul. There are probably many other friends and colleagues that I am forgetting about here. You know who you are, and if you're not sure, come and ask me.

Finally, I want to thank Madame Jalabert. The teacher without whom I would not be here today. I did this because of you.

Thank you all.

Spatio-Temporal Image Correlation Spectroscopy: Development and Implementation in Living Cells

### 1 Introduction

#### 1.1 Motivation

"If you try to take a cat apart to see how it works, the first thing you have in your hands is a nonworking cat."

Douglas Adams

Reductionism, or the study of a system by taking it apart and seeing how its individual components work, has been a dominant approach that has lead to many important advances in the physical and biological sciences in the modern era. Some of the intellectual threads in classical physics that are important in quantitative applications to biology include statistical mechanics, kinetic theory, hydrodynamics, continuum mechanics, nonlinear dynamics and colloidal physics. However, reductionist techniques study the parts, rather than the whole. The process of taking the system apart via a reductionist approach can be misleading especially in the extremely complex and interconnected milieu of biological cells. A current theme in biophysics is to be able to quantitatively measure processes directly inside the cell (in situ). New physical techniques such as those involving micromanipulation (e.g. optical traps), microlithography (to create structured environments) and fluorescence methods (for direct visualization of biomacromolecules and their biochemistry) all play an important role in getting physical insights from in vivo measurements. An important question to ask is: "what can

1.1 Motivation 2

physicists bring to this field?" An interesting parallel can be drawn with the symbiotic relationship that mathematics and physics have enjoyed for centuries. Just as physics flourished when it was endowed with the powerful abstract tools of mathematics, so can biology evolve into a more quantitative science using both the technological advances and the modeling innovations that physics has developed in the past decades, provided that the "bio" in biophysics is not forgotten.

Developments in both theoretical and experimental biophysics have led to giant leaps forward in the understanding of protein structure, bioenergetics, ion transport, transmembrane protein transport and much more. It is not productive for physicists to move into biology simply to copy the existing methods and adopt the current paradigms of the biologists. They must bring something new to the table. The importance of developing and characterizing new techniques that can give quantitative information on particular systems cannot be overemphasized, since the tools that have been used and that are being created provide powerful methods for scientists to conduct quantitative experiments with intact biological systems. The object of this thesis is the development of a new biophysical technique called spatio-temporal image correlation spectroscopy (STICS) and its application for measuring protein transport which is necessary to understand the molecular basis of cell migration.

#### 1.2 The Challenge: Cell Migration

Many types of animal cells have the ability to migrate by following chemical or mechanical cues. These displacements often play a fundamental role in both normal or pathological cases, i.e. morphogenesis or cancer metastasis [3]. Certain types of cells are even specialized in locomotion, such as immune system neutrophils or fish epidermal keratocytes [4, 5, 6]. The basic paradigm of cellular migration is illustrated in Figure 1.1. The cell extends membrane protrusions which can be either flat and large (lamellar protrusions) or thin and tubular-like (fillipodial protrusions) [7]. These protrusions help cells probe their environment, and acquire a spatial asymmetry enabling them to select a given direction of migration [8]. After these protrusions are sent out from the cell periphery, they form attachments to the substrate called focal contacts through a variety of proteins that will be described in detail in the next section [9]. Some of these attachment points will mature into more stable, solid adhesions through which the cell can turn intracellularly generated contractile forces into net cell body translocation [10]. These contractile forces come from the myosin molecular motors, which bind to the polymeric actin cytoskeleton filaments inside the cell.

The cytoskeleton is a cellular "scaffolding" or "skeleton" found in the cytoplasm inside cells and has three major fiber types: microfilaments made of actin protein, intermediate filaments made of various kinds of proteins (e.g. keratin), and microtubules made of tubulin [11]. The three fiber types serve different functions. Actin filaments are often associated with changes in cell size and morphology, contractility such as in muscle cells, and cell division,

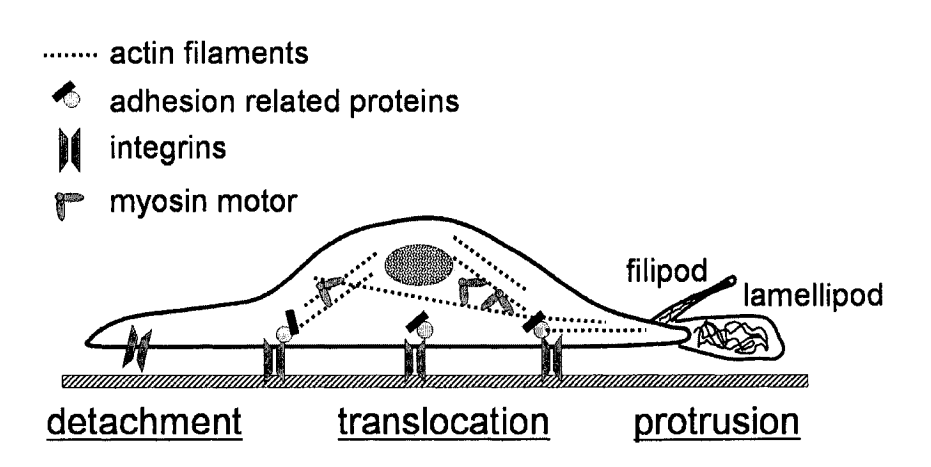


Figure 1.1: Illustration of the current cell migration paradigm. As a first step, the cell extends membrane protrusions (lamellipods or fillipods), which anchor to the extra-cellular matrix (ECM) through a variety of adhesion related molecules that link the actin cytoskeleton to the transmembrane integrins. The integrins in turn bind to the ECM. The myosin motors which connect to the actin filaments can subsequently exert traction forces and pull the cell body forward as adhesions at the rear of the cell are disassembled. Adapted from [3].

growth and motility [12]. The microtubules are major filaments for internal transport and movement of chromosomes and organelles during cell division [13]. Intermediate filaments contribute to flexibility, elasticity, and stiffness of cells and tissues [14]. Microtubules are straight, hollow cylinders with a diameter of about 25 nm composed of long chains of the proteins  $\alpha$  and  $\beta$  tubulin [15]. Actin filaments are made from monomers of one basic protein subunit, i.e. by the polymerization of F-actin monomers. Actin filaments are about 8 nm in diameter [16], and they can bundle together with myosin in what are called "stress fibers". To migrate, the cell basically anchors the actin filaments and stress fibers to adhesion sites and "tugs" forward by pulling on the actin bundles with the myosin motors [17].

As recent studies have shown, the molecular partners involved in all of the steps of cellular migration are numerous and their interactions very complex [3]. Cell migration is a dynamic, integrated process that is coordinated both spatially and temporally. Although numerous components are known to interact before, during and after the formation of focal contacts and adhesions, less is known about the exact timing, the number of components and transport mechanisms involved in these interactions. Understanding the complex physical and chemical integration of kinetic, kinematic and mechanical processes requires specialized mathematical models and analysis methods, some of which are only in their infancy. There is a great need for quantitative biophysical techniques which can reveal important quantitative aspects of the physico-chemical molecular mechanisms that govern cell migration [3].

## 1.3 Spatio-Temporal Interactions

At the cellular level, there are three main regions where the molecular partners that play a role in cell migration are located [figure 1.2]. First is the extracellular matrix (ECM), a protein rich environment outside the cell to which all cell attachments are anchored. The ECM interacts with the basal (lower) membrane of the cell (in a 2D tissue culture context). The ECM is made of many types of large glycoproteins including fibronectin, vitronectin, collagen, laminin and tenascin [18]. The second level consists of the transmembrane proteins which are found in the cell membrane and act as the link between the extra- and intra-cellular environments. Integrins are the major transmembrane proteins that cluster to form focal contacts and focal adhesions [19]. Integrins form a functional dimer of an  $\alpha$  and  $\beta$  subunit of

which there are many different subforms that are characteristic of different cells and tissues. Integrins bind to extra cellular matrix components such as fibronectin and to intracellular cytoskeletal linker proteins such as talin or  $\alpha$ -actinin. These linker molecules make up the third level of molecular partners involved in cell migration. They are termed adhesion related proteins because they are part of the linkage between the integrins and the actin cytoskeleton. They are numerous, but some of the key actors are signalling molecules such as focal adhesion kinase (FAK) and paxillin, as well as mechanical linkers such as talin, vinculin and  $\alpha$ -actinin [3, 20].

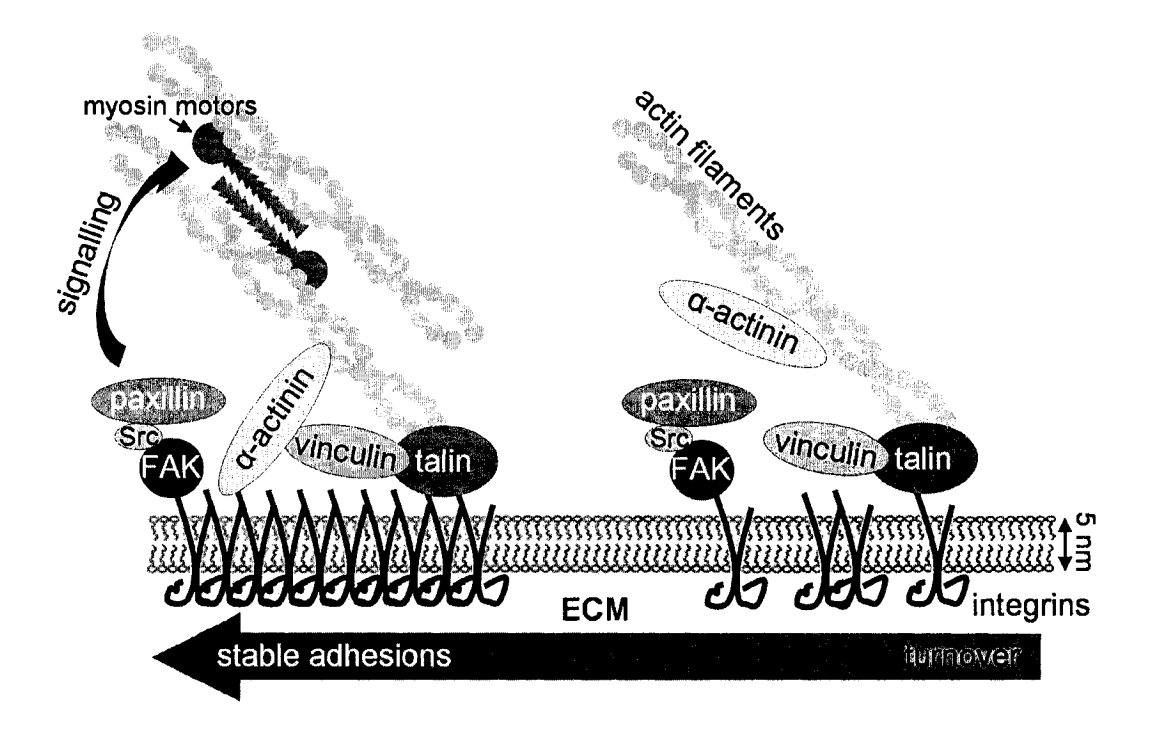


Figure 1.2: Illustration of the maturation of nascent adhesions via clustering of membrane integrins and recruitment of linker proteins into more stable complexes. Some of the major molecular players involved in linking the cytoskeleton to the extracellular matrix are the linkage proteins (integrin, α-actinin, talin, vinculin) and the signalling molecules (FAK, paxillin). Adapted from [20].

Moreover, these interactions evolve in space and time in a migrating cell: adhesions assemble and disassemble in response to extracellular cues, and mature as the actin-ECM bond is strengthened. Recycled or newly synthesized integrins are inserted into the membrane at the leading edge, where they can form bonds with the substratum ECM ligands in what are called "nascent adhesions" [20] (see Figure 1.2). As the cell crawls over them, the nascent adhesions start to mature and grow by recruiting additional molecular components. They can also disassemble to recycle components to newly formed nascent adhesions at the cell's leading edge [21]. The molecular mechanisms of maturation or disassembly of adhesion complexes are still unclear, but involve signalling from adhesion related molecules such as FAK, paxillin, Src and others [20]. Adhesions that have matured will also eventually disassemble at the rear of the migrating cell, as ripping release and detachment of the membrane occur [22].

This asymmetry at the molecular level, whereby different proteins are found at distinct locations in the cell body to serve different purposes, posits several questions. How does the cell regulate such asymmetry, and by what mechanisms does it replenish components at the leading edge? What is the order of assembly? Is the transport of components due to Brownian diffusion, anomalous diffusion (i.e. diffusion with obstacles or confined diffusion, see Figure 1.3) or directed transport (e.g. by myosin motors along actin filaments)? One important problem here is characterizing the motion and interactions of membrane proteins, extra cellular matrix components and intra cellular messengers involved in the regulation of cell migration at the

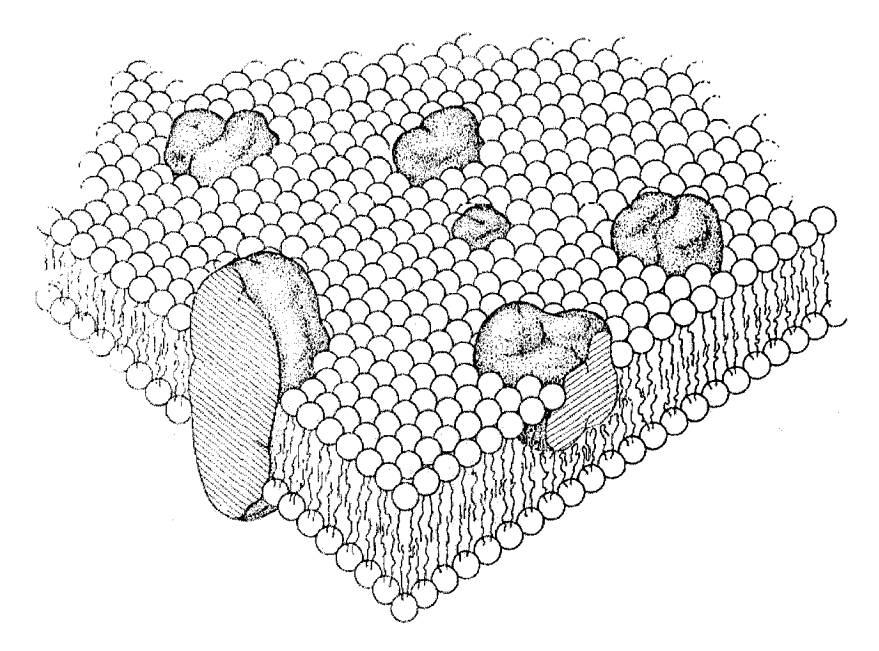


Figure 1.3: The original fluid mosaic model as envisaged by Singer et al. [23]. The fluid lipid bilayer membrane is punctuated by integral membrane proteins which are randomly distributed but are diffusively mobile and can aggregate. These can be obstacles to free diffusion.

molecular level. The next section will describe the means and methods of investigating these transport mechanisms.

## 1.4 Fluorescence Imaging

Optical microscopies, and fluorescence microscopy in particular, have been among the most important techniques developed for *in vivo* studies of living cells. Fluorescent probes are amazingly useful for biological research, because they allow the study of the inner workings of cells with single molecule detection sensitivity and high specificity. The trick is to attach the fluorescent label to the macromolecule you are interested in studying. Researchers have developed several ways to fluorescently label macromolecules for live or fixed cell imaging including many types of fluorescent organic dyes that can be

attached to antibodies for tagging purposes. More recently developed approaches use fluorescent probes that are either naturally fluorescent proteins or semi-conductor nanocrystals (quantum dots) [24, 25].

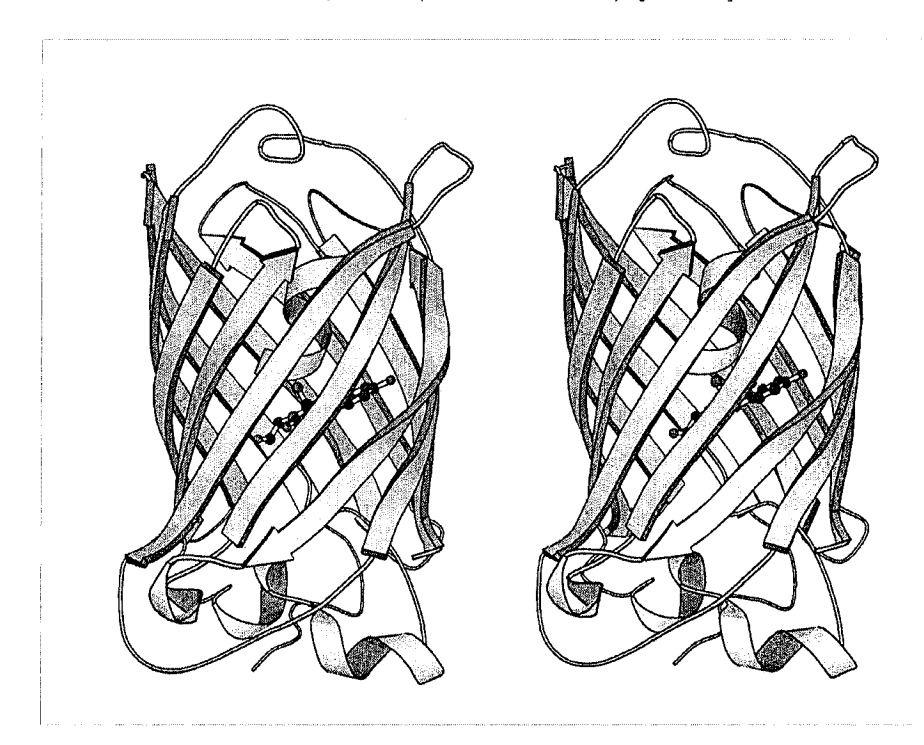


Figure 1.4: Stereoview of the structure of green fluorescent protein (GFP) [26]. Shown as arrows are 11 antiparallel  $\beta$ -strands which form the beta-can. Inside this beta-structure there is an alpha-helix (curly ribbon), in the middle of which is the chromophore (detailed ball and stick molecular structure). GFP is roughly  $4\times 3$  nm (L×W) in size.

#### 1.4.1 Fluorescent proteins

There are several kinds of naturally fluorescent proteins that are used to label macromolecules, each with its own absorption and emission spectra, quantum yield and fluorescence lifetimes. The most commonly used naturally fluorescent protein is the green fluorescent protein (GFP, see Figure 1.4). GFP is naturally found in a jellyfish (Aequorea victoria [27]) that lives in

the cold waters of the Pacific off Washington state. The jellyfish contains a bioluminescent protein, aequorin, that emits blue light. The green fluorescent protein converts this light to green light, which is what we actually see when the jellyfish lights up. The cloning of the gene that encodes GFP was a breakthrough for live cell imaging because it became possible to genetically splice the GFP codon within the genetic codes for other proteins [28] and thus have the cell synthesize the protein of interest with an attached GFP fluorescent marker (see next paragraph). Since its discovery, many mutants of GFP have been created that fluoresce at different wavelengths including the yellow fluorescent protein (YFP) and cyan fluorescent protein (CFP) [29].

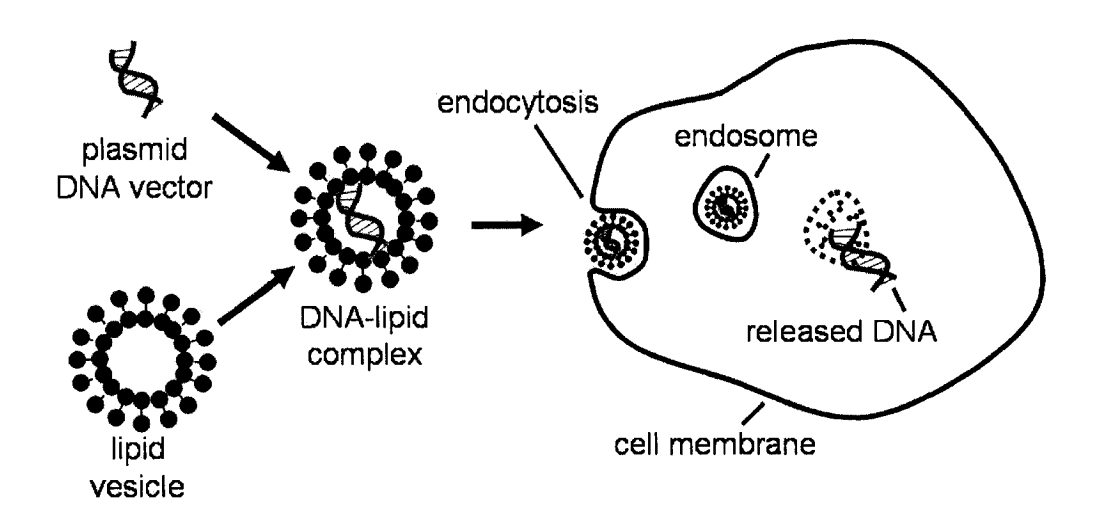


Figure 1.5: Transfection of a plasmid in a mammalian cell. The plasmid DNA vector is placed inside a lipid vesicle, which is in turn fuses with the cell membrane and is taken into the cell by endocytosis. The endosomes are eventually degraded in the cell and the DNA can now be used by the replication and transcription machinery in the nucleus to express the protein of interest.

To attach these fluorescent proteins to the molecule of interest, i.e. to splice the fluorescent protein codon into the genetic code of another protein, the genetic technique of choice is called transfection [30]. Transfection involves cellular insertion of a DNA plasmid (essentially a circular loop of DNA) that carries the genetic code for the protein of interest immediately followed by the genetic code for the fluorescent protein (see Figure.1.5). Hence when this new DNA is incorporated into the nucleus of the cell and the cell starts its transcription, it will produce the native protein fused to the fluorescent protein, effectively generating a protein with a built in fluorescent tag. Advantages of this method include the fact that it is the cellular machinery that does all the work in expressing the fluorescent probe, which eliminates the need for extrinsic labeling steps. Additionally, any kind of protein (internal or transmembrane) can be labeled in this way, but control experiments need to be carried out in order to determine if the natural function of the labeled protein is unaffected by the attached fluorescent protein.

However, organic dyes and GFP also have a few drawbacks. They are susceptible to photobleaching and can only undergo a finite number of excitation/emission cycles [31]. This means that a single GFP cannot be observed for more than a few tens of seconds when imaged with a light microscope under typical imaging settings (however this depends heavily on laser power and the chemical environment [32]). After a certain number of cycles, the fluorescent molecules undergo irreversible photobleaching, thus entering a dark state (a non-fluorescent state) [33]. Moreover, organic dyes often have broad absorption or emission spectra, making it difficult to excite a single dye if you have several fluorescent markers present in the cell, or making it

difficult to separate the emission signal from two different dyes when their spectra overlap [34]. The next section deals with a potential solution to these problems.

#### 1.4.2 Semiconductor Nanocrystals

Semiconductor nanocrystals, more commonly called quantum dots (QDs), have emerged as an interesting alternative to classical fluorescent probes [35]. They are (usually) spherically-shaped, nanometer-sized semiconductor nanocrystals. The optical properties of QDs are dramatically different than the bulk material because at the nanometer size scale, the QD behaves like a potential well that confines electrons in three dimensions to a region on the order of the electrons' de Broglie wavelength in size [36]. An electron-hole pair can be excited in the core of a quantum dot by photon absorption and when they recombine, they emit light (fluoresce). The fluorescence emission spectrum is narrow and symmetric and the wavelength depends directly on the size of the crystal: the larger the QD, the longer the wavelength of the emitted light [37]. As the dots shrink in size, the emitted light becomes shorter in wavelength, moving toward the blue.

The main advantage of quantum dots is their photostability, which means that they do not undergo irreversible photobleaching when illuminated with laser light (at reasonable laser powers), in contrast to organic dyes and GFP [38]. Single dots have been observed for times of up to several hours [39] and they have a low cytotoxicity (most reports do not find effects on cell viability, morphology, function, or development over the duration of the experiments). However they also have a main drawback: quantum dots exhibit fluorescence

intermittency [40]. This on and off "blinking" phenomenon can significantly impair the ability to track single quantum dots over extended periods of time. The characteristics of the blinking vary significantly depending on the environment of the quantum dot, and recent studies have shown that blinking is not strong in live cell experiments [35] but can severely affect any intensity fluctuation analysis [41].

Semiconductor quantum dots have to be chemically functionalized in order to make them hydrophilic [42], and they have to be attached to the protein of interest with a linker group. Labeling proteins with a linker requires the given protein to have a specific site where the linker can be attached. Usually this consists of a sequence of amino acids that is native to the protein or has been genetically modified to be recognized by a part of the linker. The most commonly used linker is the biotin-streptavidin complex. These proteins form one of the strongest non-covalent binding complexes that exists in biology, with a dissociation constant of  $10^{-13}$ - $10^{-15}$  M and a very high interaction specificity [43]. There are specific amino acid sequences to which biotin can be attached (lysine residues) [44], and several fluorescent probes are commercially available with streptavidin linkers.

The main disadvantage of labeling proteins with either a co-expressed fluorescent protein or a linked fluorophore are steric effects (see, for example, [45]). It is not always known to what extent the attached protein will affect the structure of the native protein or its dynamics. If the labeled protein retains its normal activity levels in the cell (which can be checked by various control experiments to assess the functional role of the protein) then it is

assumed that the label has minimal effect on the natural function. An open question is whether the label perturbs the transport and activity of the protein because the GFP or QD label is usually of comparable size with protein of interest [46]. As such, one can wonder if the observed dynamics are really the native ones or are perturbed due to the size of the fluorescent label on the protein. It is commonly assumed that the dynamics are not affected, for membrane proteins, because the viscous lipid bilayer is thought to be the primary determinant for diffusion rate while the fluorescent label is usually located on parts of the protein outside of the membrane exposed to the less viscous aqueous medium [47, 48].

### 1.5 Current Image Analysis Methods

Fluorescence imaging allows for direct observation of proteins in their native environment, from qualitative observations of protein localization in the cell to precise tracking of single molecules [49]. By attaching a fluorescent probe to a protein of interest and imaging it via fluorescence microscopy, one can localize in space and follow in time the behavior of the labeled macromolecule. Subsequent data acquisition can take the form of intensity trace collection at a single point in the sample [50], or two- or three-dimensional imaging of the sample to generate an (x,y,t) or (x,y,z,t) image time series [51, 52].

There are several methods that are currently used to measure flow magnitudes and/or directions within various systems that have been developed in different fields of study, ranging from physics to computer vision. They are all based on acquisition of a time series of images and subsequent application

of different algorithms for flow or motion analysis. These methods have many interesting biological applications, however they are not all applicable to the biological situations that we are interested in as explained below.

## 1.5.1 Fluorescence Recovery After Photobleaching

Fluorescence Recovery After Photobleaching, or FRAP, is a live cell fluorescence microscopy based technique used to study the mobility of tagged molecules which was introduced in its early forms in the 1970s [53]. It relies on using a focused laser beam to irreversibly photobleach a population of fluorophores in the target region of a cell via a pulse of high-intensity laser light (see Figure 1.6). The target region will appear black as compared to its surroundings, in which the fluorescent molecules have not been bleached. The intensity of the laser is reduced and the sample is imaged as a function of time after bleaching. Diffusion or directed transport of unbleached proteins into the bleach spot leads to an increase in the average fluorescence intensity. By monitoring the recovery of fluorescence in the bleached region and fitting the associated recovery curves to a known analytical form, it is possible to extract diffusion coefficients and immobile protein fraction from FRAP data [54]. The diffusion coefficient is estimated from the rate of recovery of intensity, and the immobile fraction is estimated from a comparison of the prebleach intensity level to the final level of the intensity after recovery (if some of the bleached molecules were immobile, their intensity loss will never be recovered).

However, it has been shown that in non-ideal situations, such as confined diffusion of the labeled proteins, FRAP can severely overestimate the immo-

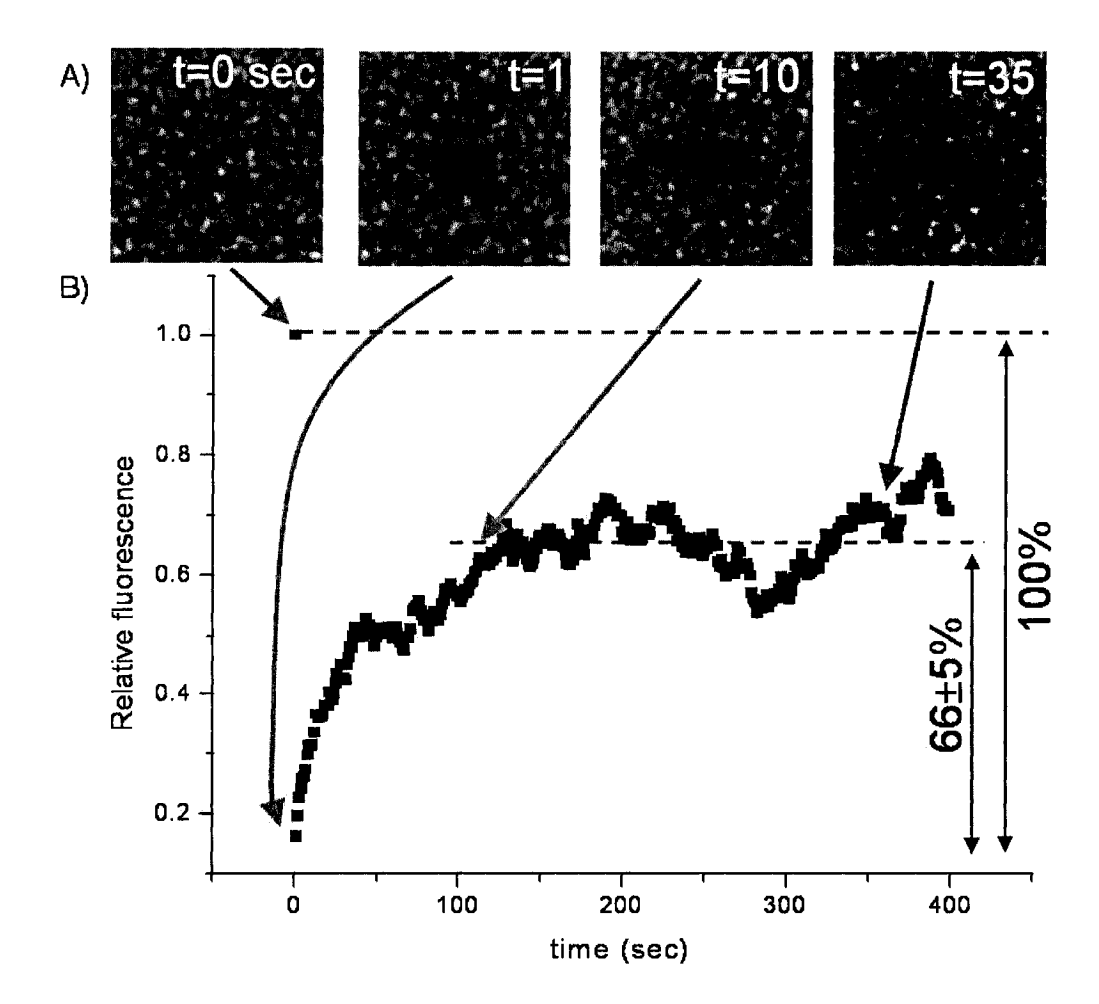


Figure 1.6: Simulation of a FRAP experiment with two populations: the first population has a density of 20 particles/μm² and a diffusion coefficient of 0.02 μm²/s, the second population has a density of 10 particles/μm² and is immobile. A) Image time series with the bleached region in the middle and subsequent recovery of fluorescence. B) Intensity of the bleached region as a function of time, relative to the initial intensity (before bleach). As expected only the mobile fraction contributes to the intensity recovery (here 2/3 of the population was mobile).

bile fraction and underestimate the diffusion coefficient [55]. FRAP is also insensitive to flow direction: although directional transport into the bleached region will affect the rate of fluorescence recovery, it is not possible to know from which direction these new fluorescent particles entered the bleach re-

gion since FRAP only looks at the overall intensity recovery. It is thus not possible to determine the flow direction using FRAP measurements.

### 1.5.2 Single Particle Tracking

Single Particle Tracking (SPT) experiments are well-suited to the noninvasive study of membrane protein transport [56]. In SPT experiments, the position of a single labeled protein is followed by optical imaging as it moves within the membrane. The position is determined by centroid fitting of the image fluorescence intensity peak for the particle and this can be accomplished with a precision on the order of 10's of nanometers. If the motion of the probe is unhindered, the spatial trajectory of the molecule will be described accurately using a two-dimensional model for Brownian motion [57]. The two dimensional random diffusion model predicts that the mean squared displacement (MSD) increases linearly with time:

$$\langle r^2 \rangle = 4 \times D \times t \tag{1.1}$$

where r is displacement, D is the diffusion coefficient of the molecule and t is the time [56, 58] (see Figure 1.7). If the membrane macromolecule encounters a structure that in some way inhibits its free diffusion (see Figure 1.3), then the trajectory will deviate from a random walk. Confined diffusion is usually reflected in the MSD versus time plot as a plateau [59]. At small times, the diffusion looks Brownian because the particle hasn't encountered the boundary of its confinement region and the MSD curve is linear. At longer times however, the particle will not exit this confinement region, which puts an

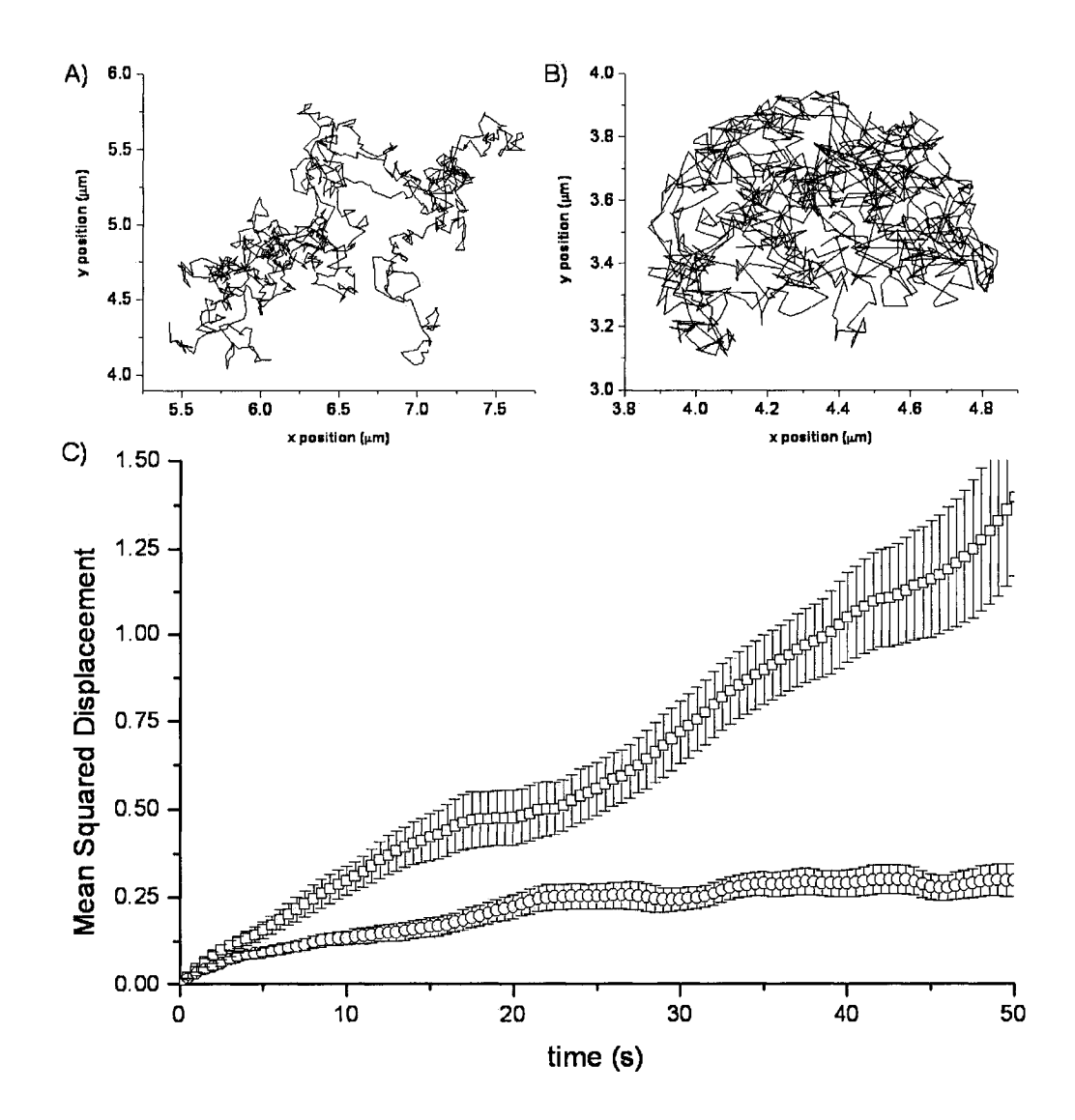


Figure 1.7: Simulation of two SPT experiment A) one particle freely diffusing at 0.01  $\mu m^2/s$  and B) one particle undergoing diffusion at 0.01  $\mu m^2/s$  but in a confined circular region of radius 0.5  $\mu m$ . C) corresponding Mean Squared Displacement versus time plots for the two trajectories in A (open squares) and B (open circles). Notice the plateau of the second MSD indicative of confinement.

upper bound on the possible mean squared displacement (and hence leads to a plateau).

Single particle tracking analysis will, in principle, provide much information about the range of transport [56]. This technique has true single molecule sensitivity, and can reveal very precise information of the dynamics at specific locations within the cell, e.g. confined lateral diffusion of membrane receptors studied by ultra-high temporal resolution single particle tracking (40,000 images per second) using 40 nm colloidal gold labels [47]. However, it can be difficult to track single proteins via fluorescence imaging due to the low signal/noise in live cells and due to the high density of expression of GFP proteins typical for transfected cells which prevents resolution of individual labeled particles. An exception to this will be presented below in section 1.5.4.

## 1.5.3 Optical Flow

In computer vision, one of the challenges is for the machine to analyze a sequence of images and determine if something is moving in its field of view. The definition of optical flow is "the distribution of apparent velocities of movement of brightness patterns in an image" [60]. This technique has had significant impact in environmental sciences such as oceanography, meteorology and climatology where it has been used to track pollutant or ice flows [61, 62]. In medicine, tomography sequences have been used to monitor blood flow in which vortices can indicate pathologies [63].

In all cases, the optical flow technique relies on pattern similitude scoring using a penalty function [64]. In essence, the optical flow method recognizes an intensity pattern in a specific region of an image, and looks for a repetition of that pattern in the following image, in the neighborhood of the region

where the original pattern was found. The optical flow algorithm uses an "optical flow constraint equation" which is equivalent to a conservation of mass equation for intensity:

$$\frac{dE}{dt} = \nabla E \cdot v + \frac{\partial E}{\partial t} \approx 0 \tag{1.2}$$

where E is the brightness as a function of time and space, and v is the velocity of the imaged flow field. This equation basically states that the intensity of a spot is roughly conserved over small time steps (small displacements): it simply insists on identity of intensities between corresponding image elements across time. In practice, to allow for imperfect data, strict enforcement of the continuity constraint is replaced with minimization of a cost function  $c_f$ :

$$c_f = \left(\nabla E \cdot v + \frac{\partial E}{\partial t}\right)^2 \tag{1.3}$$

with respect to v over an image domain of interest. Since the image is two dimensional we need an extra equation to find the two velocity components  $v_x$  and  $v_y$ . This additional constraint is to encourage smoothness of the recovered flow, and can be captured by minimizing the spatial variation of the flow via [65]:

$$c_s = \left(\frac{\partial v_x}{\partial x}\right)^2 + \left(\frac{\partial v_x}{\partial y}\right)^2 + \left(\frac{\partial v_y}{\partial x}\right)^2 + \left(\frac{\partial v_y}{\partial y}\right)^2 \tag{1.4}$$

For every pixel, a velocity vector is found which contains the information on how quickly an intensity pattern around that pixel is moving and its direction. However, this technique has two major flaws when applied to analyzing fluorescence image sequences. First, there is usually a lack of

definite features in fluorescence images of cells, which is an important factor for the optical flow method to work properly. The technique requires much higher local contrast in the patterns than is typical in fluorescence microscopy images of live cells. Second, the presence of a diffusive and an immobile component, and the absence of a clearly resolvable flow from one image to the next in typical fluorescence image series make the mapping of intensities from one frame to the next difficult using this method.

## 1.5.4 Fluorescent Speckle Microscopy

One of the most successful methods for mapping the velocities of labeled proteins in living cells is Fluorescent Speckle Microscopy (FSM). This method relies on microscopic tracking of single fluorescent speckles caused by the random insertion of fluorescent actin (or tubulin) monomers in an otherwise non-fluorescent actin (or tubulin) rod [66, 67]. The actin stress fibers can slip from their attachments and undergo retrograde flow away from the leading edge [68] because of the action of the myosin motors that pull on the cytoskeleton in an attempt to move the cell body forward. The density of labeled actin monomers is so low in FSM experiments that there are only a few labeled monomers in a single actin rod. Thus speckles appear along the actin filaments, and these speckles can be tracked to reveal the retrograde flow of the rod using computationally intensive tracking algorithms [67].

This technique generates a massive amount of information because of the large number of speckles tracked. FSM has been applied in its early stages for mapping simple retrograde flow of actin [66]. Algorithmic advances in speckle image processing allowed mapping of antiparallel flows of microtubule speck-

les in the mitotic spindle from *Xenopus leavis* egg extracts [67]. FSM was also used to reveal the existence of two coexisting actin networks at the leading edge of the cell with different kinetic, kinematic and molecular signatures [69]. More recently, a sub-micrometer resolution version of the technique has been used to measure actin turnover in lamellipodia and lamellae of migrating cells, demonstrating that the dominant feature in their turnover was a spatially random pattern of periodic polymerization and depolymerization moving with the retrograde flow [70].

FSM has proven to be a useful tool in mapping actin and microtubule dynamics, however it is limited to these two types of proteins because of their structure (rods composed of smaller subunits that can generate speckles). Moreover, it requires fluorescent actin or tubulin speckles to be generated in vivo by specialized labeling techniques. The FSM method can be perturbed by immobile and diffusive components which makes it applicable only in the cases where the flow is clearly distinguishable in the image series, i.e. when the vast majority of the protein population is flowing. Moreover, even though the technique claims to have single molecule resolution since it follows individual speckles, in practice one needs to average the calculated velocity vectors over a certain spatial and temporal window in order to filter out the noise. In essence, the FSM technique is well suited for actin or microtubule studies, but does not extend beyond to map flows of other types of proteins.

## 1.6 Spatio Temporal Image Correlation Spectroscopy

The object of this thesis is the development, implementation and application of STICS. This new technique is intended to map velocity fields in a wide range of settings, and specifically in cases where other methods would fail, as outlined above. This new method is an extension of a class of fluctuation based techniques called "correlation spectroscopy" that include fluorescence correlation spectroscopy (FCS) [71, 72, 73] and image correlation spectroscopy (ICS) [74, 51] which are discussed in more detail in the next chapter. It also builds on some of the early pixel correlation ideas developed in the computer vision field [75].

To understand the molecular mechanisms that regulate cell migration, new techniques are necessary that can be applied in situ in living cells. The STICS method was developed for this purpose. In this thesis, I will first present the theoretical basis of STICS and new algorithms that were developed for filtering out the immobile component. Using computer simulations, I will then characterize the detection limits of STICS in terms of several important imaging parameters, such as signal to noise, number of frames in the image time series and density of the protein population. I will also investigate the limits of the immobile population filtering algorithms. Following this characterization will be a description of the various corrections that have to be applied to in situ images. I will also discuss the control measurements and how STICS and its cross correlation counterpart, Spatio Temporal Image Cross-Correlation Spectroscopy (STICCS), can be applied to measure dynamics in living cells. Finally, I will present the application of

the technique to two very different biological problems of interest: the regulation of the cytoskeleton-ECM linkage, and the problem of detecting and measuring fluid flow inside migrating cells. 2 THEORY 25

# 2 Theory

## 2.1 Introduction

In its widest sense, science can be categorized into layers where the principles discovered in one layer become the foundation for the next layer above. From the physical understanding of the quantum world of atoms, to the chemistry of molecules, to the microbiological studies of cells, to the physiology of the human body, every level gains from the broadening of its foundations. However, this view emphasizes the strong interconnectedness within a field and neglects the relatively few but important links between fields. Physics has broadened its base for decades now by expanding into non-traditional fields. Biophysics has emerged as an expanding domain of research that spans many orders in space and time ranging from the submolecular (protein conformation and folding) to cellular dynamics and interactions between cells and within tissue. A common theme, be it theoretical or experimental biophysics, is to achieve a quantitative understanding of the complex mechanisms that govern biological systems. Many techniques have been invented or adapted to meet the need for quantitative information, and many new questions require the development of novel quantitative methods for assessing biophysical processes.

The theory presented in this chapter provides the underpinnings for the subject of this thesis: spatio-temporal image correlation spectroscopy (STICS). After an introduction of basic fluorescence and microscopy imaging systems, I will provide an overview of image correlation spectroscopy (ICS). ICS is a fluctuation based technique that is classified as part of a broader category

of concentration correlation spectroscopy methods, such as fluorescence correlation spectroscopy (FCS) [72, 76] or scanning FCS (S-FCS) [77]. I will then introduce the spatio temporal extension of ICS (STICS), which relies on a complete correlation of the spatial and temporal fluorescence fluctuations contained in fluorescence microscopy image time series and can be used for velocity mapping of proteins in cells. I will also discuss a new filtering algorithm for image series that uses filtering in Fourier space to remove the contribution of an immobile or slowly moving protein population from the correlation analysis.

# 2.2 Fluorescence and Jabloński Energy Diagrams

To understand the principles of fluorescence imaging, it is important to first understand the fluorescence phenomenon. Much like the excited states of an atom, fluorescence can be explained via a Jabloński energy diagram for the molecule where different energy states for the electrons in the system are arranged according to their energy like rungs of a ladder [78].

The fluorescence excitation-emission process is illustrated in Figure 2.1. Initially the molecule is in the singlet ground state  $S_0$ , and upon excitation an electron can be promoted to an excited singlet state  $S_1$ . The excitation source we are concerned with is light, and the energy needed to jump to an excited state is absorbed quantally either in a single photon [79] (one photon absorption) or with two or more photons (N-photon absorption) whose energy quanta sum to equal the difference in energy between the ground and excited states [80]. Two-photon absorption is a non linear effect produced by the quasi-simultaneous absorption of two excitation photons of exactly

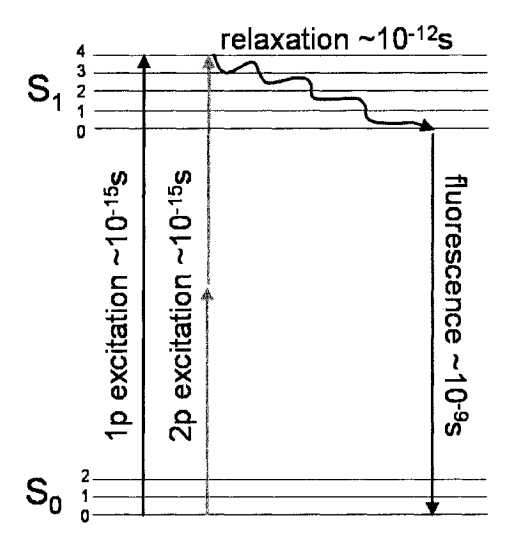


Figure 2.1: Jabloński Diagram.  $S_0$  is the electronic ground state,  $S_1$  is the excited singlet state, bars 0,1,2,3,4 represent vibrational energy levels in each electronic energy level.

half the energy of an allowed transition [80]. One needs to tightly focus ultra short pulsed lasers in order for the density of photons to be high enough to achieve non-linear excitation. After the rapid ( $\sim$  fs) absorption event, the fluorophore is usually in a high vibrational level of the first excited singlet state, which quickly ( $\sim$  ps) decays to the lowest excited singlet state vibrational energy level through non-radiative decay in a process called internal conversion.

The fluorescence photon is emitted when the molecule drops from the lowest vibrational excited singlet state energy level back to the ground state. The lifetime of the excited state in this level is orders of magnitude longer ( $\sim$  ns) than the internal conversion step and if the electron decays back to the ground state from this level, a photon will be emitted by fluorescence emission. Due to the internal conversion, energy is lost so the fluorescence

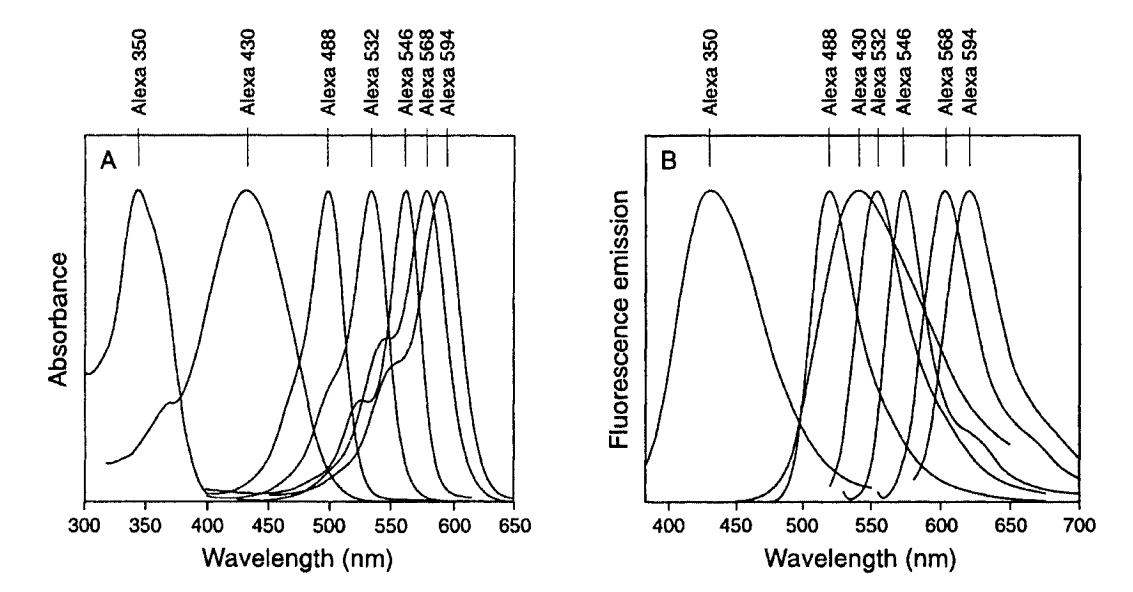


Figure 2.2: Alexa family dye spectra adapted from [81]. Notice for example that the Alexa488 dye, which has a characteristic spectrum close to that of GFP, absorbs light around 488nm and emits around 520nm.

photon is red-shifted when compared to the (total) excitation energy (see Figure 2.2). This shift in the emission wavelength, called the Stokes shift, is essential for fluorescence microscopy. The greater the Stokes shift, the easier it is to separate the excitation light from the emitted light. This separation is the basis of the sensitivity of fluorescence microscopy. Since the light intensity required to excite the molecules is much greater than the emitted light intensity, filters are needed to efficiently block out the excitation light and detect the weaker fluorescence emission.

# 2.3 Fluorescence Microscopy

#### 2.3.1 General Microscope Instrumentation

The optical microscope is the basic instrument used to image fluorescent molecules within cells (see Figure 2.3). Multiple laser lines are combined and

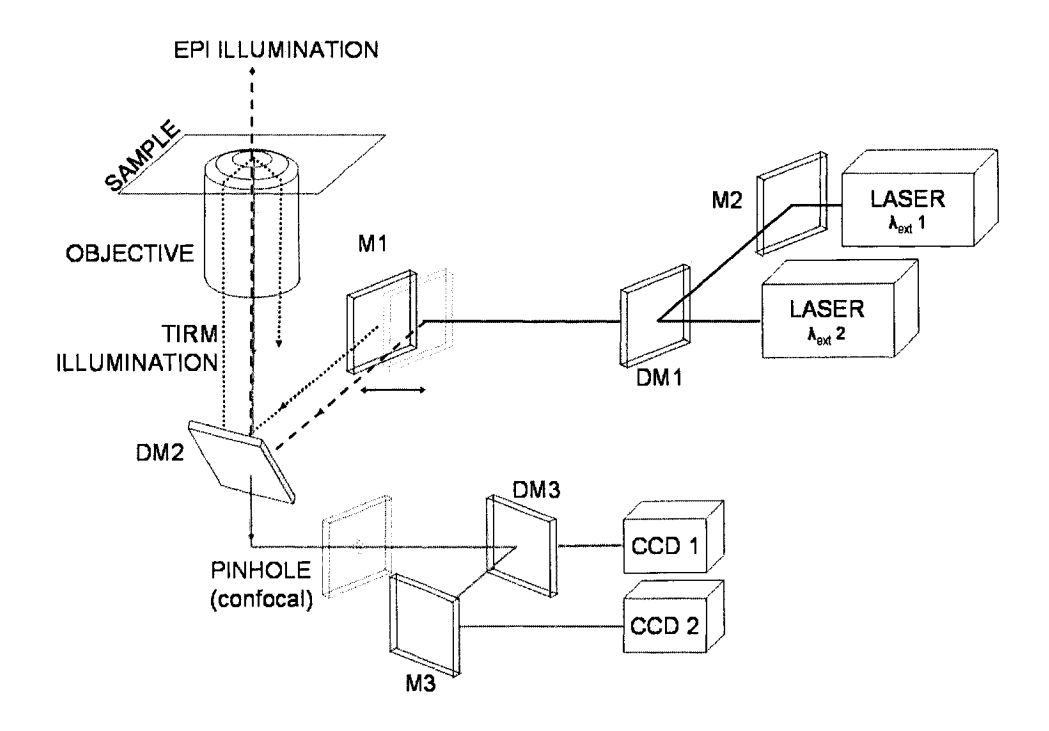


Figure 2.3: Schematic drawing of a fluorescence microscope used for imaging of fluorescently labeled molecules. Multiple laser lines can be combined through a first dichroic mirror (DM1). Aligning the illumination to the appropriate angle for wide field, laser scanning or total internal reflection microscopy is accomplished by translating a single mirror (M1). A second dichroic mirror (DM2) introduces the laser into the objective lens while allowing the emitted fluorescence to pass through. In the confocal scheme, a pinhole is needed to filter out of focus light (see section 2.3.3). The fluorescence is split in two (or more) channels using a dichroic mirror (DM3) and is detected by CCD cameras (or other light detectors such as photo multiplier tubes (PMTs)) through appropriate emission filters.

focused on the sample through the microscope objective lens. The fluorescence photons are emitted into a solid angle of  $4\pi$  (all directions in space) and a fraction are collected back through the same objective lens, and split by wavelength through an emission dichroic filter and focused on different detectors for multiple channel (wavelength) imaging. The sample is placed

on a stage above the objective lens (for an inverted microscope scheme, as illustrated in Figure 2.3), and coupled to the objective through an index matching medium (immersion oil, water, air). The focus is adjusted manually by controlling the height of the objective relative to the sample. The excitation laser beam can be expanded to just overfill the back aperture of the objective lens for point illumination (diffraction limited focus in the absence of abberations) in epi-fluorescence or laser scanning microscopy (confocal or multiphoton). Or the laser may underfill the back aperture of the objective lens and enter at the edge of the aperture (see Figure 2.3) for total internal reflection microscopy; this generates an evanescent field at the interface with the objective, which excites the fluorophores.

#### 2.3.2 Wide Field Fluorescence

Wide field microscopy is the simplest implementation of the light microscope for biological fluorescence imaging [82]. The excitation light is usually provided by a mercury lamp, which can deliver a broad range of frequencies at high intensity, from which the desired wavelength is selected by using filters. The light is focused through the microscope objective lens and creates a focal plane where the excitation intensity is higher than the surroundings. Fluorescence emission is collected through the same objective and directed to an eye piece for viewing, or a camera for digital capture (see Figure 2.4).

The optical spatial resolution of this system is dictated by the wavelength of light  $(\lambda)$  via diffraction effects and by the numerical aperture (NA, see Eq.

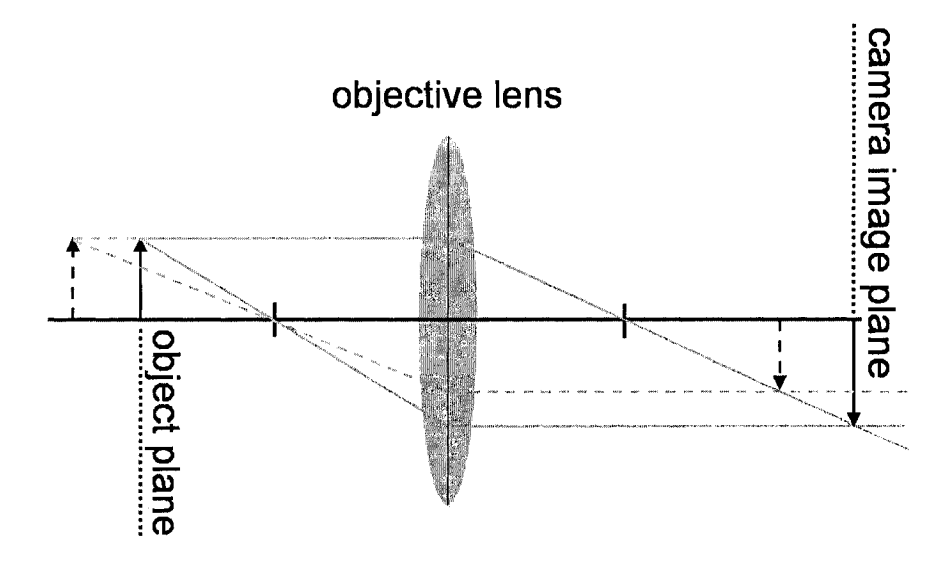


Figure 2.4: Illustration of the object plane in wide field microscopy. The solid arrow is imaged directly on the camera detector, while the dashed arrow is imaged in front of the camera image plane therefore it appears out of focus in the collected image.

2.3 for definition) of the objective lens, following [83]:

lateral (x,y) resolution = 
$$\frac{1.22\lambda}{2 \times NA}$$
 (2.1)

Equation 2.1 indicates that such a system is theoretically able to resolve between two objects separated by as little as 200 nm ( $\lambda \approx 535$  nm, NA $\approx 1.45$ ). Note that Equation 2.1 is appropriate for wide field microscopy and is based upon a number of factors that account for the behavior of objectives and condenser lenses, and should not be considered an absolute value due to one general physical law. In some instances, such as confocal and fluorescence microscopy, the resolution may actually exceed the limits set by this equation. Other factors, such as low specimen contrast, aberrations, improper illumination and beam alignment may serve to lower resolution and, more often than not, the diffraction limited value of the resolution (about 200nm

as mentioned above) is not realized in practice.

Fluorescence microscopy is very useful for biological applications because it can be applied to living samples, and fluorescence detection is very sensitive. However, one factor severely limits the applications of wide field microscopy in biology: the "out-of-focus" light coming from every plane in the sample strongly contributes to background noise and leads to blurring of the image. If the fluorescence staining is confined to a small region (for example a cellular organelle, like the Golgi apparatus) and the background noise is reduced to a minimum then wide field microscopy can produce quality images. In most experimental applications, however, a confinement of the light from a single focal plane (rather than a confinement of the labeling) is desired. A solution to this problem is presented in the next section.

#### 2.3.3 Laser scanning microscopy

Microscopy systems used to image low quantum efficiency fluorescent probes in a high density environment need to satisfy a few requirements: i) they require good spatial and temporal resolution, ii) they need to collect the signal from a single plane and efficiently reject the background from outside the focal plane (optical sectioning) and iii) they should not perturb the living system (i.e. be non-invasive). A laser scanning microscope can satisfy all these requirements to varying degrees in two different forms: the confocal microscope and the two-photon microscope.

Early laser scanning microscopes were based on specimen scanning [84, 85]. The main advantage of this method is that the beam path is fixed, en-

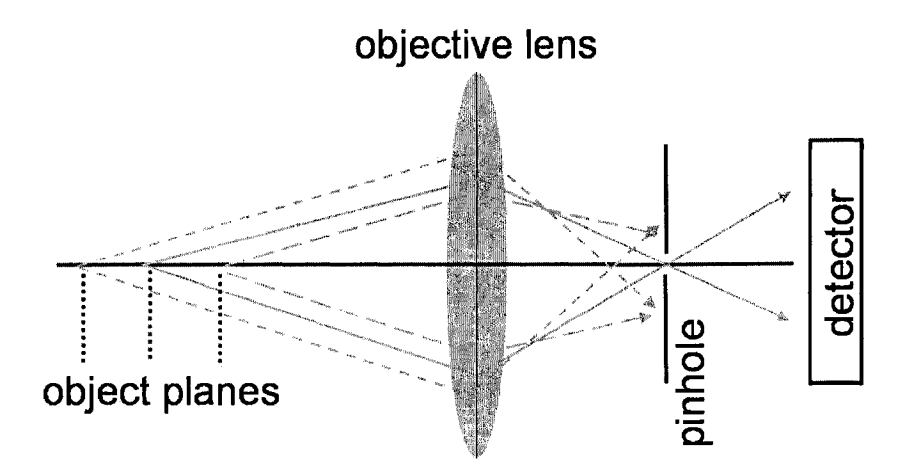


Figure 2.5: Principal light pathway in confocal microscopy. The emitted light is filtered by the pinhole in the image plane: out-of-focus light is blocked by the pinhole because it is not focused at the image plane.

suring proper illumination of the sample at all times. However, the drawback is that the scanning rates are slow (10-150 lines per second) so that the range of dynamic processes that can be imaged is limited. More recent commercial systems use scanning of the laser beam rather than the specimen which allows for much faster scanning (500 lines per second). Since the laser beam is scanned before entering the objective lens, the scan mirrors have to be placed in a conjugate plane to the back aperture plane of the objective lens [86]. In a typical laser scanning microscope, the fluorescence signal is collected in the backscattered direction, allowing the fluorescence to be "de-scanned" by the scanning mirrors and imaged onto a stationary detector.

The confocal laser scanning microscope (CLSM) (see Figures 2.3 and 2.5) has several advantages over conventional wide-field microscopy, namely the ability to control depth of field, elimination or reduction of background fluorescence originating outside of the focal plane, and the capability to collect

serial optical sections from thick specimens. The term "confocal" refers to the spatial filtering of the backscattered fluorescence signal by use of a pinhole placed in the confocal image plane [86], which filters light originating from planes above and below the focal plane of interest (see Figure 2.5). This allows optical sectioning of thin  $(0.5-1.5\mu m)$  slices through a biological sample, since fluorescence is effectively collected only from a small illumination volume (see Figure 2.7A) defined by the spatial extent of the confocal point spread function (PSF). Due to diffraction effects, the laser light passing through the excitation pinhole is not focused to a point, but rather a three dimensional intensity distribution: the excitation PSF. Likewise, the collected fluorescence light is also imaged as a three dimensional distribution on the detection pinhole: the detection PSF. Both PSFs have the same shape but differ in size because of the different objective lens responses to the excitation and emission wavelengths [83]. The PSF characterizes the resolution of the imaging system, since a point emitter (sub diffraction limit size emitter) maps as a PSF in the image space due to diffraction. In the focal plane, the diffraction pattern is proportional to the first order Bessel function of the first kind, which can be well approximated by a Gaussian [83]. Although the instrument is limited by the number of available wavelengths from conventional laser sources, by the transmission properties of the built-in optics and by the range of laser intensities that can be safely delivered to live cells, it remains the tool of choice for producing high quality images of living samples.

The two-photon microscope [87] also has optical sectioning capability but relies on a completely different principle to achieve this [80]. Long wavelength (IR), high intensity, femtosecond laser pulses are focused within the sample

and the excitation of the fluorophore is achieved via two-photon absorption as discussed in section 2.2. Such an event can only take place when the intensity is high enough so that there is a significant probability of simultaneous absorption of two photons by the fluorophore. This occurs only in a small region in the vicinity of the focus. Although the effective PSF for two-photon absorption is slightly larger than the confocal PSF it has the definite advantage that outside of this volume, none of the fluorophores are excited. This entails less photobleaching of the out-of-focus dyes and less photodamage to the sample. Two-photon microscopy thus presents inherent optical sectioning without the use of a pinhole and can be better suited to live sample imaging, but requires expensive pulsed lasers and can have lower signal to noise as compared to regular confocal microscopy.

## 2.3.4 Total Internal Reflection Microscopy

Total Internal Reflection Microscopy (TIRM) is an evanescent wave based technique used to locally excite fluorescence from a sample located within a few hundred nanometers of the boundary interface surface [88, 89]. It uses the optical phenomenon known as total internal reflection: when light strikes an interface going from a high refractive index medium to a low refractive index medium at an angle greater than the critical angle  $\theta_c$ , it undergoes total internal reflection (see figure 2.6). The critical angle is given by [88]:

$$\theta_c = \sin^{-1}(n_2/n_1) \tag{2.2}$$

where  $n_1(n_2)$  is the refractive index of the first (second) medium, and  $n_1 > n_2$ . In the second, lower refractive index medium there is still a propagation of the electric field in the boundary layer (parallel to the interface) called the "evanescent wave", but this boundary wave decays exponentially in the z direction. If a laser beam is totally internally reflected from inside the objective and off the glass coverslip interface, it is possible for the evanescent wave to excite fluorescent molecules within  $\sim 100$  nm of this surface. The excited fluorescence is collected back through the same objective lens, through standard dichroics and emission filters.

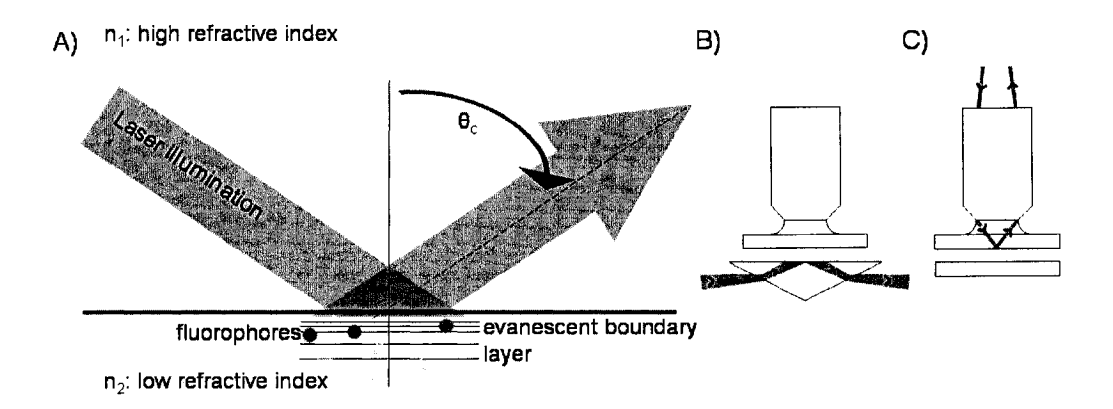


Figure 2.6: Total Internal Reflection Microscopy. A) The laser beam (shown as a thick arrow) strikes the interface between the high and low refractive index media at an angle greater than or equal to the critical angle  $\theta_c$ . An exponentially decaying evanescent wave, which can be used to excite fluorescent molecules in the low index medium that are close ( $\sim 100$  nm) to the boundary, is created. B) experimental setup for prism-based TIRM. C) experimental setup for through-objective TIRM.

Total Internal Reflection Microscopy has the potential to generate images with single molecule sensitivity [90, 91, 92, 93]. There is much lower background signal than in confocal or two-photon systems because the exponentially decaying evanescent wave does not excite most of the fluorophores in the bulk solution [89]. In vivo imaging using TIRM is also very useful

for studies of the basolateral (bottom) membrane of the cell, where macromolecular adhesion complexes form within two dimensional tissue cultured
cells. Since this membrane is only about 5 nm thick and located near the
coverslip boundary, it is completely immersed in the evanescent field, as are
all the transmembrane proteins and their molecular partners. This technique
is thus very useful for imaging of adhesion related proteins, since the fluorescently labeled adhesion molecules are present both in adhesions at the cell
membrane, but also as unbound entities in the cytosol within the cell. This
allows for very high signal to noise imaging of the adhesions, with minimal
contribution from cytosolic background.

There are several experimental geometries used to achieve TIRM near a dielectric interface in wide-field microscopy [89, 94]. Prism-based and through-objective TIRM (see Figure 2.6) have been used extensively and they each have their own advantages [89]. Experiments in which the total number of photons is of importance should employ a near wall geometry (such as through-objective TIRM) and experiments which require a rapid measurement with good signal to noise, as single molecule measurements do, should use a far wall geometry (such as prism-based TIRM) [95]. In the case of slow adhesion related protein motion, the signal-to-noise and photon collection are of importance, so we used the through objective configuration.

The collection efficiency of the objective in through-objective TIRM is characterized by the numerical aperture (NA):

$$NA = n \times sin(\theta) \tag{2.3}$$

where n is the index of refraction of the medium and  $\theta$  is the half angle of light collection. The NA, usually 1.2-1.45 for high numerical aperture objective lenses, is a measure of how wide a cone of light the objective can gather: the greater the NA, the wider the cone of light and the greater the resolution of the lens. Hence a larger NA objective is desirable to permit a greater angle of incidence for the laser in through-objective TIRM. For example, the refractive index of the aqueous medium is usually about 1.33 to 1.38, while the refractive index of glass is 1.52. Thus for an objective built from glass, in order to have incoming illumination at an angle greater than the critical angle, we need to have  $n_1 sin(\theta) > n_2$  (see Eq. 2.2), thus one needs the NA > 1.35 in order to achieve through objective evanescent illumination. There are 1.65 NA objectives available on the market but they require the use of toxic immersion oils and costly high refractive index glass such as sapphire. A 1.45 NA objective can be used with regular glass and immersion oil so it is an optimal lens for TIRM.

There is no scanning involved in TIRM. The whole field of view is illuminated with the evanescent wave and this area is imaged using a cooled charged coupled device (CCD) camera. Hence there is no illumination volume per se as in confocal or two-photon microscopy. However, it is not possible to surpass the diffraction limit as there is still collection of the fluorescence emission through the collection optics (the objective lens), which means that a point emitter will still transform to a PSF-sized spot in the image. The advantage of TIRM, in addition to the narrow depth of field at the interface, is that modern cooled CCD cameras permit very short acquisition times, on

the order of 50 ms per image ( $\sim$ 10 ms or faster for some cameras) compared to the  $\sim$ 1 Hz imaging rate for standard LSMs. This allows the study of faster dynamic processes in the basolateral membrane of the cells and at the inside interface with the membrane.

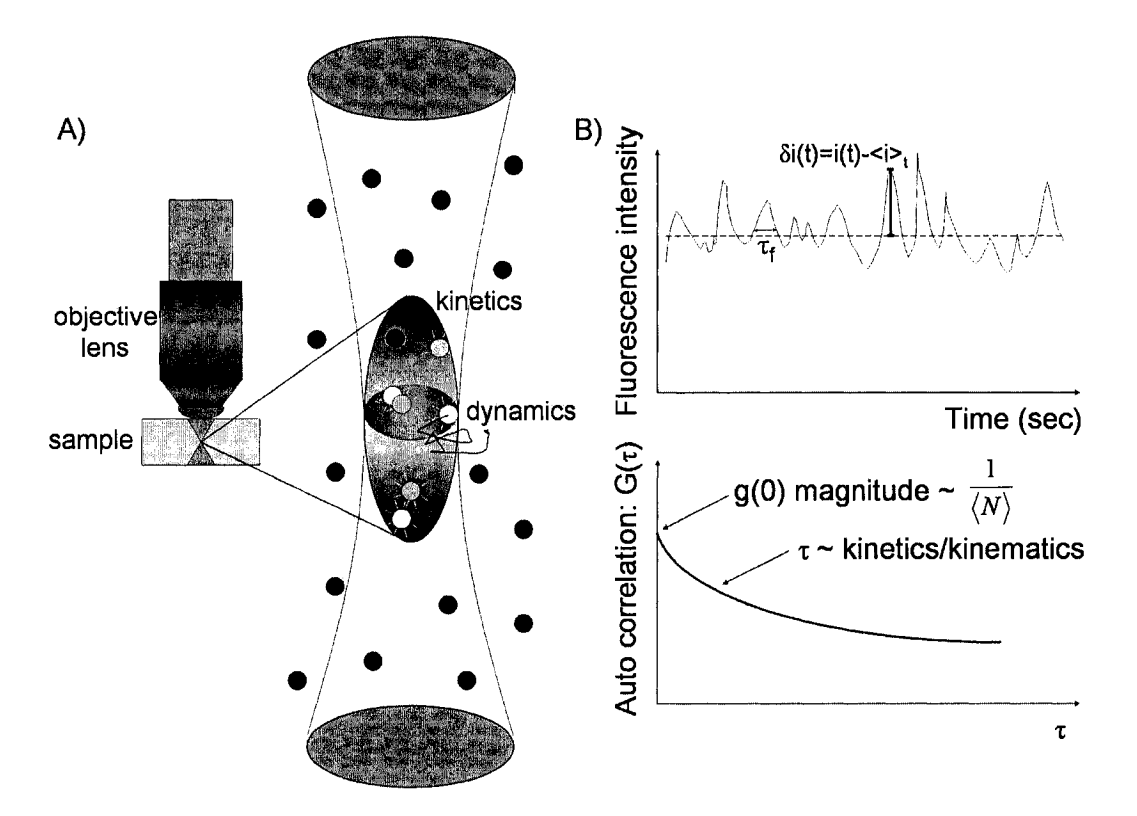


Figure 2.7: Schematic diagram of the fluorescence correlation spectroscopy method. A) In either case, the fluorescence intensity is collected only from a small region (focal volume). Fluorescence fluctuations arise from either the molecules entering or exiting of the volume (kinematics) and/or chemical reactions affecting the fluorescence intensity (kinetics). B) The intensity can be collected in time from a single point, and the autocorrelation function of the intensity fluctuation time series reflects the dynamics of the system.

## 2.4 Fluorescence Correlation Spectroscopy

The technique of Fluorescence Correlation Spectroscopy (FCS) was developed in the early 1970s, at Cornell University [71]. Although originally implemented by relatively few groups in the biophysical community, FCS really blossomed in the 1990's due to advances in electronics, computers, detectors, lasers and especially due to the implementation of confocal optics for FCS [96]. In essence, FCS looks at the temporal persistence of the fluorescence intensity fluctuations collected from a small volume (<1 fL) defined by the focus of a laser beam as fluorescent molecules move into and out of the focal volume (see Figure 2.7A). Much information is contained in the magnitude and characteristic time scale of the fluctuations including molecular concentration and kinetics/kinematics. Qualitatively, this stems from the fact that the higher the concentration, the more particles you will find in the small observation volume and the smaller the relative intensity fluctuations will be, since fluorescence emission is an extensive property of the system. The transport dynamics, and possibly chemical reaction rates and/or photophysical processes such as photobleaching (see section 4.2.1), are responsible for the fluctuations in intensity as molecules enter and leave the laser focus, changing the occupation number. The fluorescence intensity fluctuations are recorded in a time series which is used to calculate a temporal autocorrelation function (ACF) that can be fit with appropriate decay models to solve for the transport properties (diffusion coefficient, flow speeds) if the dimensions of the focal volume are known (see Figure 2.7B). The fit models are obtained by solving the fluctuation ACF within the context of the appropriate transport equation (e.g. diffusion law or flow with constant velocity) and laser

excitation profiles.

The time scales involved in FCS are from the microsecond to the millisecond. The inherent rates at which data can be collected by modern photo multiplier tubes (PMTs) or avalanche photo diodes (APDs) make it possible to probe reactions and dynamics happening on short time scales within cells. However, the continuous illumination of the sample can entail photodamage to the fluorescent dye or the protein under study, and may prevent extended exposure times to study long scale dynamic processes. As well, the measurement is localized to only one point in space. Moreover, FCS measurements of dynamics on slow time scales can suffer from low signal to noise ratios, since for a fluctuation measurement, this ratio depends on the square root of the number of independent fluctuations sampled. Entities with slow transport dynamics (e.g. membrane protein diffusion) will therefore not create enough independent fluctuations over the time course of a typical FCS experiment in a living cell. Several extensions of FCS have been developed to address this problem [51, 77], and we will focus our attention on image correlation spectroscopy.

# 2.5 Image Correlation Spectroscopy

Image correlation spectroscopy (ICS) was introduced a decade ago in Nils Petersen's laboratory at the University of Western Ontario (UWO). It was initially developed as the imaging analog of FCS for measuring labeled protein surface densities and aggregation state [51]. Later, ICS was further extended to the temporal domain by calculation of a temporal ACF from an

LSM image time series [97]. The characteristic imaging rate of the LSM (~1 Hz) makes it possible to probe processes happening on the seconds to minutes time scales, which are characteristic of membrane protein dynamics. A summary of the basic concepts behind ICS and its cross-correlation variant, image cross-correlation spectroscopy (ICCS), will be provided in order to set the stage for the introduction of the theory necessary for the spatio-temporal image correlation spectroscopy (STICS) method.

## 2.5.1 Generalized Spatio-Temporal Correlation Function

ICS is based on the correlation of fluorescence intensity fluctuations measured from an observation area defined by the diffraction limited focal spot of the exciting laser beam in a LSM. The intensity fluctuations in fluorescence are recorded in an image series as the laser beam is repeatedly rastered across the sample. The image series can be thought of as a record of fluorescence intensity in space and time (we consider only collection from a single fixed plane in z): i(x,y,t). It is an easy matter to calculate the mean intensity of the  $n^{th}$  image:

$$\langle i \rangle_n = \frac{1}{NM} \sum_{j=0}^N \sum_{k=0}^M i(j, k, n)$$
 (2.4)

where N and M are the spatial dimension (in pixels) of an image from the time series. Spatial and temporal correlation is then applied to the image time series. We define a generalized spatio-temporal intensity fluctuation correlation function which is a function of spatial lag variables  $\xi$  and  $\eta$  and of a temporal lag variable  $\tau$  for detection channels a and b:

$$r_{ab}(\xi, \eta, \tau) = \frac{\langle \delta i_a(x, y, t) \delta i_b(x + \xi, y + \eta, t + \tau) \rangle}{\langle i_a \rangle_t \langle i_b \rangle_{t+\tau}}$$
(2.5)

where  $\delta i_{a(b)}(x,y,t) = i_{a(b)}(x,y,t) - \langle i_{a(b)}\rangle_t$  is the intensity fluctuation in channel a(b) at pixel position (x,y) and time t, and the angular  $\langle \text{brackets} \rangle$  in the denominator represent spatial ensemble intensity averaging over images at time t and  $t+\tau$  in the time series, and the numerator is also an ensemble average over all pixel fluctuations in pairs of images separated by a lag time of  $\tau$ . White noise sources contribute to the numerator only at zero lags (temporal and spatial), whereas white noise does contribute to the average intensities in the denominator. Correction methods dealing with white noise and background correlation have been reported [97]. This discrete calculation of the correlation function can be fit with the appropriate models (see sections below), and the zero lags amplitude value is not weighed in the fits.

## 2.5.2 Spatial Correlation and Cross-Correlation

ICS has traditionally treated the cases for spatial and temporal correlations separately. The spatial correlation function  $\mathbf{r}_{ab}(\xi,\eta,0)$  is defined by evaluating Eq. 2.5 with zero time lag:

$$r_{ab}(\xi, \eta, 0) = \frac{\langle \delta i_a(x, y, t) \delta i_b(x + \xi, y + \eta, t) \rangle}{\langle i_a \rangle_t \langle i_b \rangle_t}$$
(2.6)

These functions are typically calculated by Fourier methods for each image in the time series using:

$$r_{ab}(\xi, \eta, 0)_n = \frac{FFT^{-1}\{FFT(i_a(x, y, n)) \times FFT(i_b(x, y, n))^*\}}{\langle i_a(x, y, n) \rangle \langle i_b(x, y, n) \rangle}$$
(2.7)

where  $r_{ab}(\xi, \eta, 0)_n$  is the spatial correlation function of the  $n^{th}$  images of the image time series from channels a and b,  $FFT^{(-1)}$  denotes the (inverse) Fast

Fourier Transform and \* denotes complex conjugation. The spatial correlation functions are then fit to standard 2D Gaussian functions by nonlinear least squares methods. This is due to the fact that a  $TEM_{00}$  "Gaussian" beam acts as the correlator in the LSM measurement [51, 97]. The Gaussian fit function for the spatial correlation of the  $n^{th}$  image is given as:

$$r_{ab}(\xi, \eta, 0)_n = g_{ab}(0, 0, 0)_n exp \left\{ -\frac{\xi^2 + \eta^2}{\omega_{0ab}^2} \right\} + g_{\infty abn}$$
 (2.8)

(note in this fitting equation and those that follow, the fit parameters are highlighted in bold type). The fit parameters are the zero-lags amplitude  $g_{ab}(0,0,0)_n$ , the  $e^{-2}$  beam radius  $\omega_{0ab}$  (the horizontal radius of the beam focal spot), and the offset at long correlation lengths  $g_{\infty abn}$ . For an ideal system of non-interacting particles, the zero lag amplitude  $g_{ab}(0,0,0)_n$  is the square relative intensity fluctuation and is equal to the inverse of the mean number of independent fluorescent particles in the correlation area defined by the focus of the laser [51]. When a=b= 1 or 2, Eq. 2.6 defines a spatial autocorrelation function for a single detection channel, and when a=1 and b=2, Eq. 2.6 defines a spatial cross-correlation function between two detection channels.

#### 2.5.3 Temporal Correlation and Cross-Correlation

The temporal correlation function is given by evaluating the generalized correlation function at zero spatial lags:

$$r_{ab}(0,0,\tau) = \frac{\langle \delta i_a(x,y,t)\delta i_b(x,y,t+\tau)\rangle}{\langle i_a\rangle_t\langle i_b\rangle_{t+\tau}}$$
(2.9)

Its decay will essentially depend on the temporal persistence of the average spatial correlation of intensity fluctuations between images in the time series separated by a lag time of  $\tau$  as measured from an ensemble of focal spots (correlation areas) within a sampled image area. The same relationships hold for the a and b subscripts in defining temporal auto and cross-correlation functions as was outlined above for the spatial case.

### 2.5.4 Decay Models for Correlation Functions

The rate and shape of the decay of the correlation functions will reflect any dynamic process that contributes fluctuations on the time scale of the measurement [72]. The actual decay models for fluorescence correlation will depend on both the underlying dynamics of the fluctuating process and the geometry of the laser focal spot (the point spread function) [98]. We consider four separate functional forms that are analytical solutions for the generalized intensity fluctuation correlation function appropriate for specific cases of 2D transport phenomena as measured within a membrane system illuminated by a  $TEM_{00}$  laser beam with Gaussian transverse intensity profile:

2D Diffusion [72]:

$$r_{ab}(0,0,\tau) = g_{ab}(0,0,0) \left(1 + \frac{t}{\tau_d}\right)^{-1} + g_{\infty ab}$$
 (2.10)

2D Flow [99]:

$$r_{ab}(0,0,\tau) = g_{ab}(0,0,0)exp\left\{-\left(\frac{|\boldsymbol{v_f}|\tau}{\langle\omega_{0ab}\rangle}\right)^2\right\} + g_{\infty ab}$$
 (2.11)

2D Diffusion and Flow for a Single Population [99]:

$$r_{ab}(0,0,\tau) = g_{ab}(0,0,0) \left(1 + \frac{t}{\tau_d}\right)^{-1} \times$$

$$exp\left\{ -\left(\frac{|\boldsymbol{v_f}|\tau}{\langle \omega_{0ab}\rangle}\right)^2 \left(1 + \frac{t}{\tau_d}\right)^{-1} \right\} + g_{\infty ab}$$
(2.12)

2D Diffusion and Flow for Two Populations (i=1,2) [1]:

$$r_{ab}(0,0,\tau) = g_{ab}(0,0,0)_1 \left(1 + \frac{t}{\tau_{d1}}\right)^{-1} +$$

$$g_{ab}(0,0,0)_2 exp \left\{ -\left(\frac{|\boldsymbol{v_{f2}}|\tau}{\langle \omega_{0ab}\rangle}\right)^2 \right\} + g_{\infty ab}$$
(2.13)

The highlighted fit parameters are the zero-lags amplitude  $g_{ab}(0,0,0)_n$ , the long correlation time offset  $g_{\infty ab}$ , the characteristic diffusion decay time  $\tau_d$  and the mean speed of the particles  $|v_f|$ :

$$|v_f| = \frac{\omega_{0ab}}{\tau_f} \tag{2.14}$$

where  $\tau_f$  is the characteristic flow time. The effective  $e^{-2}$  beam radius is calculated by averaging the individual  $\omega_{0ab}$  obtained from fitting the spatial correlation functions (Eq. 2.8) for every image in the time series. The best fit characteristic diffusion time combined with the average beam radius allow calculation of the diffusion coefficient:

$$D_{exp} = \frac{\langle \omega_{0ab} \rangle^2}{4\tau_d} \tag{2.15}$$

Note that in Eq. 2.14, the mean speed  $|v_f|$  is directionally blind (a velocity

magnitude). Temporal ICS is not sensitive to the direction in which the particles exit the observation area, because the basic analysis does not include non zero spatial lags in combination with the temporal lags in the calculation of the correlation function (see Eq. 2.9).

# 2.6 Space-Time Image Correlation Spectroscopy

The object of this thesis is to develop, characterize and apply a new extension of ICS and ICCS in order to obtain flow vectors, or essentially to determine the direction in which the particles are exiting the correlation areas if directed flux is present. To achieve this, one must combine the spatial information embedded in the two dimensional spatial correlations with the time dependent transport measured by the temporal correlation. For this we define a discrete approximation to the full space-time correlation function as:

$$r'_{ab}(\xi, \eta, s) = \frac{1}{N - s} \times \sum_{t=1}^{N - s} \frac{\langle \delta i_a(x, y, t) \delta i_b(x + \xi, y + \eta, t + s) \rangle}{\langle i_a \rangle_t \langle i_b \rangle_{t+s}}$$
(2.16)

where N is the total number of images in the time series. The function  $r'_{ab}$  represents the average cross correlation function for channels a and b, for all pairs of images separated by a lag time of  $\Delta t = s\delta t$  (where s is the discrete frame lag between pairs of images and  $\delta t$  is the sampling time per frame). This generalized space-time correlation function can be considered as a time series, where the individual frames are averaged two dimensional spatial (cross-)correlation functions, and the time variable is actually the lag time ( $\Delta t$ ) between all image pairs for which the correlation was computed.

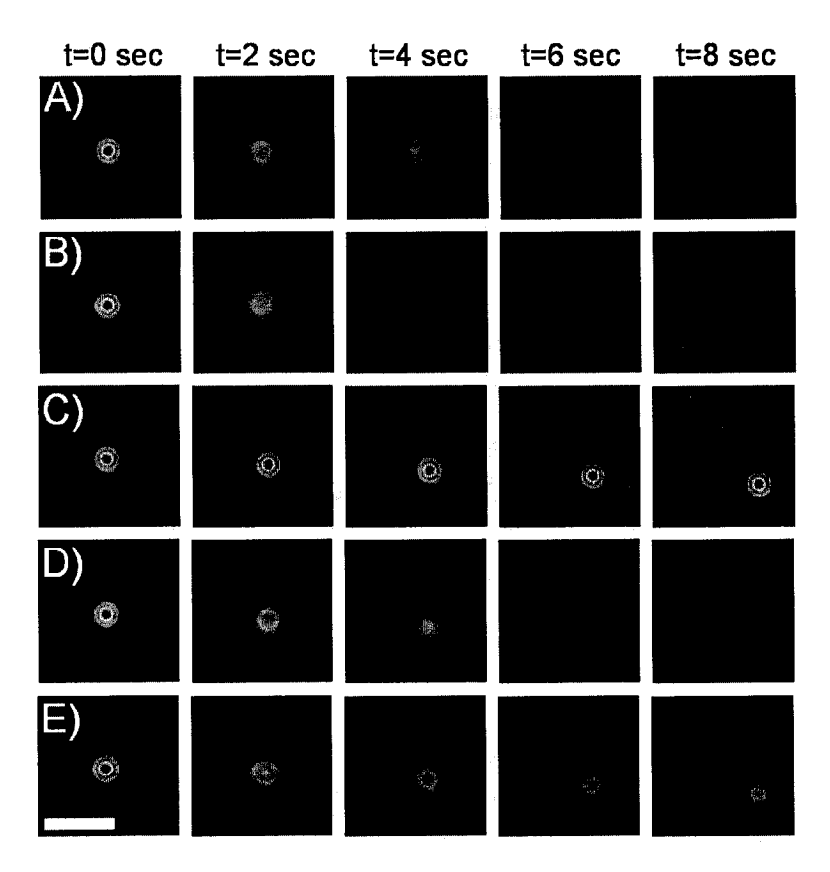


Figure 2.8: Examples of calculated STICS correlation functions for simulations of various transport dynamics behaviors. A) Diffusion with  $D=0.01~\mu m^2/s$ . B) Flow of  $|v|=0.144~\mu m/s$  with particles flowing in random directions. C) Flow of  $v_x=-0.12~\mu m/s$  and  $v_y=0.08~\mu m/s$ . D) Combined one population diffusion with  $D=0.01~\mu m^2/s$  and flow of  $v_x=-0.12~\mu m/s$  and  $v_y=0.08~\mu m/s$ . E) Two population, one with a diffusion coefficient of  $0.01~\mu m^2/s$  and the second with a flow of  $v_x=-0.12~\mu m/s$  and  $v_y=0.08\mu m/s$ . Scale bar is  $2~\mu m$ .

For an image time series collected using a LSM,  $r'_{aa}(\xi, \eta, 0)$  is the average spatial autocorrelation function from each image (Eq. 2.6 averaged for each image n in the series; see Figures 2.8 and 2.9). It will appear as a two dimensional Gaussian with peak value at  $(\xi=0, \eta=0)$  since the autocorrelation of an image with itself always yields a maximum value at zero lags. Assuming that the temporal resolution is sufficiently high for intensity fluctuations

to be correlated between successive images,  $r'_{aa}(\xi, \eta, 1)$ ,  $r'_{aa}(\xi, \eta, 2)$ , are also going to appear as Gaussian spatially distributed correlations. However, if some particles have moved between frames, the correlation function is going to change depending on the underlying microscopic motion of the particles. It is this change in shape and location of the correlation peak that directly reports the nature of the transport of the particles. We can therefore monitor the spatial evolution of the average spatial correlation function as a function of time lag by fitting it to a two dimensional Gaussian profile with variable peak position:

$$r'_{ab}(\xi, \eta, s) = g_{ab}(0, 0, s) exp \left\{ -\frac{(\xi - x(s))^2 + (\eta - y(s))^2}{\omega_{0ab}^2(s)} \right\} + g_{\infty ab}(s)$$
(2.17)

where x(s) and y(s) are the x and y coordinates of the peak of the correlation function at lag time  $\Delta t = s\delta t$  (note that all fit parameters are a function of lag time). We can monitor the transport processes by observing the evolution of the fit Gaussian peak over time.

To better conceptualize the meaning of these changes, we will consider a few thought experiments (see Figure 2.8). The simplest case is to imagine the particles as stationary, then the correlation stays unchanged for  $\Delta t=0$  to N and remains centered at ( $\xi=0$ ,  $\eta=0$ ) because there are no fluctuations in intensity. If we now consider the particles as randomly diffusing, they will tend to exit the correlation area in a symmetric fashion thus broadening the correlation peak in every direction as a function of lag time (see Figure 2.8A). This is analogous to a tracer diffusion experiment except that at lag time zero, we start with a centered Gaussian peak not a delta function.

The peak will stay centered at  $(\xi=0, \eta=0)$  but its value will decrease hyperbolically, because our discrete approximation in Eq. 2.16 evaluated at zero spatial lags is equivalent to Eq. 2.10. If we now consider particles flowing at constant speed in random directions, the Gaussian correlation is also going to spread in every direction, eventually forming an expanding "doughnut" shape for the simulation presented in Figure 2.8B. If all the particles are flowing uniformly, the spatial correlation Gaussian peak is going to maintain its original shape as a function of time, but its peak value will be shifted to lag positions  $(x(\Delta t) = -v_x \cdot \Delta t, y(\Delta t) = -v_y \cdot \Delta t)$  where  $v_x$  and  $v_y$  are the x and y velocities of the particles (see Figure 2.8C). This is due to the fact that in consecutive images the same pattern of particle distribution will occur except that it will have shifted slightly (this assumes the time resolution is sufficiently high). Hence, the correlation peak will translate between frames (see Figure 2.8C). This is consistent with the observation that for a flowing population, the temporal autocorrelation function  $r_{aa}(0,0,\tau)$  decays as a Gaussian (see Eq. 2.11). The negative signs in the expression for  $\xi$  and  $\eta$  arise from the fact that the Gaussian correlation peak moves in a direction opposite to the flow because of the order in which we correlate the images (i.e. in Eq. 2.7 we multiply the FFT of the image that comes earlier in the time series by the complex conjugate FFT of the image that comes later). This analysis is only valid as long as the particles undergoing concerted motion stay within the bounds of the analyzed region. Finally, if we analyze a single population that is undergoing both directed flow and diffusion (i.e. biased diffusion) at the same time, the Gaussian correlation peak is going to shift according to flow, but also broaden because of diffusion (see Figure

2.8D).

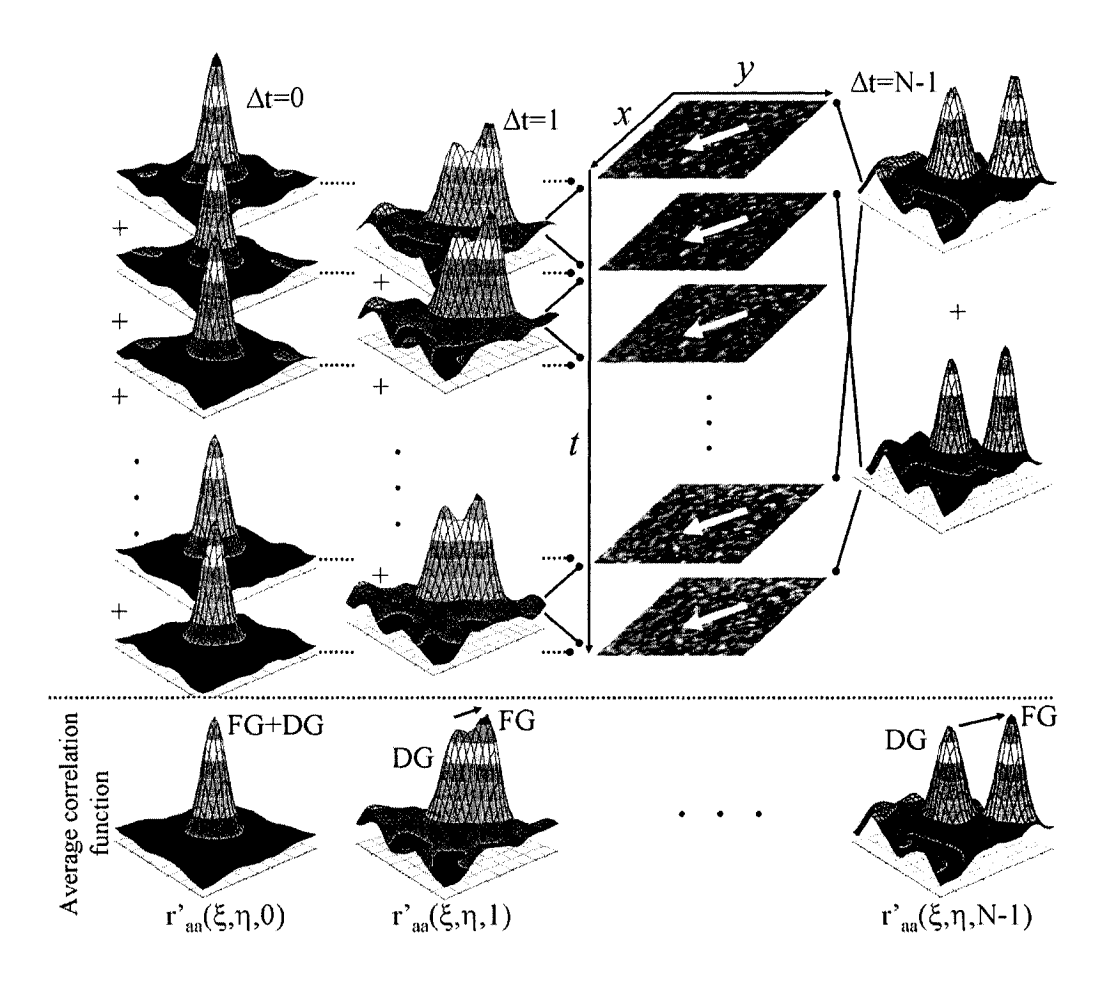


Figure 2.9: Schematic illustration of the algorithm used to compute the discrete approximation to a generalized spatio-temporal correlation function for a simulated two population system with flow and diffusion. The Gaussian autocorrelation peaks for each image are shown in the left column (s=0), the cross correlation for a lag time of 1 time unit in the middle column (s=1), and for the second longest lag time of N-1 time units in the right column (s=N-1), where N is the number of frames in the image series). The white arrows on the simulation images represent the direction of the flow. The averaged Gaussian correlation functions  $r'_{aa}(\xi,\eta,s)$  are shown at the bottom for s=0,1 and N-1. The separation of the Gaussian correlation peak due to flow (FG) from the Gaussian correlation peak arising from the diffusing population (DG) is clearly seen.

The two population case with a flowing and a diffusing population is illustrated in Figure 2.8E and 2.9, where the correlation peak due to diffusion (DG) broadens and stays centered at ( $\xi$ =0,  $\eta$ =0) and the correlation peak due to flow (FG) shifts in a direction opposite to the flow of the particles (as indicated by the white arrows on the simulated images in Figure 2.9). In this simulation the flowing and diffusing populations were equally represented in terms of density and intensity. However in cell systems that are usually studied, the actively transported protein sub-population is usually a small fraction of the total dynamic and static protein species present. This makes tracking the flow Gaussian peak difficult because it is hard to resolve near the zero lags origin due to the correlations of the slowly diffusing and immobile populations. A solution to this problem is presented in the next subsection.

# 2.7 Immobile Population Removal in STICS Analysis

The most general case of cellular protein transport is a combination of diffusion, flow and immobile populations. The challenge of applying STICS in living cells is to measure the velocity by following the flow Gaussian correlation peak, without being influenced by the correlations of the immobile or slowly diffusing populations (which effectively remain centered at (0,0)spatial lags). The immobile population contribution to  $r'_{aa}(\xi, \eta, s)$  can be removed by Fourier filtering in frequency space the zero, or low frequency components for every pixel trace in time before running the space-time correlation analysis.

#### 2.7.1 Zero Frequency Filtering

The intensity values in detection channel a for a given pixel value,  $i_a(0, 0, t)$ , contain contributions to the signal of interest from dynamic and immobile component signals and spurious noise sources. The signal from the dynamic components (flow and diffusion) contribute intensity fluctuations that change as a function of time for a given pixel trace. However, an immobile component only adds a constant intensity offset to the single pixel intensity trace through time because, by definition, the immobile component does not move so its intensity contribution to the pixel does not fluctuate in time. Removing the DC (zero) frequency component eliminates this contribution from the correlation analysis. For a given pixel location (x,y) the corrected intensities  $i'_a(x,y,t)$  are given by:

$$i'_a(x, y, t) = F_f^{-1} \{ F_t(i_a(x, y, t)) \times H_{\frac{1}{T}}(f) \}$$
 (2.18)

where T is the total acquisition time of the image series,  $H_{\frac{1}{T}}(f)$  is the Heaviside function which is 0 for  $f < \frac{1}{T}$  and 1 for  $f \ge \frac{1}{T}$ ,  $F_t$  denotes the Fourier transform with respect to t,  $F_f^{-1}$  denotes the inverse Fourier transform with respect to f, and f is the pixel temporal frequency variable.

#### 2.7.2 Windowed Average Filtering

The advantage in using the formulation of Eq. 2.18 is that we can modulate the range over which we perform the filtering in frequency space. The Heaviside function used to eliminate the zero frequency component can be modified to include non-zero components, for example using  $H_{\frac{1}{T-1}}(f)$ ,  $H_{\frac{1}{T-2}}(f)$ , etc...

This is equivalent to applying a window average filter to the raw data:

$$i_a'(x,y,s) = i_a(x,y,s) - \left(\frac{1}{2 \times \Delta N + 1} \sum_{n=s-\Delta N}^{s+\Delta N} i_a(x,y,n)\right) + \langle i_a(x,y,s) \rangle_t$$
(2.19)

where  $2 \times \Delta N + 1$  is the filtering window size. The first term in Eq. 2.19 is the intensity at location (x,y) and discrete frame time s, from which we subtract the second term which is the average intensity in a window centered around time s. The last term in Eq. 2.19 is added as a constant offset to prevent the temporal ACF from diverging when we divide by the average intensity. Without this last term, we would have  $\langle i'_a(x,y,s)\rangle = 0$  and so the denominator in Eq. 2.9 would be null. Also note that this last term will make the correlation function decay to 1 at infinite lag times, and not to 0 as is usually the case for Eq. 2.9 (if there is no immobile population).

This method can be used if there are slow variations in intensity that are not part of the signal. Any low frequency "noise", such as a vesicle slowly moving through the field of view, will be removed. However, this technique introduces artificial correlations in the data because of the inherent use of a window to compute the average to be subtracted from the data. It is easiest to understand this with an example. Assume  $\Delta N = 1$  (window size of 3), dropping the channel subscript a to simplify the notation, and assuming we select a specific pixel location  $(x_0, y_0)$ :

$$i'(s)_{x_0,y_0} = i(s)_{x_0,y_0} - \frac{1}{2 \times \Delta N + 1} \sum_{n=s-\Delta N}^{s+\Delta N} i(n)_{x_0,y_0} + \langle i(s)_{x_0,y_0} \rangle_t$$
 (2.20)

or more simply (since  $\Delta N = 1$ ):

$$i'(s) = \frac{2}{3}i(s) - \frac{1}{3}i(s-1) - \frac{1}{3}i(s+1) + \langle i \rangle$$
 (2.21)

$$= \begin{bmatrix} i(s-1) & i(s) & i(s+1) & \langle i \rangle \end{bmatrix} \cdot \begin{bmatrix} -\frac{1}{3} \\ \frac{2}{3} \\ -\frac{1}{3} \\ 1 \end{bmatrix}$$
 (2.22)

the matrix notation simplifies the generalized form for the multiplication of the new intensity at time t and the new intensity at time  $t+\tau$ :

$$i'(s)i'(s+\tau) = \begin{bmatrix} i(s-1) & i(s) & i(s+1) & \langle i \rangle \end{bmatrix} \cdot (2.23)$$

$$\underbrace{\begin{bmatrix} \frac{1}{9} & -\frac{2}{9} & \frac{1}{9} & -\frac{1}{3} \\ -\frac{2}{9} & -\frac{4}{9} & \frac{1}{9} & \frac{2}{3} \\ \frac{1}{9} & \frac{1}{9} & \frac{1}{9} & -\frac{1}{3} \\ -\frac{1}{3} & \frac{2}{3} & -\frac{1}{3} & 1 \end{bmatrix}}_{\text{matrix } \mathbf{A}} \cdot \begin{bmatrix} i(s+\tau-1) \\ i(s+\tau) \\ i(s+\tau+1) \\ \langle i \rangle \end{bmatrix}$$

where matrix **A** is obtained by the vector multiplication of the coefficients column vector in Eq. 2.22. The new autocorrelation function  $g'(\tau)$  for the single pixel location is now given by:

$$g'_{x_0,y_0}(\tau) = \frac{\langle i'(t)i'(t+\tau)\rangle}{\langle i\rangle}$$
 (2.24)

since  $\langle i' \rangle = \langle i \rangle$ . Plugging Eq. 2.23 into Eq. 2.24 we see that the new correlation function at lag  $\tau$  is going to be a combination of the old correlation

function at lags  $\tau-2,\,\tau-1,\,\tau,\,\tau+1$  and  $\tau+2.$  In our case:

$$g'(\tau) = \frac{1}{9}g(\tau - 2) - \frac{4}{9}g(\tau - 1) + \frac{2}{3}g(\tau) - \frac{4}{9}g(\tau + 1) + \frac{1}{9}g(\tau + 2) + 1 \quad (2.25)$$

where the coefficients are obtained by summing the diagonal elements of the submatrix constituted by the first  $3\times3$  elements of matrix **A**.

In Eq. 2.25 it can be seen that the filtered correlation function at time lag  $\tau$  includes contributions from other time lags. In a practical manner, this process can be generalized to any window size by realizing that the coefficients weighting the old correlation functions at other lag times in Eq. 2.25 are actually the convolution of the coefficient column vector in Eq. 2.22. In essence, Eq. 2.25 provides an analytical form to fit the temporal autocorrelation function obtained when we analyze window filtered data.

# 2.8 Chapter Conclusions

In this chapter, the theoretical basis of the fluorescence phenomenon was introduced through use of the Jabloński energy diagram for fluorescent molecules, and the central aspects of fluorescence important for optical microscopy were outlined. The major tools for fluorescence imaging of biological systems, namely confocal, two-photon and total internal reflection microscopy, were introduced. Finally, the basis of fluorescence correlation techniques, namely FCS and ICS, were introduced. The theoretical basis of the STICS method was introduced and the response of the method to different forms of transport was shown via analysis of simulations. In the following chapter, we will

review the materials and methods used for characterizing STICS  $in\ silico$  and  $in\ vivo$ .

# 3 Materials and Methods

#### 3.1 Microscopy Instrumentation

#### 3.1.1 Wide Field Fluorescence Microscopy

Fish epidermal keratocyte cells were imaged in a cell incubation chamber on a Nikon Diaphot 300 inverted microscope at room temperature using a 40× (NA=1.3) or a 60× (NA=1.4) objective. Metamorph version 6.1 (Molecular Devices, Sunnyvale, CA) was used to drive the filter wheels and shutters. Images were collected on a cooled CCD camera (Princeton Instruments, Trenton, NJ), with a 2× optivar attached. For tracer flow measurements, phase images were acquired before and after acquisition of a fluorescence image series of 150-300 frames at a frame rate of 3-10 frames/s, using exposure times of 50 ms (for QDs) or 100-200 ms (for GFP). The 655 QDs (Quantum Dot Corporation, Hayward, CA) were visualized with Texas Red chromatic filters, and the 545 QDs (Quantum Dot Corporation, Hayward, CA) and GFP with FITC chromatic filters (Chroma, Rockingham, VT). Phase and fluorescence images were acquired at a frame rate of 0.5 frames/s, with a Rhodamine chromatic filter (Chroma, Rockingham, VT).

#### 3.1.2 Confocal Microscopy

Confocal images of cells were acquired on an Olympus Fluoview 300 microscope (Olympus, Melville, NY) equipped with an IX70 inverted microscope fitted with a 60× PlanApo (1.40 NA) oil immersion objective. Excitation was from the 488 nm laser line of a 40 mW Ar ion laser (Melles Griot, Carlsbad, CA) attenuated to 0.1-0.2% power using a ND filter and an acousto-optical

tunable filter. The photomultiplier tube was operated at 800 V with  $1 \times \text{gain}$ , and 0% offset. In order to get high resolution images  $(0.023 \ \mu\text{m/pixels})$  we used a clip box subregion of  $256 \times 256$  pixels from a  $1024 \times 1024$  image at  $10 \times \text{zoom}$ . A custom Q500LP dichroic mirror (Chroma, Rockingham, VT) was used for the laser excitation and for collection of the fluorescence emission. Note that use of this filter enhanced the EGFP signal by about 50% over the standard triple dichroic that comes with the FV300. Under these conditions the pixel dwell times were  $2 \ \mu\text{s/pixel}$  (fast scan),  $4 \ \mu\text{s/pixel}$  (medium scan) or  $8 \ \mu\text{s/pixel}$  (slow scan), and the time between lines was  $1.608 \ \text{ms}$  (fast scan),  $2.12 \ \text{ms}$  (medium scan), and  $3.15 \ \text{ms}$  (slow scan).

#### 3.1.3 Two-Photon Microscopy

Two-photon microscopy of the fluorescent microspheres was conducted using an Olympus Fluoview 300 CLSM/IX70 inverted microscope (Olympus, Melville, NY), coupled with a Tsunami (model 3960) pulsed femtosecond Ti:sapphire laser (Spectra Physics, Mountain View, CA) pumped by a Millennia XsJS laser. The microspheres were excited at 800 nm and point detection was achieved with two external PMTs (Hamamatsu, Bridgewater, NJ). For imaging of the microspheres, a 720 DCSPXR excitation dichroic mirror, a 555dclp emission beam splitter, and HQ525/50 HQ610/75 emission filters (all from Chroma Technology Co., Brattleboro, VT) were employed for light detection. All images were collected using a PlanApo Olympus 60× (NA 1.40) oil immersion objective lens. Images were collected with a typical optical zoom setting of  $2\times$  corresponding to x and y pixel dimensions of 0.23  $\mu$ m/pixel. Image time series of 100 frames with a time delay of 0.45 s between frames were collected.

61

Two-photon imaging of cells was conducted using a Biorad RTS2000MP video rate capable two-photon/confocal microscope (Biorad, Hertfordshire, UK), coupled with a MaiTai pulsed femtosecond Ti:sapphire laser (Spectra Physics, Mountain View, CA) tunable over a range from 780-920 nm. The microscope used a resonant galvanometer mirror to scan horizontally at the NTSC line scan rate. Point detection was employed using one or two photomultiplier tube(s) with fully open confocal pinholes when imaging. For imaging EGFP in cells, the laser was tuned to a wavelength of 890 nm and a 560 DCLPXR dichroic mirror and an HQ528/50 emission filter were employed for light detection. For imaging cells expressing both ECFP and EYFP fusion proteins, the laser was tuned to 880 nm and a D500LP dichroic mirror and HQ485/22 and HQ560/40 emission filters were used for detection and separation of the emitted fluorescence. All laser filters were from Chroma Technology Co. (Brattleboro, VT). All image time series were collected using a PlanApo Nikon  $60 \times$  oil immersion objective lens (NA 1.40) which was mounted in an inverted configuration. Images having dimensions of 480 (height) by 512 (width) pixels were collected with a typical optical zoom setting of 2× corresponding to x and y pixel dimensions of 0.118  $\mu$ m/pixel. Image series with time delays of 1, 5, or 10 s between sequential frames and 60, 120 or 150 frames in total were collected from single cells. Individual image frames sampled from the cells were accumulated as averages of 32 video rate scans (i.e. approximately 1 s/frame).

#### 3.1.4 Total Internal Reflection Microscopy

TIRM microscopy was performed on an Olympus IX70 microscope equipped with an Olympus TIRM illumination arm and a PlanApo 60× (1.45 NA)

TIRM oil immersion objective (Olympus, Melville, NY). The laser launch (Prairie Technologies, Inc., Middleton, WI) was connected to the TIRM Illumination arm via a fiber optic and illumination was from the 488 nm line of a 200 mW Ar Ion laser or the 543 nm line of a 2 mW HeNe green laser. The 488 nm laser line was attenuated to 10% of incident power with a ND1 filter and further attenuated with the AOTF (Acousto-Optic Tunable Filter) to give a total power of about 1% of incident power. The HeNe green laser was used at full power, i.e. no ND filter and the AOTF. Images were collected on a Retiga EXi camera (QImaging, Burnaby, BC, Canada) with  $2\times 2$  binning to give a pixel resolution of 0.2146  $\mu$ m. Exposure times were typically 500 - 1000 ms. For EGFP and RFP dual imaging, the images were collected sequentially using MetaMorph software (Molecular Devices Corporation, Downingtown, PA), the AOTF control of the laser lines and a LUDL (LUDL Electronics Products Ltd., Hawthorne, NY) emission filter wheel controlled by a MAC2000 control unit. Fluorophores were excited sequentially and typically the image with the lower exposure time was collected first to reduce the delay between successive frames. Imaging was done using custom dichroic filter sets designed by Chroma Technologies for use with TIRM microscopy and lasers at a high incidence angle. For EGFP imaging, an HQ485/30 dichroic filter was used in combination with a 535/30 bandpass emission filter. For dual EGFP/RFP imaging a z488/543rpc dual dichroic was used in combination with a z488/543 dual band pass emission filter in the cube and a 535/30 or 630/60 emission filter to select either EGFP or RFP emission. This leads to double filtering of the light causing some loses, but it is a safer design for the end microscope user as it avoids having reflected laser light at the eyepiece.

# 3.2 Image Auto-Correlation and Cross-Correlation Analysis

Microscope image time series data sets were viewed, and image sub-regions of 16<sup>2</sup>, 32<sup>2</sup>, 64<sup>2</sup>, 128<sup>2</sup> or 256<sup>2</sup> pixels in size were selected that covered areas of the cell. These image sub-stacks were exported for image correlation analysis using a custom Interactive Data Language (IDL 6.0, RSI Colorado) program written for the PC. Correlation calculations for all image time series and nonlinear least squares fitting of the spatial correlation functions were performed in a Windows environment on a PC using programs written in IDL. Discrete intensity fluctuation autocorrelation functions were calculated from the image sections as described in sections 2.5 and 2.6. The equations used for the calculation and fitting of the normalized intensity fluctuation autocorrelation and cross-correlation functions (both spatial and temporal) have been described in section 2.5.

#### 3.3 Cell Culture

#### 3.3.1 Plasmids

The  $\alpha$ -actinin-EGFP, paxillin-EGFP, and  $\alpha$ 5-integrin-EGFP plasmids have been previously described [100]. The plasmids for  $\beta$ -actin-RFP and talin-EGFP were generous gifts from the laboratories of Frank Gertler (Massachusetts Institute of Technology) and Ken Yamada (National Institutes of Health), respectively.

3.3 Cell Culture 64

#### 3.3.2 Cell culture of the 3T3, MEF and CHO lines

CHO, MEF and 3T3 cells were cultured in a humidified, 8.5% CO<sub>2</sub> atmosphere at 37°C in minimum essential medium (MEM) supplemented with 10% FBS, non-essential amino acids, and glutamine. For stable cell lines 0.5 mg/mL neomycin (G418) was added to the media for cell selection. Cells were transfected 24 to 48 hours before imaging with 0.1  $\mu$ g of DNA for a given EGFP protein and 0.9  $\mu g$  of BlueScript empty vector (Stratagene, La Jolla, CA). Titrating down the EGFP protein DNA with BlueScript DNA decreases the number of cells that highly overexpress the EGFP protein, however it is important to maintain the total DNA concentration at 1  $\mu$ g or the transfection efficiency is markedly reduced. For dual transfections 0.1  $\mu g$  of DNA for each fluorescently tagged protein was added with 0.8  $\mu g$  of BlueScript DNA. The DNA was mixed with 5  $\mu$ L of lipofectamine reagent (Invitrogen, Carlsbad, CA) in PBS and left to sit for 20 minutes. Cells were plated in 6 well tissue cultures the day before transfection so that they were 40-60% confluent. Cells were washed two times with serum free medium and then the lipofectamine and DNA solution was mixed with 600 ml of serum free medium and applied dropwise to each well. The cells were placed at 37°C for 3-4 hours and then washed two times and left in serum containing medium overnight. Cells were lifted with trypsin and plated in CCM1 medium (Hyclone, UT) buffered with 15 mM HEPES on homemade 35 mm glass bottomed dishes coated with an integrin activating extracellular matrix protein 2  $\mu$ g/mL fibronectin (Sigma, Munich, Germany) and maintained at 37°C during imaging with a Warner Instruments heated stage insert (Warner Instruments, Hamden, CT) and a Bioptechs (Bioptechs, Butler, PA) objec3.3 Cell Culture 65

tive heater. Non-transfected cells were used as control samples to determine autofluorescence background levels.

Cell samples that had been fixed with 4% paraformaldehyde in PBS for 10 minutes at room temperature were also prepared for each type of migratory cell line studied (3T3s, MEFs and CHOs). The chemically fixed cells were imaged to provide a control for any contributions from mechanical vibrations, stage translations, and laser fluctuations.

#### 3.3.3 Keratocyte cell culture

Keratocytes were isolated from the scales of the central American cichlid Hypsophrys nicaraguensis as described [101] with the exception that the scales were sandwiched between two 25 mm acid-washed glass coverslips. Cells were cultured in Leibovitz's L-15 medium (Gibco BRL) supplemented with 14.2 mM HEPES pH 7.4, 10% FBS and 1% antibiotic-antimycotic (Gibco BRL) and used within 1-3 days of isolation. 5 kD methoxy PEG 655 or 545 QDs (Qtracker, Quantum Dot Corporation), purified His-tagged GFP (gift from J. Dawson) or Alexa Fluor 546-conjugated phalloidin (AF546phalloidin, Molecular Probes), were introduced into living keratocytes using a small volume electroporator for adherent cells [102]. Cells were placed in a 35 mm dish in 1 mL of culture media, and drops of the fluorescent probe diluted in 20  $\mu$ L of water were placed directly onto the cell samples. The 655 or 545 QDs were used at 0.2-2 M and GFP was used at 160 M. In some cases a volume marker (AF488, Molecular Probes) was also included. AF546phalloidin was used to visualize F-actin dynamics [103]. AF546-phalloidin was used at 2 M and pre-mixed with 7.5 M d-ATP, 7.5 M d-GTP, and 5 M

66

d-CTP in water for  $\sim 15$  min at room temperature before electroporation to prevent aggregation. Following electroporation, the cells were allowed to recover in culture media for at least 10 min before viewing on the microscope. To obtain single isolated cells, sheets of keratocytes could be dispersed by incubating for  $\sim 5$  min in 85% PBS/2.5mM EGTA pH 7.4.

### 3.4 Computer Simulations

Computer simulations of image time series were used to model and test the STICS analysis algorithms via comparison with the expected (set) results for different particle transport property, settings and collection conditions. This facilitated direct comparison of simulation with results from the experimental measurements. An Interactive Data Language program (IDL 6.0, RSI, Colorado) was written to simulate data that would be obtained by laser scanning microscopy of point emitters in a 2D system under defined settings of instrument collection and particle mobility. The program allowed a wide range of system parameters to be defined including flow speed and direction of the simulated particles on the 2D surface, characteristic diffusion times, densities of multiple populations of particles, laser beam focal area size and shape characteristics, size of confinement domains in the 2D lattice, image size, pixel size, the number of images collected for analysis and the time interval between images. The adjustable parameters are shown in Table 3.1 along with a range of typical values for a normal experiment. The simulations were run on a standard desktop PC.

symbol	description	typical values
$\Delta x$	pixel spatial resolution	$0.05$ - $0.2~\mu{\rm m}$
$\Delta \mathrm{t}$	imaging temporal resolution	0.01-15 s/frame
ho	particle density	$0.1\text{-}100 \text{ particles}/\mu m^2$
D	diffusion coefficient	$0.001 \text{-} 0.05 \ \mu m^2/\mathrm{s}$
$v_x$	x velocity of the particles	$0.1\text{-}1.0~\mu\mathrm{m/min}$
$v_y$	y velocity of the particles	$0.1$ - $1.0~\mu\mathrm{m/min}$
$N_x$	x size of ROI	16-128 pixels
$N_y$	y size of ROI	16-128 pixels
N	number of images in time series	10-300
$d_x$	confinement domain size in $x$	$0.1$ -1 $\mu\mathrm{m}$
$d_y$	confinement domain size in y	$0.1$ -1 $\mu\mathrm{m}$
$ au_{bleach}$	characteristic photobleaching time	1-30 s
$\omega$	$e^{-2}$ laser beam size	$0.2\text{-}0.4~\mu\mathrm{m}$
S/N	signal to noise ratio	2-10

**Table 3.1:** Adjustable parameters in the computer simulation of two dimensional laser scanning microscopy of point emitters.

For all simulations, periodic boundary conditions were used at the image edges. For diffusion, discrete displacements in x and y were computed at every time step for each particle using normally-distributed, floating-point, pseudo-random numbers having a mean of zero and standard deviation  $\sigma = \sqrt{2Dt}$ . For flow, a deterministic displacement in x and y was computed from the input velocity and added to each particle's x and y positions at every time step. To simulate several populations with different transport dynamics, single population movies were combined by addition and the total intensity was scaled to simulate 8-, 12- or 16-bit acquisition. It is important to note that scaling the intensity values of the simulated data by a constant factor does not alter the correlation function (see Eq. 2.5), thus we were free to multiply the intensity by a scaling factor but could not add a constant value to the intensities. Another advantage of this scaling property is that

clustering can also be simulated by weighted addition of two image series, where the clustered population intensities would be multiplied by a scaling factor proportional to the number of subunits in the cluster (or to a certain fraction of that value to simulate self quenching during the aggregation processes). To simulate the scanning of the sample with the focus of a  $TEM_{00}$  laser beam, we convolved the image of point emitters (single pixels) with a kernel consisting of a two-dimensional Gaussian function with characteristic  $e^{-2}$  radius  $\omega$  as input (see Figure 3.1). Convolution is done through the product of Fourier transforms in reciprocal space, thus we chose image sizes that are powers of 2 in order for this convolution step to be computed quickly.

The signal to noise ratio (S/N) is usually defined as the ratio of the average signal value to the standard deviation of the background noise. To simulate background noise, a square matrix  $\mathbf{N}$  of the same dimensions as the image  $(L_x \times L_y)$  with normally distributed random numbers was generated. The mean of the distribution was zero and its standard deviation was one, the absolute values of the numbers were taken and this noise matrix  $\mathbf{N}$  was added to the image matrix. This simulated the case where the mean background intensity is subtracted from each pixel leaving residual background counts that are greater than the mean in each pixel. This average background correction is standard practice for quantitative fluorescence microscopy. A variable scaling coefficient, S/N, is used as an adjustable standard deviation parameter that allowed control of the magnitude of the signal to noise ratio. The new intensity at a given pixel location  $(\mathbf{x}, \mathbf{y})$  after background noise

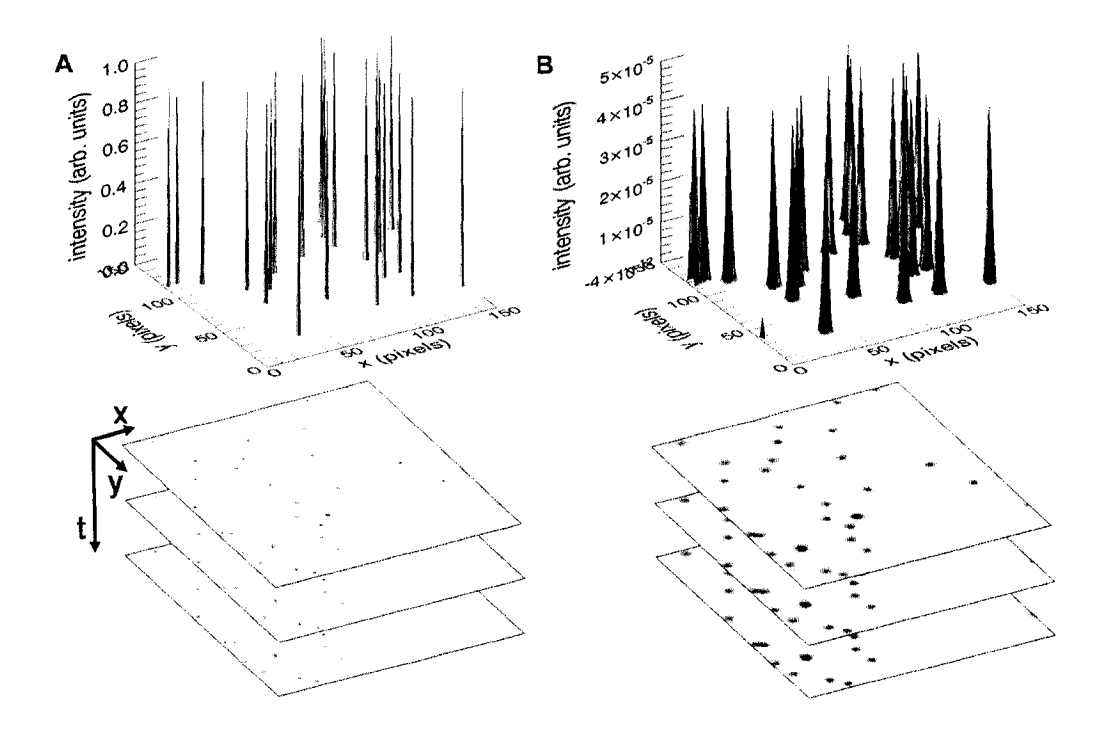


Figure 3.1: Generation of the simulated LSM images. A) particles are randomly placed as delta functions on a 2D lattice (here a 150×150 pixel image). B) The grid is then convolved with a 2D Gaussian function, which simulates the scanning of the particles with a focused  $TEM_{00}$  laser beam. The process is repeated over time as we displace the particles according to their simulation defined dynamics (i.e. diffusion or flow) to generate the image time series.

addition is given by:

$$i'(x, y, t) = i(x, y, t) + S/N \times \mathbf{N}(x, y)$$
(3.1)

Using this definition the signal to noise ratio is defined as:

$$S/N = \frac{max[i(x, y, t)]}{\sigma}$$
 (3.2)

For the computer simulations presented in this thesis, the parameters were set

to be close to what one would use or measure in the actual cell experiments. The alternative would be to express some parameters as dimensionless quantities like the velocity in pixels per frame, the density in number per pixel<sup>2</sup>, etc. However, since the numerical ranges for the simulation parameters were chosen close to actual experimental parameters, it was found more useful for direct comparison purposes to keep the real units for most of the cases presented in this thesis.

# 3.5 Vector Flow Fields Comparison for Two Population Measurements

In cases where two populations of labeled proteins are not undergoing perfectly concomitant directed motion, the STICCS analysis will not reveal correlated flows because the particles are not moving entirely together. Hence it will not be possible to track a cross-correlation Gaussian flow peak. To handle these situations, which frequently arise in cell measurements, we applied two scores to assess the degree of similarity between two velocity fields. The first is the correlation coefficient between the magnitudes of the velocities which reflects the degree of engagement or binding of the two proteins, and second is the correlation between the directions of the velocity vectors for each region of interest.

Figure 3.2A-B shows two simulated flow fields. The first one was generated with x and y velocity values that increase towards the upper right corner of the frame. The second flow field was generated using the first field,

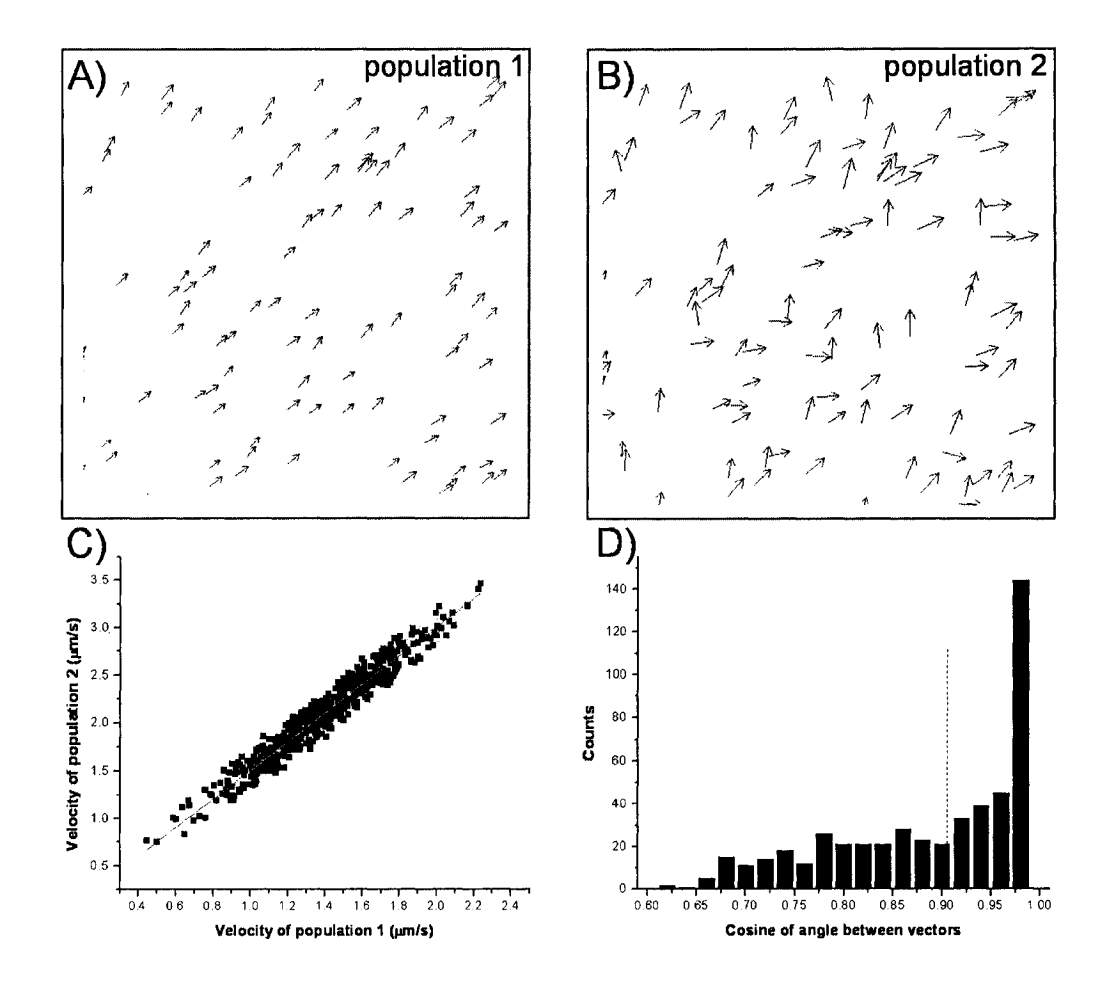


Figure 3.2: Similitude scoring of two flow fields. A) Velocity field generated with increasing x and y velocity values towards the upper right corner of the figure. B) Velocity field generated by adding angle and magnitude randomness to the first flow field, with the magnitudes on average 1.5× larger. C) Magnitude correlation plot. D) Histogram of the cosine values for the angles between all velocity field vectors (dashed line indicates median).

and adding randomness in angle and magnitude. The angles were varied by adding angles with a random uniform distribution between [-45,+45] degrees. The x and y velocity magnitudes were multiplied by a factor of 1.5, and then randomness was introduced by adding a uniformly distributed number be-

tween  $[-0.2,+0.2] \mu m/s$  to these new magnitudes.

The correlation in magnitude is clearly shown in Figure 3.2C, and the slope of the line was found by linear regression to be  $1.503 \pm 0.003$  which recovers the multiplying factor set in the simulation. The directional correlation is defined as the median of the cosine values calculated from the dot product formula:

directional correlation score = median
$$[cos(\Theta)]$$
  
= median  $\left[\frac{\vec{v_A} \cdot \vec{v_B}}{||\vec{v_A}||||\vec{v_B}||}\right]$ 

where  $\Theta$  is the set of all angles between the velocity vectors for each population at every point,  $\vec{v_A}$  represents the set of all vectors in the first flow field,  $\vec{v_B}$  represents the set of all vectors in the second flow field. For this simulation the directional correlation score was  $0.92\pm0.01$  (see dashed bar in histogram of cosine values in Figure 3.2D). This parameter varies between -1 and 1, 1 for perfectly aligned velocity maps and -1 for velocities in opposite directions. Care has to be taken in the interpretation of the median because a single value for this score can arise from many different types of histogram distributions. The typical histogram distribution is the one showed in Figure 3.2D, since most of the vectors are aligned, the cosine values tend to be clustered towards a value of 1. For all analyses, careful attention was paid to the shape of the histogram. The error on the median was estimated using the bootstrap method [104].

# 3.6 Chapter Conclusion

In this chapter we described the computer simulations that will be used to test the STICS technique in chapter 4. We have also outlined the methods that will be applied to the culture, transfection and microscopy imaging of cells used in chapters 5 and 6. The next chapter will make use of the computer simulations of various biologically relevant cases to test the dynamic range and accuracy of STICS.

# 4 In Silico Characterization

#### 4.1 Introduction

The principal paradigm of science is that a theory can only be true if it is falsifiable, i.e. if there are situations in which it can be tested by experiments. One of the challenges of working with living cells lies in the fact that there are so many uncontrolled and interconnected parameters, which makes it difficult to reliably test biophysical theories. However, it is possible to model components of biological systems and this approach is adopted to study processes such as protein folding [105] and macromolecular transport in biological systems [106]. An advantage of studying membrane protein dynamics by fluorescence microscopy is that the proteins can easily be modeled in computer simulations as point emitters diffusing and flowing in a two dimensional system (i.e. the cell membrane) or a three dimensional system (i.e. the cytoplasm). This chapter will present computer simulations of LSM imaging of point emitters in a 2D system and their analysis with ICS and STICS, under set simulation conditions of photobleaching, signal to noise, immobile population removal by Fourier filtering, and different ratios between the characteristic diffusion and flow times for the particles. The simulations are intended to model transport in a 2D membrane system which is what we are interested in for STICS measurements of membrane and membrane associated adhesion proteins. Using the computer simulations, the sensitivity and detection limits of STICS for such applications will be explored in this chapter as a function of collection parameters and system transport properties. It will be shown that given the proper spatio-temporal sampling, STICS can

extract the velocities of labeled proteins in many situations typical of what is encountered when imaging cells.

#### 4.2 STICS characterization

#### 4.2.1 Photobleaching

During the acquisition of a fluorescence image time series, the fluorophore will usually undergo photobleaching due to laser irradiation and be photochemically converted to a non-fluorescent state. Due to photobleaching, the mean intensity of the images will decrease over time as fluorophores randomly convert to a non-emitting state. After transition from an excited singlet state to an excited triplet state (see Figure 2.1), the fluorophore may react with another molecule to produce irreversible covalent modifications. Since the triplet state is relatively long-lived with respect to the shorter lifetime singlet state, the excited fluorophore has a much longer time to undergo chemical reactions with components in the environment if it is residing in an excited triplet state. Photobleaching will be dependent on several parameters such as laser intensity, the nature of the fluorophore and the chemical environment. However, a characteristic of any fluorophore in a given environment is the average number of excitation and emission cycles that can occur before photobleaching. Some fluorophores bleach quickly after emitting only a few photons, while others that are more robust can undergo millions of cycles before bleaching. In a real experiment, the laser intensity has to be adjusted so that the fluorophores do not bleach excessively on the time scale of the image series collection, while still providing enough contrast (signal) in the images for correlation analysis. The process of fluorescence bleaching and the

77

resulting decrease in image intensity can often be fit with a mono-exponential decay using:

$$\langle i(x, y, t) \rangle_{x,y} = \mathbf{A}exp(-t/\tau_{bleach}) + \mathbf{B}$$
 (4.1)

where A, B and  $\tau_{bleach}$  are fitting parameters, thereby providing a measure of the characteristic bleaching time  $\tau_{bleach}$ .

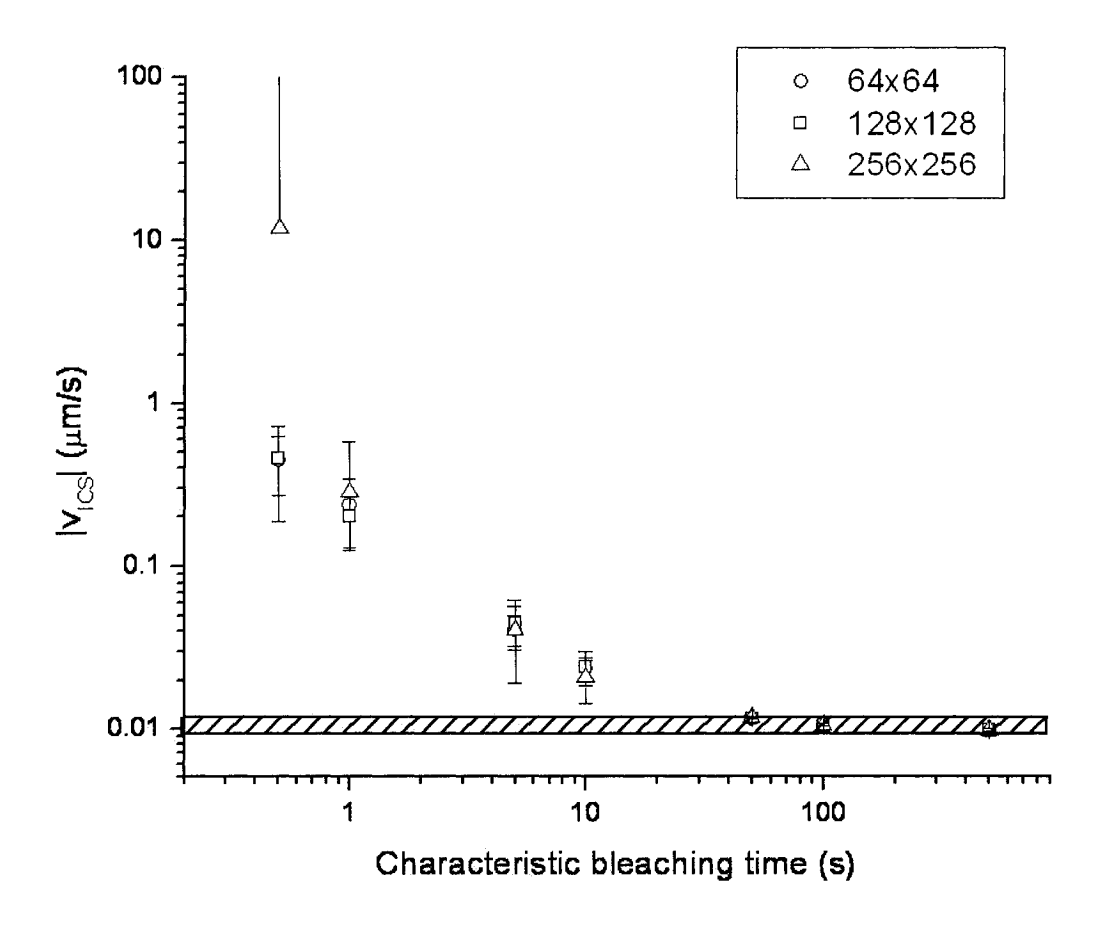


Figure 4.1: Effects of photobleaching rates on the ICS measured velocity magnitude for varying image size. Each point and error bar represents the average result of 100 simulations and standard deviation. The shaded region shows the set velocity in the simulations ( $v_x$ =0.01  $\mu$ m/s corresponding to  $\tau_{flow}$ =30 s) and a band of acceptable error of  $\pm$ 10%.

78

To investigate the effects of photobleaching on our correlation techniques, a series of computer simulations were run to generate image series of a single flowing population of particles. The Gaussian convolution radius was set at 0.3  $\mu m$  and the velocity of the particles was kept constant at  $v_x = 0.01 \,\mu\text{m/s}$  so that the characteristic flow time was 30 s. The computer simulated images were 64 by 64, 128 by 128 or 256 by 256 pixels with 300 frames at a density of 10 particles/ $\mu m^2$ , using 0.5 s/frame and 0.1  $\mu$ m/pixel. The characteristic bleaching time  $\tau_{bleach}$  was varied from 0.5 to 500 s so that it would cover a range of values both smaller and larger than the characteristic flow time.

Figure 4.1 shows that at high photobleaching rates (short photobleaching characteristic times) ICS cannot recover the correct set value for the velocity of the particles. In fact, it can be systematically off from the set velocity in the simulation by as many as 2 to 3 orders of magnitude. The reason for this error is the decay in the correlation function is due mainly to the loss of intensity due to photobleaching on the short time scale, not from the variation due to particles coming in and out of the observation volume. The recovered velocity value becomes acceptable (less than 10% deviation) when  $\tau_{bleach}$  is just above 50 seconds, i.e. when the bleaching time becomes about twice as large as the characteristic flow time, as would be expected. In this regime, the fluctuations in intensity between adjacent frames in the image time series are due mostly to the dynamic fluctuations of the particles rather than the photobleaching of the fluorophores.

In contrast to the ICS measurements, Figure 4.2 shows that STICS is not affected unless the bleaching rate is very high. For example at a characteristic

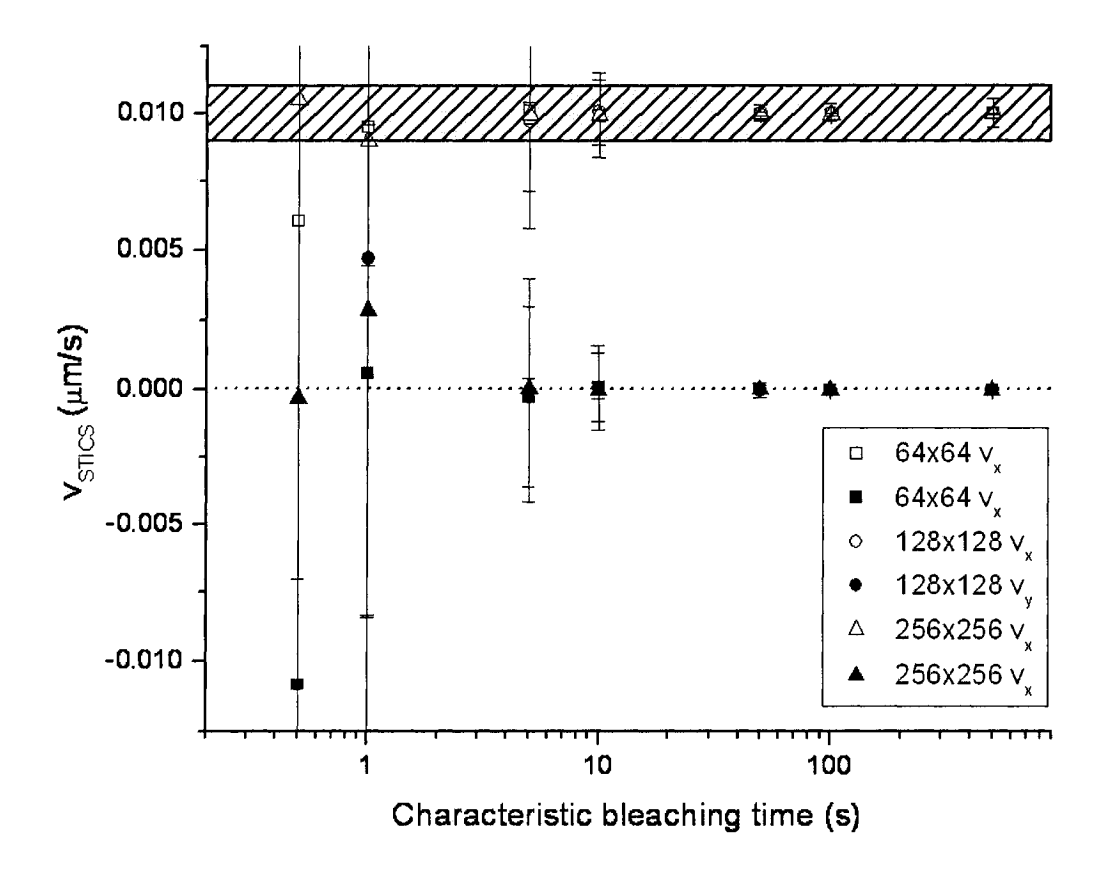


Figure 4.2: Effects of photobleaching rates on the recovered velocity magnitudes by STICS for varying image size. Each point and error bar represents the average result of 100 simulations and standard deviation. The shaded region show the set velocity in the simulation ( $v_x = 0.01 \ \mu\text{m/s}$  and  $v_y = 0 \ \mu\text{m/s}$ ) and a band of acceptable error of  $\pm 10\%$  for  $v_x$ .

bleaching time of 0.5 s, all the particles are extinguished within the first 3 to 5 frames of the time series. It would be expected that STICS would fail with the very high rates of bleaching because there are only a few valid image frames with signal. However, even at rates of photobleaching where ICS fails to recover the set velocity, STICS can still measure the correct x and y velocities. Overall, we can neglect signal fluctuations due to bleaching in ICS and STICS flow/diffusion measurements as long as the characteristic times

80

associated with these processes are shorter than the bleaching time. This was the case for all of the cell measurements reported in this work.

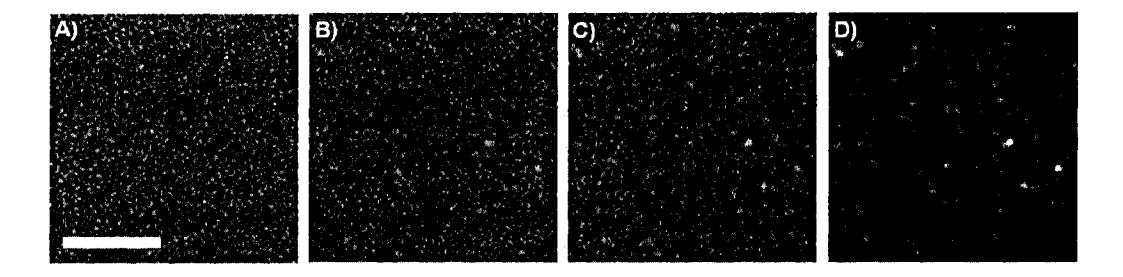


Figure 4.3: Example of simulated images with varying signal to noise ratio at a density of 0.1 particles per beam area, all particle positions are the same in these images. A) S/N=1, B) S/N=3, C) S/N=5, D) S/N=10. Scale bar is 5  $\mu m$ 

#### 4.2.2 Sampling and Signal to Noise Considerations

The spatial sampling is inherently given by the size of the selected subregion(s) in the image time series. For image correlation, the sampling statistics are related to the square root of the number of independent spatial fluctuations sampled within the subregion. The number of independent fluctuations is simply the subregion area divided by the beam focus area [7]. Additionally, for STICS velocity measurements, there is an upper limit on the maximum velocity that can be measured by STICS along the x or y axes because the flow Gaussian peak location has to be tracked within the subregion for at least one time step. The maximum velocity that can be measured along any axis is given by:

$$v_{\max x(y)} = \frac{N_{x(y)} \times \Delta x}{2 \times \Delta t} \tag{4.2}$$

where  $N_{x(y)}$  is the frame size in pixels,  $\Delta x$  is the spatial resolution ( $\mu$ m/pixel), and  $\Delta t$  is the time resolution (s/frame) of the image time series. For a small

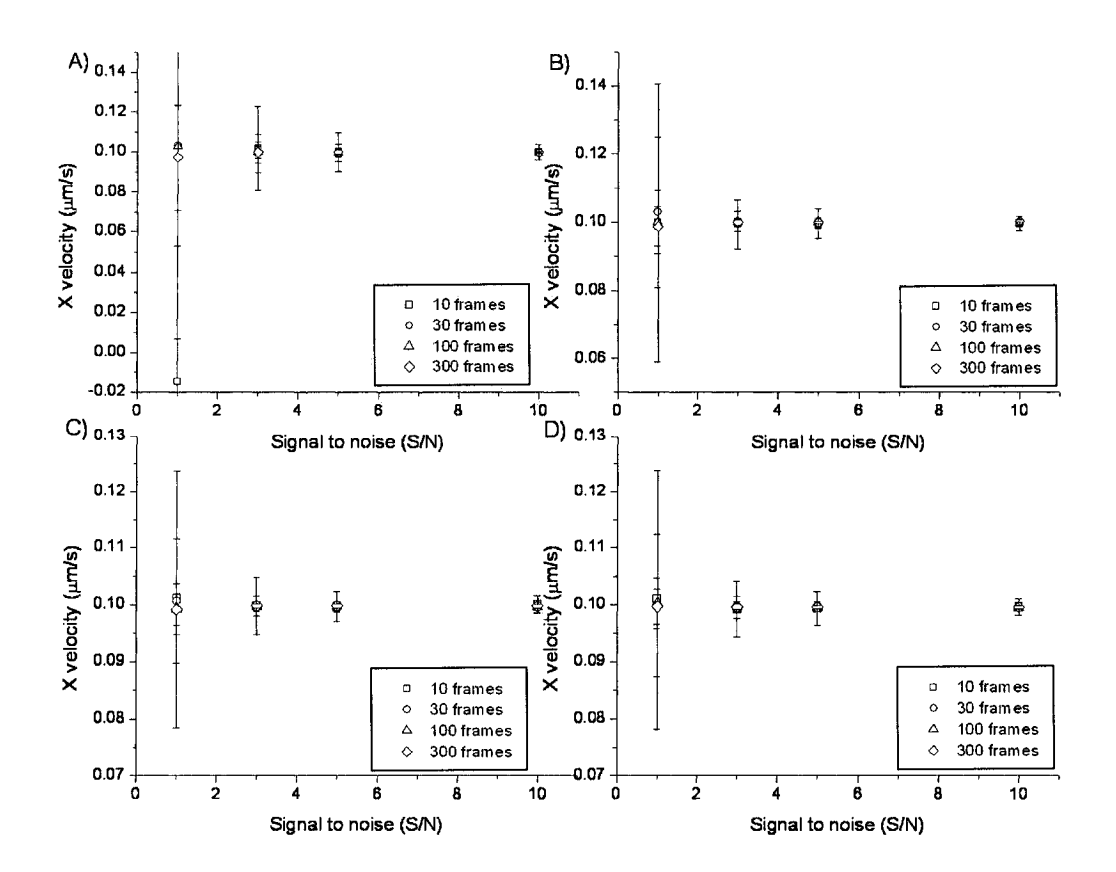


Figure 4.4: Simulation characterization of STICS accuracy and precision as a function of signal to noise ratio, with a set velocity of 0.1  $\mu$ m/s. A) density=0.01 particles per beam area, B) density=0.1 particles per beam area, C) density=1 particles per beam area, D) density=10 particles per beam area.

box size of  $16 \times 16$  pixels<sup>2</sup> and for typical spatial and temporal resolutions of 0.2  $\mu$ m/pixel and 5 s/frame respectively, the maximum velocity that can be measured by STICS is approximately 0.3  $\mu$ m/s, which is well above typical retrograde flow rates ( $\sim 0.01 \ \mu$ m/s) for actin and adhesion related proteins [1, 67].

The performance of the STICS analysis was also studied under varying conditions of signal to noise ratio, number of frames sampled and the density

82

of particles. For each set of conditions, 100 computer simulations were run to obtain an average value of the velocity in x and y and an error (the standard deviation, SD). The simulated images were  $128 \times 128$  pixels, with a spatial resolution of 1  $\mu$ m/pixel and a temporal resolution of 1 frame/s. The velocity was set at 0.1  $\mu$ m/s, typical of what would be obtained in a retrograde protein transport measurement in adherent cells. The signal to noise ratio, as defined in Eq. 3.2, was varied from 1 to 10. The density was varied between 0.01 to 10 particles per laser beam area (BA), and the number of image frames was varied between 10 and 300. This series of simulations allowed a full probing of the parameter space relevant to observation of flow in live cells.

The effects of signal to noise ratio (S/N) on the simulated images are depicted in Figure 4.3 with typical simulation parameters as defined above. The particle positions were kept fixed between the different images and the signal to noise ranges from 1 to 10, with 1 being an absolute worst case scenario where the standard deviation of the noise is as large as the amplitude of the signal. Analysis of these simulations revealed that STICS is able to perform very well (see Figure 4.4) even in poor conditions where the signal to noise ratio is as low as 1, provided that the number of frames is sufficiently large to allow sufficient averaging in Eq. 2.16.

The results of these simulations are summarized in Table 4.1. Notice that the STICS analysis works very well in almost all cases, with the only exception being the worst case scenario at the lowest density ( $\rho$ =0.01 particles/BA), the smallest number of frames (N=10) and the lowest signal to noise ratio (S/N=1.0). In all other cases the recovered x-velocity is accurate

$\rho$ S/N	1	3	5	10	S/N N
0.01	$0.000\pm1.000$	$0.100\pm0.020$	$0.100 \pm 0.010$	$0.100 \pm 0.004$	10
	$0.100\pm0.100$	$0.100 \pm 0.010$	$0.099 \pm 0.004$	$0.099 \pm 0.001$	30
	$0.100 \pm 0.050$	$0.100 \pm 0.005$	$0.100 \pm 0.002$	$0.100 \pm 0.001$	100
	$0.097 \pm 0.030$	$0.100 \pm 0.003$	$0.100 \pm 0.001$	$0.100 \pm 0.001$	300
0.1	$0.100 \pm 0.040$	$0.099 \pm 0.007$	$0.099 \pm 0.004$	$0.099 \pm 0.002$	10
	$0.100\pm0.020$	$0.100\pm0.003$	$0.100 \pm 0.002$	$0.100 \pm 0.001$	30
	$0.100\pm0.010$	$0.100 \pm 0.001$	$0.100 \pm 0.001$	$0.100 \pm 0.001$	100
	$0.099 \pm 0.006$	$0.100 \pm 0.001$	$0.100 \pm 0.001$	$0.100 \pm 0.001$	300
1.0	$0.100 \pm 0.020$	$0.100 \pm 0.005$	$0.100 \pm 0.003$	$0.100 \pm 0.002$	10
	$0.100\pm0.010$	$0.100 \pm 0.002$	$0.100 \pm 0.001$	$0.100 \pm 0.001$	30
	$0.100 \pm 0.005$	$0.100 \pm 0.001$	$0.100 \pm 0.001$	$0.100 \pm 0.001$	100
	$0.099 \pm 0.003$	$0.100 \pm 0.001$	$0.100 \pm 0.001$	$0.100 \pm 0.001$	300
10.0	$0.100 \pm 0.020$	$0.099 \pm 0.005$	$0.099 \pm 0.003$	$0.100 \pm 0.002$	10
	$0.100 \pm 0.010$	$0.100\pm0.002$	$0.100 \pm 0.001$	$0.100 \pm 0.001$	30
	$0.100 \pm 0.004$	$0.100 \pm 0.001$	$0.100 \pm 0.001$	$0.100 \pm 0.001$	100
	$0.100 \pm 0.003$	$0.100 \pm 0.001$	$0.100 \pm 0.001$	$0.100 \pm 0.001$	300

Table 4.1: STICS simulation analysis results for the measured x-velocity (set value  $v_x = 0.1 \ \mu m/s$ ) for the image series with varying particle density ( $\rho$  particles/BA), signal to noise (S/N) and number of image frames (N). Each number in the table represents the average velocity measured by STICS for 100 simulations under the set conditions and the quoted error is the standard deviation (SD).

to within a few percent of the set value. The error, or spread in the results between different simulations, diminishes as expected as the density  $\rho$  gets higher, as the number of frames N increases and as the signal to noise ratio (S/N) increases.

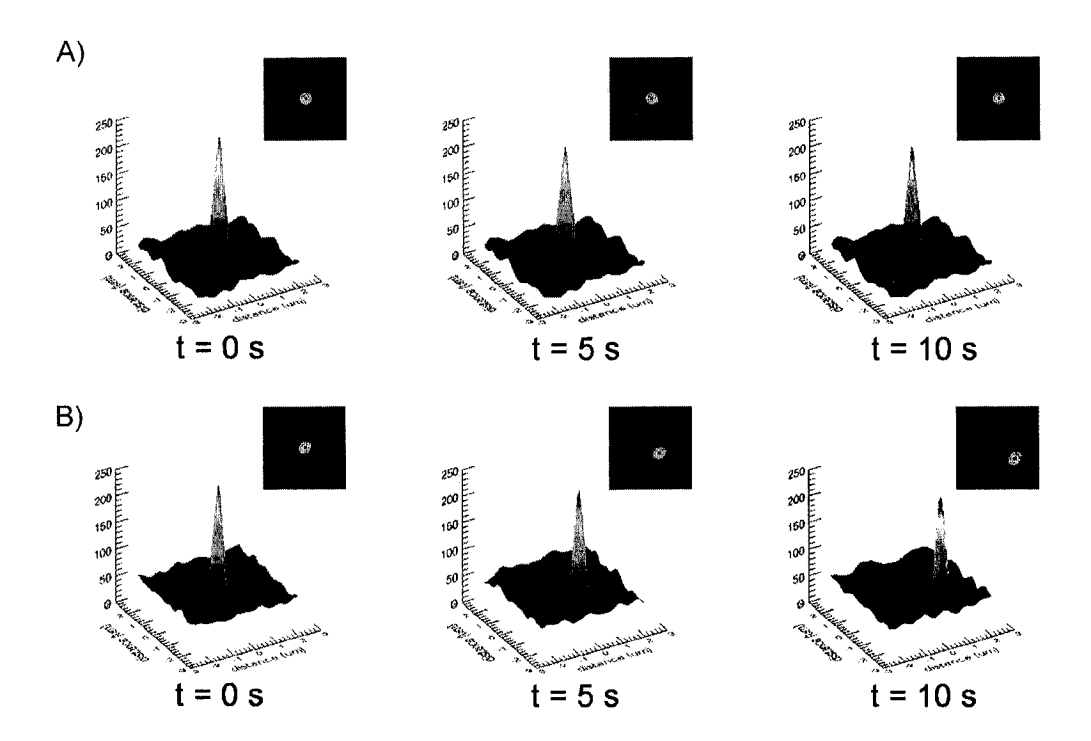


Figure 4.5: STICS analysis of a computer simulated images of flowing and immobile point emitters ( $v_x = -0.12$  and  $v_y = 0.08 \ \mu m/s$ , 90% immobile). A) spatio-temporal correlation functions as a function of time without immobile population filtering, notice the peak stays centered at ( $\xi$ =0,  $\eta$ =0) B) spatio-temporal correlation functions as a function of time with immobile filtering, now the Gaussian peak moves in a direction opposite to the flow and is not hidden by the immobile component (recovered velocities:  $v_x = -0.119 \pm 0.001 \ \mu m/s$  and  $v_y = 0.08 \pm 0.01 \ \mu m/s$ ).

# 4.3 Immobile Filtering Characterization

A very basic example of application of the immobile populations filtering algorithm (see section 2.7) is shown in Figure 4.5. A computer simulation of

point particles imaged by LSM with 90% of the particles immobile and 10% flowing ( $v_x = -0.12~\mu\mathrm{m/s}$  and  $v_y = 0.08~\mu\mathrm{m/s}$ ) was analyzed with STICS with and without filtering. As can be seen from Figure 4.5A the analysis without filtering is dominated by the stationary correlation peak at zero spatial lags due to the immobile population. The linear fits for  $x(\Delta t)$  and  ${m y}(\Delta t)$  (see Eq. 2.17) in this case yield velocity values of  $v_x=-0.01\pm0.01$  $\mu \text{m/s}$  and  $v_y = 0.01 \pm 0.01 \ \mu \text{m/s}$ , which are well below the set values and reflect the large static weighting of the immobile particle population. As a comparison, filtering the immobile population in the simulated image series before STICS analysis gave the measured velocity values of  $v_x = -0.119 \pm$  $0.001~\mu\mathrm{m/s}$  and  $v_y = 0.08 \pm 0.01~\mu\mathrm{m/s}$ . In Figure 4.5B we can see these results for the STICS analysis after filtering the immobile population: the correlation peak now moves away from  $(\xi=0, \eta=0)$  as only correlations due to the dynamic population are captured. The results of these simulations suggest that STICS, in combination with the immobile population filtering, can be used to measure protein transport for membrane associated proteins where a significant fraction of the proteins may be immobilized.

#### 4.3.1 Immobile Population Filtering Artifacts

As shown by the simulation results, removing the DC offset from a single pixel intensity trace can remove the effects of the immobile fraction if it is present over the entire time course of the measurement. Before applying this technique however, one has to be careful that certain criteria are fulfilled. There are a few important requirements, especially concerning sampling and the relative timescales of the underlying processes that must be taken into

account in such applications.

The filtering algorithm works because the characteristic time scale for flow (in terms of frames) is short enough compared to the total number of frames. In other words there is complete relaxation of the flow process over the time scale of the simulation (this requirement also holds for the case of a diffusion study with ICS, where one needs to have a complete relaxation of the diffusive process for accurate measurements). Relaxation refers to the complete decay of spatial fluctuations which occurs over the characteristic time for particle dynamics. If the flow is too slow compared to the total time of the experiment, then it will resemble an immobile population and be removed by the filtering algorithm. This situation can be avoided by selecting the right sampling time resolution and experimental time scale with which to measure the flow process. If no order of magnitude data is available, then several trial experiments should be run in order to assess the magnitude of the flow. The basic reasoning is that the particles should flow over a distance greater than one full laser focus diameter during the time course of the image series' sampling in order to have quasi-complete relaxation of the correlation function. Specifically the total time of the image series sampling, T, should be greater than the characteristic flow time (ratio of the laser beam radius to the velocity):

$$T >> \frac{\omega_{0ab}}{v_f} \tag{4.3}$$

If the particles do not move more than a correlation radius over the time of acquisition of the entire image series, then removing the DC offset will spatially anti-correlate the intensities over a short distance in the direction of the flow. In this case, the central Gaussian peak is reduced in width, and accompanied by two diametrically opposed depressions aligned with the flow direction (see Figure 4.6B). Nevertheless, these artifacts are of no real consequence in the determination of the flow direction because a Gaussian can still effectively be fit to the correlation functions and the fitted velocities are always within 1% of the set values in the simulations (see Figure 4.6A). Figure 4.6B shows the effect of immobile filtering on  $r'_{ab}(\xi, \eta, s)$  for varying velocities. The Gaussian peak narrows at low velocities due to the spatial anti-correlation with two depression on each side of the Gaussian peak, in the direction of the flow (which was the x direction in this case). Note that this effect is negligible when  $v\approx 0.1~\mu\text{m/s}$  which corresponds to the particles moving 10 correlation radii over the total image series time for this simulation. Thus in practice the condition in Eq. 4.3 now becomes:

$$T \approx 10 \times \frac{\omega_{0ab}}{v_f} \tag{4.4}$$

However, this condition needs only to be satisfied if we wish to recover the proper correlation radius from the STICS analysis after using the immobile filtering algorithm. Application of this algorithm is of particular importance when the image time series analyzed presents static bright, spatially extended fluorescent features (see for example filamentous adhesion structures in Figure 5.6C) that will contribute strong deviations at non-zero spatial lags and hence distort the gaussian shape in the spatial autocorrelation function. In this case, the fit to  $\omega_{0ab}$  in Eq. 2.8 will diverge significantly from the actual correlation radius value. Using the immobile filtering algorithm, one can remove these features and get a correct value for  $\omega_{0ab}$  provided that the

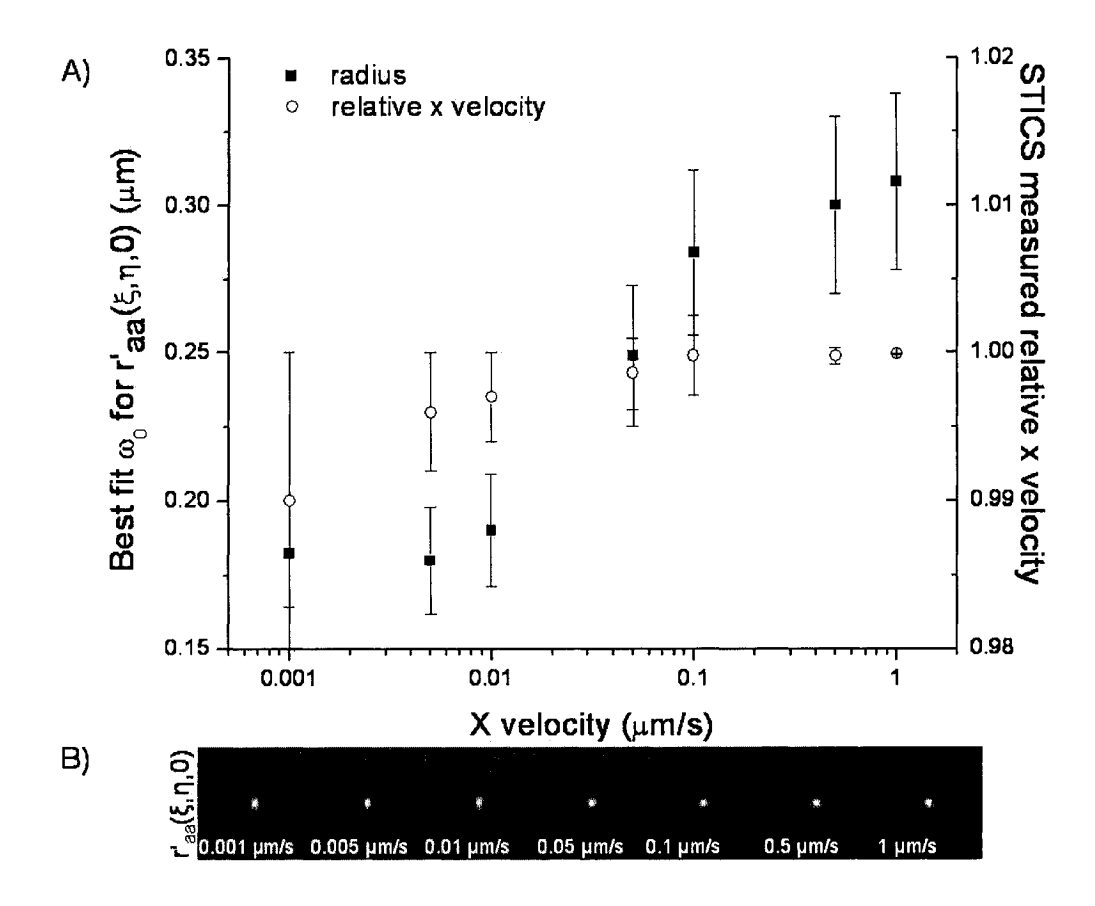


Figure 4.6: Simulation results for the effects of the immobile population filtering algorithm on  $r'_{ab}(\xi,\eta,s)$  for particle flow with varying velocities. All simulations were  $128 \times 128 \times 300$  (x,y,t) at 0.1  $\mu$ m/pixel and 0.1 s/frames. A) Plot of the fitted radius for  $r'_{ab}(\xi,\eta,0)$  and the recovered relative x velocity:  $v_{x(STICS)}/v_{x(input)}$  as a function of the set particle flow velocity magnitude. B) Two dimensional intensity contour maps of  $r'_{ab}(\xi,\eta,0)$  as a function of set particle flow velocity.

complete relaxation condition of Eq. 4.4 is satisfied.

In addition to the question of the time scale of the sampling, there is also the question of the relative time scales of the underlying dynamic processes. When imaging adhesion proteins in living cells, we are most likely going to encounter a combination case of immobile, diffusing and flowing

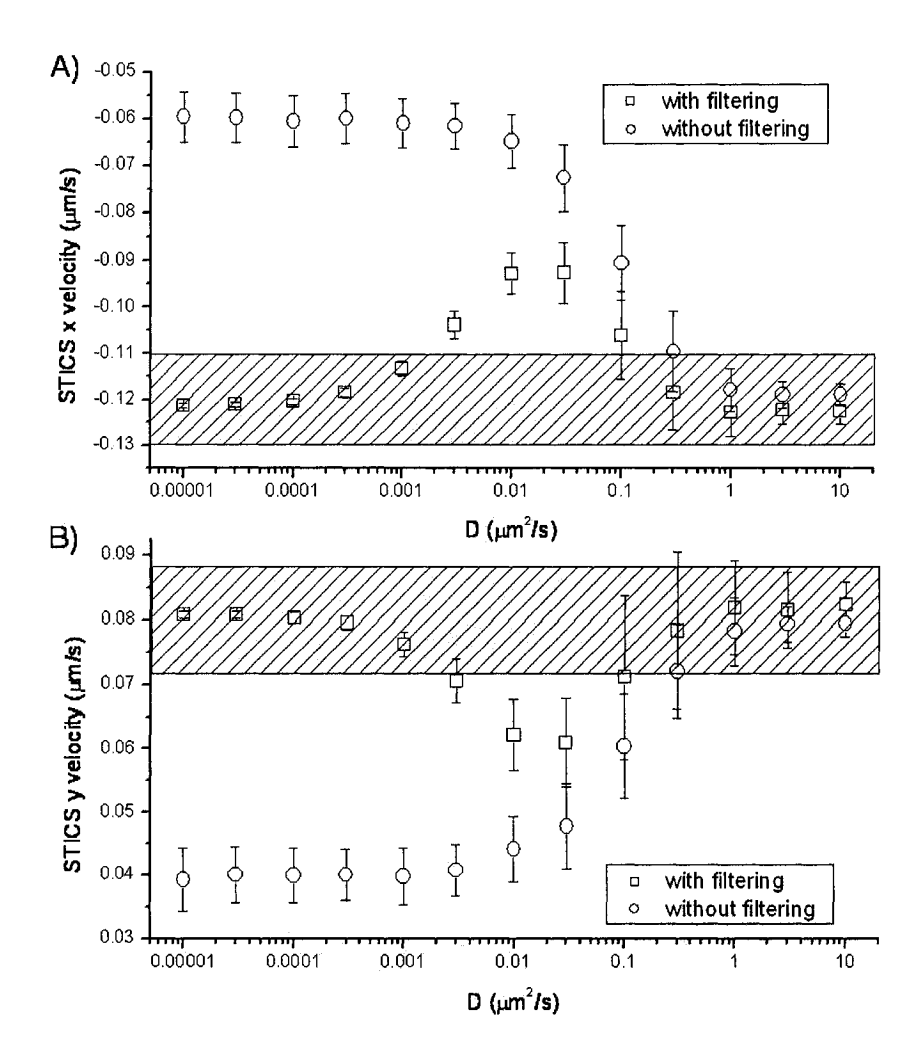


Figure 4.7: STICS analysis results for computer simulations with two particle populations, one flowing ( $v_x = -0.12 \ \mu m/s$  and  $v_y = 0.08 \ \mu m/s$ ) and one diffusing (variable diffusion coefficients). A) x velocity as measured by STICS with and without the immobile population filtering. B) y velocity as measured by STICS with and without the immobile population filtering. On both graphs, each point and error bar represent the average result of 100 simulations with standard deviation. The shaded regions show the set velocities in the simulation within an acceptable error band of  $\pm 10\%$ .

macromolecules. The filtering is able to remove the contribution of the immobile population as we have just shown, but the diffusing population has a

characteristic time scale that is important to consider. There are two limiting cases to envisage. First, if the diffusing population's characteristic time is fast compared to the characteristic time of the flowing population, then the diffusing Gaussian correlation peak (DG in Figure 2.9) is going to decay quickly within a few lag times. Then tracking the flowing Gaussian correlation peak (FG in Figure 2.9) can easily be done once the diffusion correlations have decayed. The other limiting case is if the diffusing population is slow compared the flowing population (in terms of their characteristic times). In this case, the total imaging time needed to capture the flowing population correlations will be short enough so that the diffusing population will not move significantly within that time window. Thus it will essentially look like an immobile population over this time scale and will be removed by the immobile filtering algorithm.

In order to quantify what is meant by "fast" and "slow" relative characteristic times, flowing and diffusing particle population computer simulations were run in which the characteristic flow time was kept constant (2.78 s), and the characteristic diffusion time was varied over several orders of magnitude from 4 ms to 4000 s. The computer simulated image series were 128 by 128 pixels with 100 frames at a density of 100 particles/ $\mu m^2$ , using 0.1 s/frame, 0.06  $\mu$ m/pixel and an  $e^{-2}$  radius of 0.4  $\mu$ m.

These simulations showed that the STICS analysis is valid when the characteristic diffusion time is about five times faster or slower than the characteristic flow time (see Fig. 4.7). When the characteristic times are similar,

the post filtering remnants of the diffusing population contribution (DG in Figure 2.9) effectively weight the flowing Gaussian correlation peak (FG in Figure 2.9) back towards the zero lags origin when we try to fit the position of the Gaussian peak in Eq. 2.17. However, both the x and y velocities are affected in a proportional manner by the radially symmetric diffusion correlation peak centered at the origin, so the direction of particle flow can still be correctly determined from the underestimated values of  $v_x$  and  $v_y$ . In the simulations shown, the angle of the velocity vector of the particles relative to the x-axis was set to be 146.3° and the average recovered angle for the 4 data points (with filtering) that lay outside the shaded acceptable range  $(\pm 10\% \text{ region})$  in Figure 4.7 was  $146.2 \pm 0.4^{\circ}$ . In such scenarios, if one can assume that the total flow is dominated by the directional flux (as opposed to separate flows in random directions), then one can scale the x and y velocities from STICS analysis according to the total velocity obtained by ICS analysis. Note that the temporal ICS analysis will be sensitive to all flow processes present, which will all contribute to the decay of the correlation function. For the case of the adhesion protein transport at the membrane in cells that we report in this work, the second scenario of faster diffusion  $(\tau_D \gg \tau_f)$  was usually observed.

#### 4.3.2 Dynamic Range of Immobile Filtering

The performance of the STICS analysis in the presence of an immobile population was verified under varying conditions of signal to noise, number of frames sampled and the fraction of the population that is immobile (the total particle density being kept constant). For each set of conditions, 100 computer simulations were run to obtain an average value and an uncertainty

(SD). As before, the simulations were  $128 \times 128$  pixels, with a spatial resolution of 1  $\mu$ m/pixel and a temporal resolution of 1 frame/s. The flow velocity was set at 0.1  $\mu$ m/s, typical of what would be obtained in a retrograde protein transport cellular experiment. The density was kept constant at  $\rho$ =10 particles/BA, while the signal to noise ratio, as defined in Eq. 3.2, was varied from 1 to 10, and the number of frames was varied between 10 and 120. This series of simulations explored the overall accuracy and precision of the STICS technique in the presence of a variable fraction of immobile species (0 to 90% immobile).

The results of these simulations are shown in Table 4.2. There are a few things to note in this table. The first is that when provided with a sufficient number of frames (here N=120), the STICS analysis can always recover the input velocity, within these ranges of signal to noise ratio or immobile population fraction. The only exception to this was the worst case scenario, when S/N=1 and the immobile fraction was 90%, where the error is slightly larger but still encompasses the input value. Another element to point out is that for S/N above 1, the fraction of immobile population does not change the results dramatically, suggesting that the number of frames is a much more important factor for accurate STICS analysis. Finally the results also show that STICS needs more than 30 frames in the image series (at v=0.1  $\mu$ m/s) in order for the subtracted average in each pixel to make sense. This can be rephrased in more general terms. Since particles move 3 pixels in 30 frames and the laser focal spot radius was set at 4 pixels in these simulations, it seems that we need our particle to move at least one full beam focus diameter during the time of the experiment. This is

imm	1	3	5	10	S/N N
0%	$-0.17 \pm 0.84$	$-0.10 \pm 0.64$	$-0.01 \pm 0.46$	$0.02 \pm 0.34$	10
	$-0.02 \pm 0.59$	$0.155 \pm 0.006$	$0.155 \pm 0.004$	$0.155 \pm 0.002$	30
	$0.106 \pm 0.003$	$0.106 \pm 0.001$	$0.106 \pm 0.001$	$0.106 \pm 0.001$	70
	$0.101 \pm 0.002$	$0.101 \pm 0.001$	$0.101 \pm 0.001$	$0.101 \pm 0.001$	120
30%	$0.04 \pm 0.77$	$-0.06 \pm 0.69$	$-0.03\pm0.55$	$-0.01 \pm 0.39$	10
	$-0.10\pm0.73$	$0.154 \pm 0.009$	$0.155 \pm 0.004$	$0.155 \pm 0.003$	30
	$0.106 \pm 0.004$	$0.106 \pm\ 0.001$	$0.106 \pm 0.001$	$0.106 \pm 0.001$	70
	$0.101 \pm 0.002$	$0.101 \pm\ 0.001$	$0.101 \pm 0.001$	$0.101 \pm 0.001$	120
60%	$-0.09\pm0.73$	$-0.09 \pm 0.70$	$-0.05\pm0.62$	$0.01 \pm 0.44$	10
	$0.04 \pm 0.66$	$0.13 \pm 0.14$	$0.155 \pm 0.004$	$0.155 \pm 0.002$	30
	$0.10 \pm 0.04$	$0.106 \pm 0.001$	$0.106 \pm 0.001$	$0.106 \pm 0.001$	70
	$0.101 \pm 0.003$	$0.101 \pm\ 0.001$	$0.101 \pm 0.001$	$0.101 \pm 0.001$	120
90%	$-0.07\pm0.69$	$0.00 \pm 0.65$	$-0.18 \pm 0.71$	$-0.12 \pm 0.66$	10
	$-0.05 \pm 0.69$	$-0.05 \pm 0.63$	$0.16 \pm 0.24$	$0.155 \pm 0.004$	30
	$0.00 \pm 0.65$	$0.107 \pm 0.003$	$0.106 \pm 0.002$	$0.106 \pm 0.001$	70
	$0.09 \pm 0.15$	$0.100 \pm 0.002$	$0.101 \pm 0.001$	$0.101 \pm 0.001$	120

Table 4.2: STICS simulation analysis results for the measured x-velocity (set value  $v_x = 0.1 \ \mu m/s$ ) for the characterization simulations with immobile fraction (imm), signal to noise ratio (S/N) and number of image frames (N). Each number in the table represents the average velocity measured by STICS from 100 simulations under the set conditions and the quoted uncertainty is the standard deviation (SD). All simulations were corrected for immobile population.

closely tied to Eq. 4.3, which was set as the condition at which we could recover the correct beam radius from the STICS analysis after performing the immobile population removal on the time series. This also explains the consistent overestimation of the velocity. Since we artificially introduce a negative correlation at the origin, in the presence of noise the fit peak is located farther from the origin than it really should be, thus giving a higher velocity value. However, the results of Table 4.2 show that when provided with a sufficient number of frames, we can expect this overestimation to be under 5%.

## 4.3.3 Window Filtering Correction for ICS

The previous section dealt with removing the immobile fraction by filtering out the zero frequency component (DC offset) in the intensity pixel traces of the image time series. However, this only works for a truly immobile population, and we have seen some deviation when we add a slowly diffusing population (that is almost immobile on the time scale of the measurement). Window filtering removes a local average around a point, so that intensity fluctuations due to slow processes, which are essentially static over that time window, will not contribute to the correlation function. Some cases where removing a slowly varying signal might be of interest include the situation of a large vesicle moving slowly through the field of view, the protruding edge of a cell advancing at a slower rate than the dynamic transport of molecular species inside the cell, or more simply laser illumination fluctuations or focus drift. However, one has to be careful that the window size chosen for the average calculation is large enough to allow quasi-complete relaxation of the dynamic processes of interest, otherwise the deviations outlined in section

#### 4.3.1 will become significant.

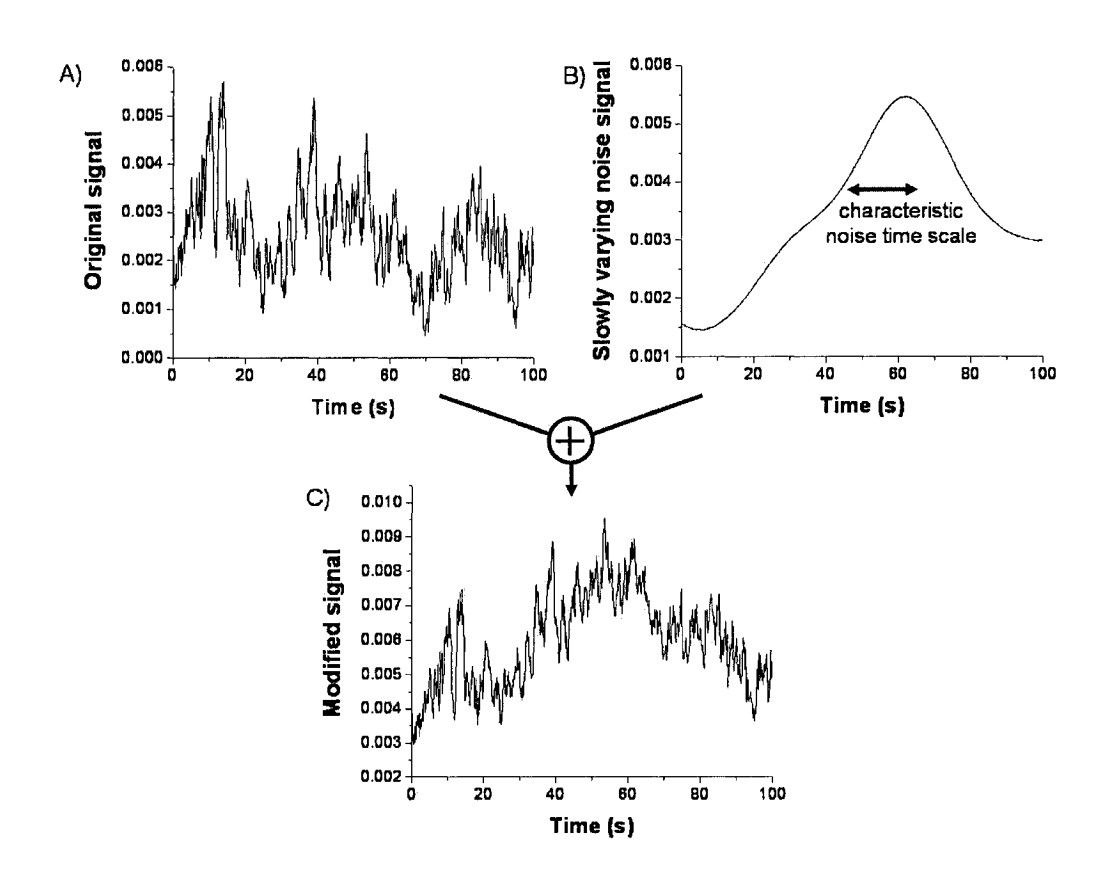


Figure 4.8: Generation of single (x,y) point intensity trace with slowly varying noise. The original intensity trace (A) is added to a slowly varying noise signal (B) which has a characteristic time scale of fluctuation, to give the modified signal (C).

Computer simulations were run to test the applicability of the theory presented in section 2.7.2. We extracted a 30,000 point intensity trace from a single (x,y) point in a simulated image time series where the particle diffusion coefficient was set to be 0.01  $\mu m^2/s$ , the time resolution was 0.1 s/frame and the  $e^{-2}$  Gaussian radius was 0.3  $\mu m$ . This data constituted what we call the "original signal" (see Figure 4.8A) to which a slower time scale, smoothly varying noise signal (see Figure 4.8B) was added to simulate a slow drift in

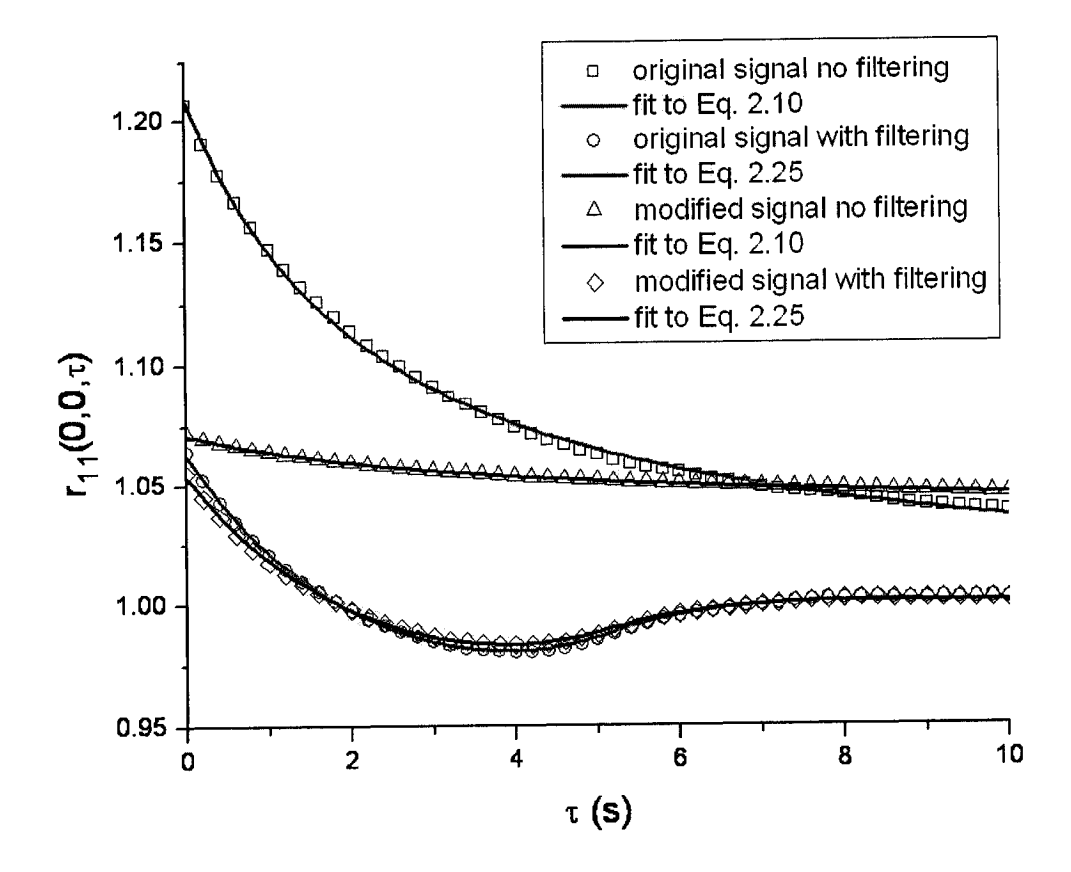


Figure 4.9: Temporal autocorrelation functions and best fits of the original single pixel intensity trace signal (30,000 frames) and modified signal (original + slowly varying noise with characteristic time scale of 20 s), for both filtered and unfiltered simulation data sets. The filter window size was set at 101 frames ( $\Delta N = 50$ ). The intensity data was extracted from an image time series simulation.

intensity to give what we refer to as the "modified signal" (see Figure 4.8C). The added noise signal was obtained by convolving in time a computer generated random noise signal with a Gaussian function. It was thus given a characteristic timescale which we define as the  $e^{-1}$  extent of the Gaussian function. The window average filtering was applied to both the original and modified signals, generating a set of two filtered signals. The autocorrela-

97

tions of all four signals were calculated and fit for using Eq. 2.25 with the appropriate window size.

Temporal autocorrelation functions of the original and modified signal, both unfiltered and filtered with a 101 frame ( $\Delta N=50$ ) window, are shown in Figure 4.9 for a characteristic slow noise signal timescale of 20 s. Notice that the correlation functions for the filtered signals reach values below 1. This is due to the fact that we are introducing negative correlations in the filtered data when using the window filtering. The autocorrelation function of the original signal was fit using Eq. 2.10 to obtain an estimate of  $D=0.010\pm0.001~\mu m^2/s$  (average of 100 simulations plus SD). Figure 4.9 also shows an autocorrelation function computed after filtering the original signal with the window averaging defined by Eq. 2.19 with a window size of 101 frames ( $\Delta N=50$ ). The theoretical curve in Eq. 2.25 (adapted for  $\Delta N=50$ ) was fit and a  $D=0.010\pm0.001~\mu m^2/s$  was calculated from the fit parameters. This shows that with the original signal (filtered or not), both fitting equations can recover the diffusion coefficient.

The same process was repeated with the modified (slow noise added) signal, and the autocorrelation functions for the unfiltered and filtered modified signal are shown in Figure 4.9. Note that in this specific case, the characteristic timescale of the added noise signal is 20 seconds, or 200 frames, which is longer than our window size for the filtering (101 frames). Thus we expect the window average removal to get rid of the slowly varying signal efficiently. For the unfiltered signal, the best fit recovered diffusion coefficient

was  $0.004 \pm 0.001 \ \mu m^2/s$ , whereas for the filtered signal, it was  $0.010 \pm 0.002 \ \mu m^2/s$ . This shows how the regular ICS fit model fails if there are significant variations in the intensity of the signal, i.e. the fluctuations arise from longer time scale intensity changes of the slowly varying noise signal in addition to the dynamics of the molecule of interest. Notice how the autocorrelation curves for both the filtered original signal and the filtered modified signal are almost identical. This shows that if the fluctuations are slow enough, then the window average filtering can eliminate them and the diffusion coefficient can be measured accurately using Eq. 2.25 as a fit model.

The results of a general analysis using window filtering for various added noise signal characteristic timescales are shown in Figure 4.10 and Table 4.3. As expected, ICS can recover the set simulation diffusion coefficient when fitting the unfiltered original signal temporal autocorrelation function to Eq. 2.10. We obtain an accurate diffusion coefficients with a slightly larger standard deviation when fitting the filtered original signal temporal autocorrelation function to Eq. 2.25. After adding noise of varying characteristic timescales to the original signal, we see that in most cases ICS fails to recover the set diffusion coefficient except when the time scale of the noise signal is very long relative to the diffusion timescale. This means that we are adding very slow fluctuations to our signal and we do not expect these to significantly influence the fitting of the correlation function using Eq. 2.10. After filtering combined signal and noise, and fitting to the modified decay (Eq. 2.25) of the temporal correlation function, it is clear that we can recover the set diffusion coefficient in almost all cases simulated. The only exception was the first case where the characteristic noise timescale is 5 seconds,

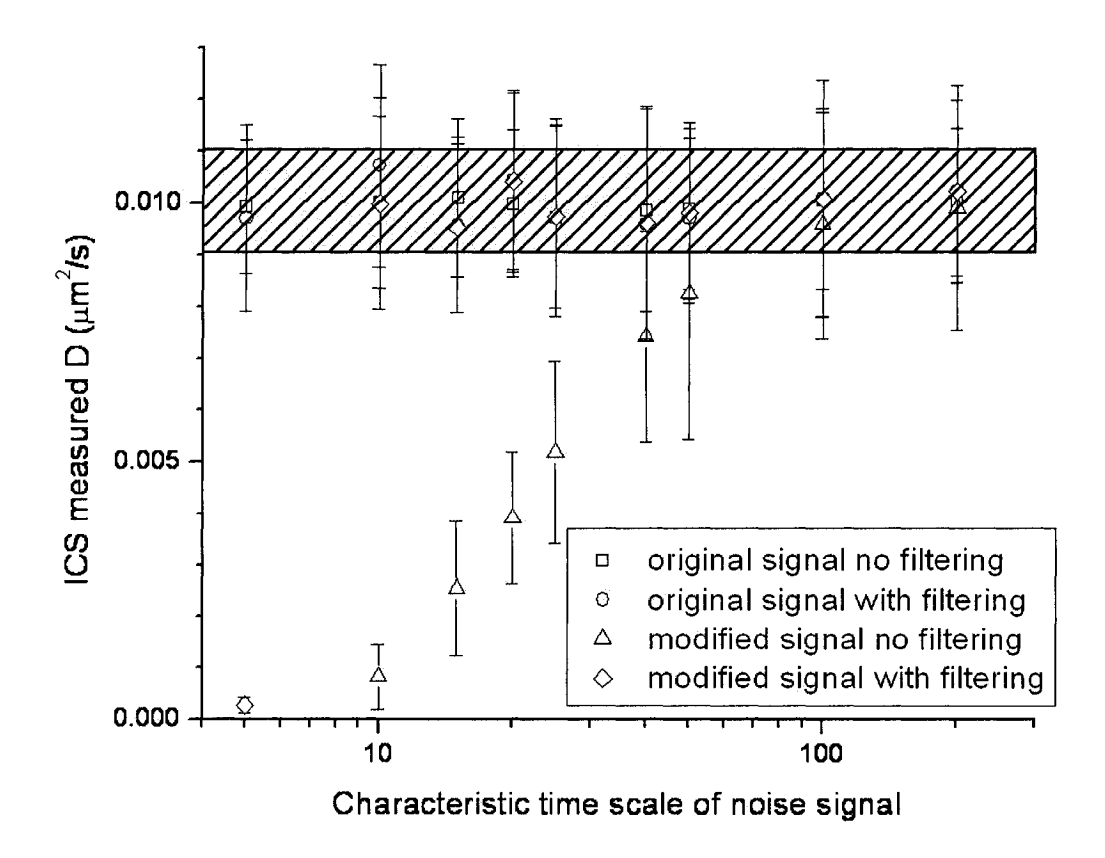


Figure 4.10: Diffusion coefficients recovered from temporal correlation analysis of simulated pixel intensity traces before and after windowed immobile population filtering, on both the original signal and the modified signal (original + slowly varying noise). Points and error bars on the graph represent the average of 100 simulations with standard error of the mean. All simulations were 30,000 frames, with the diffusion coefficient set at 0.01 μm²/s, the time resolution at 0.1 s/frame and the Gaussian e<sup>-2</sup> radius at 0.3 μm. The shaded band shows the set diffusion coefficient with an acceptable error of ±10%.

or 50 frames, which is half of our window size. In this case, we expect to see significant intensity variations due to the noise signal within our window frame, which is going to affect the correlation function of the filtered signal. However, even when the characteristic timescale of the noise signal is 100

characteristic		D original	D original	D modified	D modified
noise timescale		unfiltered	filtered	unfiltered	filtered
(s)	(frames)	$(\mu m^2/s)$	$(\mu m^2/s)$	$(\mu m^2/s)$	$(\mu m^2/s)$
5	50	$0.010\pm0.001$	$0.010\pm0.002$	$0.130 \pm 0.030$	$0.000 \pm 0.001$
10	100	$0.010 \pm 0.002$	$0.010 \pm 0.002$	$0.001 \pm 0.001$	$0.010 \pm 0.002$
15	150	$0.010 \pm 0.002$	$0.010 \pm 0.002$	$0.003 \pm 0.001$	$0.010 \pm 0.002$
20	200	$0.010\pm0.001$	$0.010 \pm 0.002$	$0.004 \pm 0.001$	$0.010 \pm 0.002$
25	250	$0.010\pm0.002$	$0.010 \pm 0.002$	$0.005 \pm 0.002$	$0.010 \pm 0.002$
40	400	$0.010\pm0.002$	$0.010 \pm 0.002$	$0.007 \pm 0.002$	$0.010 \pm 0.002$
50	500	$0.010\pm0.002$	$0.010\pm0.002$	$0.008 \pm 0.003$	$0.010 \pm 0.002$
100	1000	$0.010\pm0.002$	$0.010 \pm 0.002$	$0.010\pm0.002$	$0.010\pm0.002$
200	2000	$0.010\pm0.001$	$0.010 \pm 0.002$	$0.010\pm0.002$	$0.010\pm0.002$

Table 4.3: Diffusion coefficients recovered from ICS analysis of simulation time series before and after windowed immobile population filtering ( $\Delta N = 50$ ), on both the original signal and the modified signal (original signal+ slowly varying noise). All simulations were 30,000 frames, and every number in the table represents the average ICS measured D for 100 simulations with standard error of the mean. The diffusion coefficient was set at 0.01  $\mu$ m<sup>2</sup>/s, the time resolution was 0.1 s/frame and the Gaussian e<sup>-2</sup> convolution radius was 0.3  $\mu$ m.

frames (so almost equal to our window size of 101 frames), the filter adjusted correlation analysis can recover the set diffusion coefficient within error.

#### 4.3.4 Window Filtering and STICS

Window filtering of a slowly moving population can also be of use when using the STICS technique for mapping velocities. To asses the effects of this type of filtering on the STICS analysis, we generated simulated images of  $128 \times 128$  pixels, with a spatial resolution of  $0.1 \ \mu m/pixel$  and a temporal resolution of  $0.1 \ frame/s$ . The particle velocity was varied between  $0.01 \ and \ 1.0 \ \mu m/s$ , and the window filter size was changed from 21 to 111. The measured STICS velocities are shown in Figure 4.11 as a function of set input velocity, where

each point represents the average from 100 simulations, and the error is the standard deviation (SD).

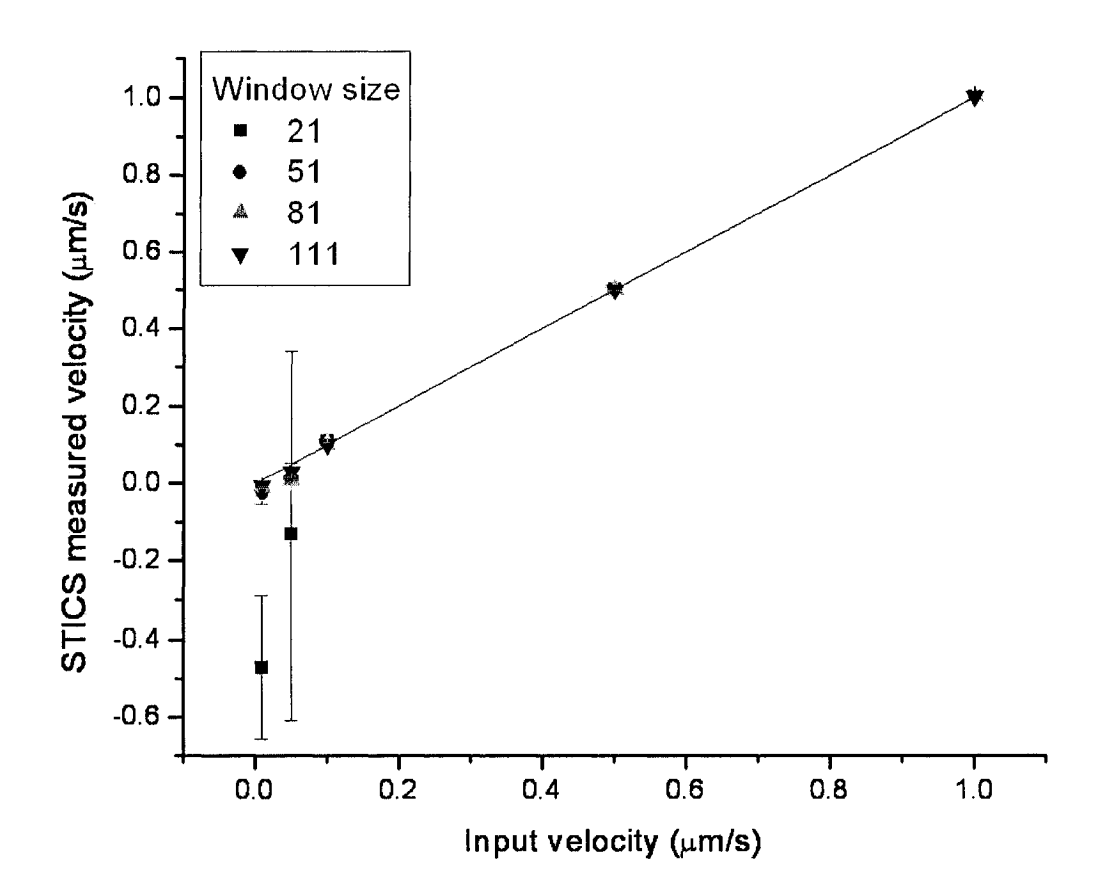


Figure 4.11: Plot of STICS measured mean velocity as a function of set input particle velocity after window immobile population removal for image series simulations. Each error bar is the standard deviation for 100 simulation measurements.

These simulations show that the STICS velocity measurement fails for small window sizes, but this is not due to an intrinsic flaw in the STICS method. It fails because the window size is too small and the underlying dynamic processes (here flow) do not relax completely over the time scale of

$v$ $\Delta N$	21	51	81	111
0.01	$-0.47\pm0.18$	$-0.02\pm0.03$	$-0.010\pm0.003$	$-0.007\pm0.003$
0.05	$-0.13\pm0.47$	$0.013 \pm 0.008$	$0.007 \pm 0.009$	$0.03\pm0.02$
0.1	$0.109 \pm 0.001$	$0.105 \pm 0.008$	$0.102 \pm 0.002$	$0.1001 \pm 0.0003$
0.5	$0.5001 \pm 0.0003$	$0.5001 \pm 0.0002$	$0.5000 \pm 0.0008$	$0.5002 \pm 0.0003$
1.0	$0.9997 \pm 0.0008$	$1.0000 \pm 0.0001$	$1.0000 \pm 0.0001$	$1.000 \pm 0.001$

Table 4.4: STICS measured mean velocity as a function of set input velocity and filter window size for image series simulations as a function of set velocity (v) and window size  $(\Delta N)$ . Each number in the table represents the average velocity measured by STICS from 100 simulations under the set conditions and the quoted uncertainty is the standard deviation (SD).

the window. Table 4.4 shows the simulations STICS analysis results, and we can see that the measurement systematically fails for  $v=0.01~\mu\text{m/s}$  because even in 111 frames (i.e. 11.1 seconds) the particles only move 0.111  $\mu m$  (just over one pixel). This does not satisfy the sampling criterion of Eq. 4.3 as discussed in sections 4.3.1 and 4.3.2. This condition will be met for  $v \geq 0.05~\mu\text{m/s}$  at a window size of 111. In the limiting case of  $v=0.05~\mu\text{m/s}$ , the particles move approximately 0.5  $\mu m$  over the time scale of the window when  $\Delta N$ =111 (which is greater than the Gaussian  $e^{-2}$  radius of 0.3  $\mu m$ ) and the STICS measured velocity of 0.03±0.02 is within error of the set value. In general, the STICS analysis works well with the window filtering when the dynamic process of flow relaxes completely over the time scale of the window.

Also, as discussed in the previous section, by removing a window average from the data, we are introducing negative correlations. This is reflected in the STICS analysis as the Gaussian flow peak becomes negative, i.e. a negative amplitude  $g_{ab}(0,0,s)$  in Eq. 2.17. However, this does not prevent

103

us from fitting for the x and y location of this peak, and thus we can still extract the correct velocity values.

## 4.4 Chapter Conclusion

In this chapter we modeled fluorescence microscopy imaging of protein dynamics in the membrane by using computer simulations of point emitter particles diffusing and flowing in a two dimensional matrix. We used the simulation image time series to investigate the dynamic range, accuracy and precision of STICS, under set simulation conditions of photobleaching rate, signal to noise ratio, immobile population removal by Fourier filtering, and different ratios between the characteristic diffusion and flow times for the particles. We found that STICS was almost unaffected by photobleaching or low signal to noise ratios, since it always recovered the set value for velocity within the ranges studied. Furthermore, we investigated the effects of immobile filtering and found that given proper spatio-temporal sampling, STICS can recover accurate particle velocities even in the presence of a high density immobile population. Finally, we showed that the window immobile filtering algorithm could be applied in cases where a slowly varying noise signal is superimposed over the signal of interest, and that both STICS and temporal correlation analysis could recover the set velocity values after the filtering. Overall, we have seen that STICS is a very robust technique by investigating its dynamic range using a range of simulation parameters. The next chapter will focus on the characterization and implementation of STICS in vivo.



## 5 In Situ Characterization

### 5.1 Introduction

The sheer complexity of microenvironments present in the cell stems from the diversity of the molecular components, their dynamics and an incredibly complex myriad of interactions between them. However refined computer simulations might be given the rapid progress that has been made in microprocessor speed and computational algorithms, they currently cannot mimic the full extent of a living cell. Therefore, a careful testing of any new biophysical technique has to be performed in situ, and care must be exercised in applying the method to account for cellular variability, inhomogeneous dynamical parameters, background and noise, and any other important physical parameter. In this section, I first present the controls and corrections that have to be applied to an image time series before performing the STICS analysis, in order to remove the background noise and correct for drift and intensity variations. I will then show control measurements performed on chemically fixed cells to test the detection limits of STICS, and present the measurement and analysis of typical cases of diffusion, non directed flow and directed flow of labeled proteins in living CHO cells. Finally, I will demonstrate a test experimental application of the cross-correlation implementation of STICS using fluorescent microsphere samples, and an in situ proof of principle experiment using two kinds of labeled tracers in fish epidermal keratocytes to characterize applications of the STICS and STICCS methods in real systems.

## 5.2 Image treatment

## 5.2.1 Noise and Immobile Population Removal

The white or random noise that, by definition, has a uniform power spectral density at every frequency in the range of interest, only contributes at the zero spatio-temporal lag point of the correlation function:  $r_{ab}(0,0,0)$ . This stems from the fact that white noise is essentially uncorrelated beyond zero lags, so it only correlates with itself. As discussed in the original ICS contributions [51, 97], it is possible to correct for white noise by acquiring a white noise image and measuring its average to subsequently remove this number from the original cell image. The same method can be applied by selecting an "off-cell" region from the image (see Figure 5.1), which should essentially be white noise assuming there are no real fluorescent particles in the region. The average intensity of that subregion is subsequently subtracted from the whole image to correct for the mean background. The result of this process is shown in figure 5.1, where the corrected image shows better contrast, and more importantly for quantitative analysis has a reduced background noise contribution.

In STICS analysis, however, the immobile population filtering algorithm will remove the white noise offset at every pixel by removing the average value of that pixel over the time course of the experiment. This temporal average should be equivalent to the spatial average if we assume that the system is ergodic, and that there are no significant laser intensity variations during the acquisition. The Fourier filtering algorithm is designed to remove the immobile component in the space time correlation function of Eq. 2.5. If

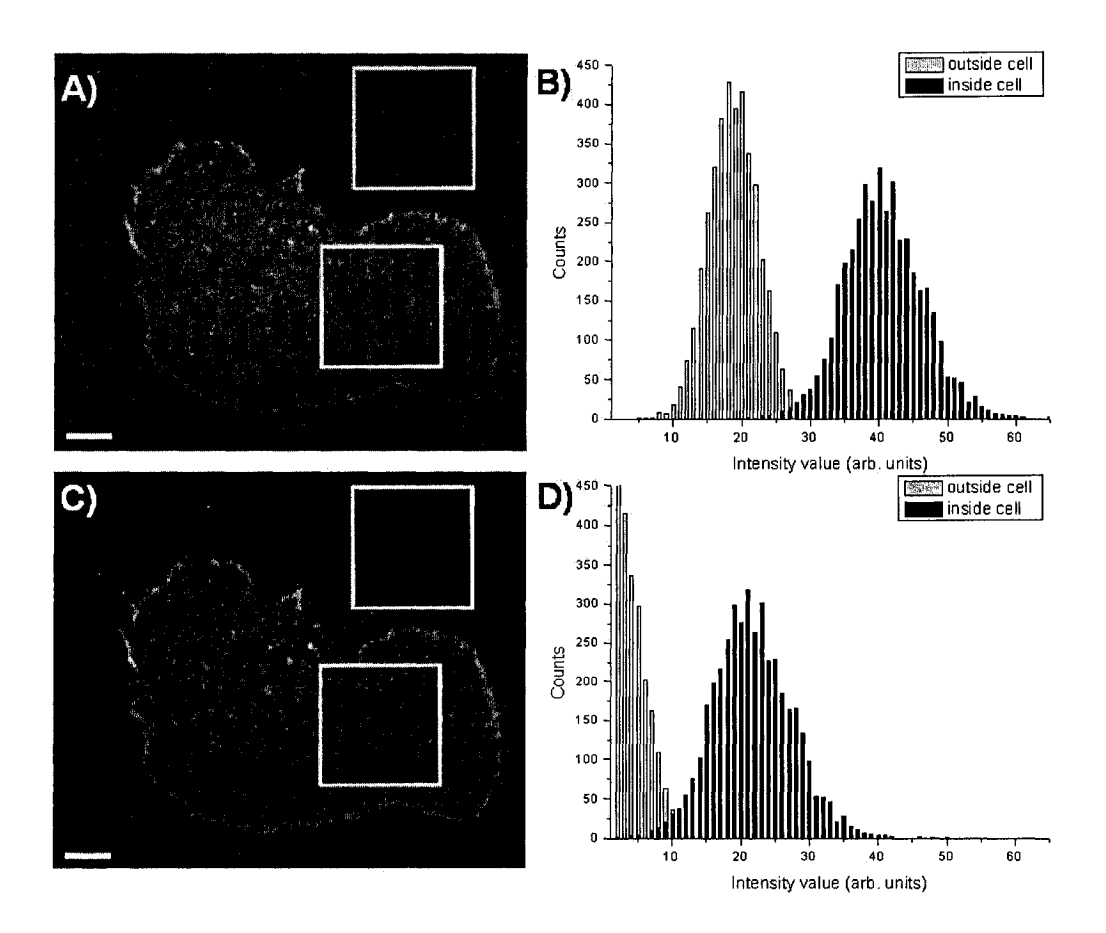


Figure 5.1: Example of white noise correction. A) TIRM image of a CHO cell transfected with actin-mRFP. B) Histograms of the intensity inside and outside of the cell, as defined by the two white boxes shown in A. C) Mean background corrected image of the cell showing better contrast than the original image. D) New histogram of intensities after average background correction from the same regions inside and outside the cell. Scale bars are 5 μm.

this immobile component is not removed, then the STICS measured velocity is consistently underestimated (see section 4.3.2).

Filtering the immobile population will also remove any extended spatial correlations due to static fluorescent structures in the image. These structures can severely deform the spatial correlation function if they are present.

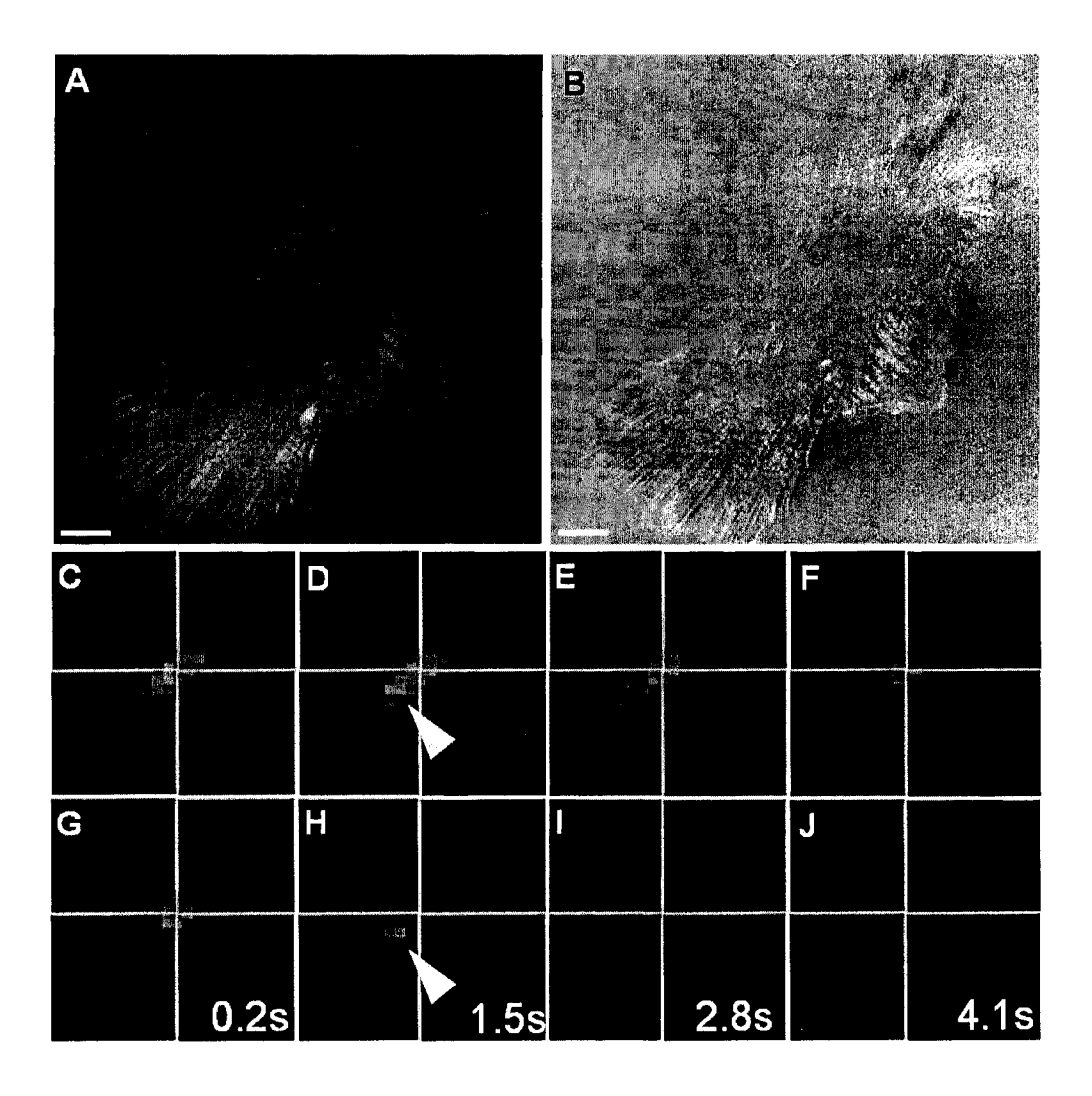


Figure 5.2: Example of immobile population filtering. A) TIRM image from a time series of a CHO cell transfected with α-actinin conjugated with GFP. B) Same image after immobile population removal using the whole time series. Scale bars are 10 μm. C-F) Time evolution of the spatio-temporal correlation function without immobile population removal. Note that the flow peak is buried in the static correlations of the immobile population. G-J) Time evolution of the spatio-temporal correlation function with the immobile population removed. The translating peak due to flow can now easily be seen and tracked.

For example, if the image contains an actin stress fiber (bundle of actin filaments) or focal adhesion contacts, the correlation function will be perturbed

and deviate from the expected Gaussian shape as these cellular structures are larger than the diffraction limit. Figure 5.2A-B shows a typical image of a cell transfected with GFP tagged  $\alpha$ -actinin and the resulting image following the immobile population filtering in the image series. Because  $\alpha$ -actinin strongly interacts with actin, it is also organized in filamentous structures (along the actin filaments) and thus the spatial correlation function of the first image reflects this organization by showing long "bands" of spatial correlations oriented in the direction of the filaments (see Figure 5.2C-F). Any fraction of the total population that undergoes directed motion along the filaments will be obscured by the static correlations of the mostly immobile proteins. The image after filtering shows less structure, and although the organization along filaments can still be seen, the filtered time series shows much clearer speckles of  $\alpha$ -actinin undergoing retrograde flow. Indeed, the spatial correlation function after the immobile population filtering does not show these long range spatial correlations, and we can clearly track the translating Gaussian peak due to flow and extract the  $\alpha$ -actinin velocity in and around the filaments (see Figure 5.2G-J, white arrow head).

#### 5.2.2 Drift Correction

An unavoidable consequence of imaging with any type of microscope is sample drift. The sample is mechanically coupled to the objective lens by the immersion oil (see section 2.3.1). So after focusing, the system can sometimes slowly relax to an equilibrium, leading to a slight lateral drift or a drift from focus axially of the sample on the microscope stage. Such a drift in the image series will hamper quantitative pixel-to-pixel analysis of any spatially dependent variable. The drifts can range from as small as one half to a

few micrometers, which corresponds to typical distances moved by proteins such as actin over the duration of a typical image series collection. Such a drift would show up as a significant component of protein flow in the STICS analysis, and it is essential to be able to detect and correct for drift when it appears.

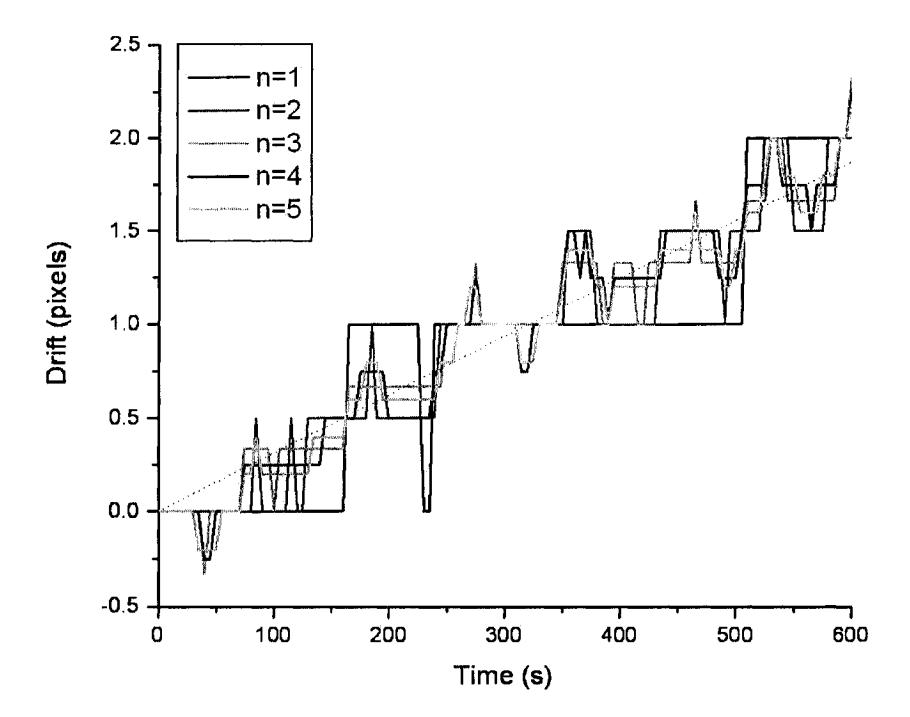


Figure 5.3: Measured stage drift as a function of time for an image time series of a CHO cell. As we increase the rebinning factor n, the precision in the drift measurement increases. The dotted line shows a linear best fit to the n=5 curve. This theoretical curve is used for final drift correction on the entire image time series.

A simple correlative approach was used to find the drift at any time point. It assumes that the cell doesn't change shape extensively, and requires locating a source of background fluorescence that is bound to the coverslip surface and can thus act as a reporter of stage drift. The correction scheme simply uses the first frame of the movie (or a cropped subregion around the marker) as a reference frame, and subsequently correlates every frame of the image series with the first one. The maximum of the correlation function  $(x_{max}, y_{max})$  is located for each frame by a simple maximum location search. This gives the x and y displacements (i.e. the drift) at which the images best match (correlate with) the first reference image with about a one pixel precision. One can fit a function (usually a Gaussian), to extract the peak location with subpixel precision, but the choice of that function would critically influence the peak location and is therefore not so reliable. An alternate approach, that was used in this work, involves artificially enhancing the resolution of the image by a factor of n by rebinning the pixels of the original  $N_x$  by  $N_y$  pixels image into a grid  $n \times N_x$  by  $n \times N_y$  using interpolation. The correlation function is now recalculated, and the pixel location where it attains its maximum value  $(x'_{max}, y'_{max})$  is related to the original pixel location  $(x_{max}, y_{max})$  and the rebinning factor n through:

$$(x_{max}, y_{max}) = (\frac{x'_{max}}{n}, \frac{y'_{max}}{n})$$
 (5.1)

thereby artificially enhancing our precision by a factor of n. By visual inspection of the drift-corrected image time series, we found that values of n greater than 5 do not result in a significant improvement of the drift correction process. Most of the time, drift shows up as a non-random, directed motion of the stage (see Figure 5.3). The level of precision increases as we increase the value of n, and we can see that the drift approaches a linear function in the rebinned image series. We can combine this rebinning approach with a linear regression fit without offset, in order to extract the theoretical displacement

of the stage at all times which is the used to correct the original image time series. This type of linear fit is shown in Figure 5.3 (for n = 5), and the corrected image series using the fit data shows no apparent drift.

## 5.3 STICS Applied to Cells

#### 5.3.1 Fixed Controls

In order to asses the detection limits of STICS under true imaging conditions with drift, we imaged CHO cells transfected with EGFP labeled Epidermal Growth Factor Receptor (EGFR), a cell surface signalling receptor which has been implicated in the development and progression of a number of human cancers including those of the lung, breast, prostate, colon, ovary, head and neck [107]. The CHO cells were fixed in 4% paraformaldehyde/PBS, a functional fixative that cross-links membrane proteins, thus killing and "freezing" the cell. Early FRAP studies have shown that protein motion stops after the cells have been fixed with paraformaldehyde above a concentration of 3.7% [108].

Several chemically fixed cells were imaged, at slow or fast scan speeds, to generate image time series with 100 frames and these were subsequently corrected for drift and analyzed by STICS to extract the x and y velocities of the labeled proteins. The imaging times were varied from 45 s to 10 min, and the sample drift and focus drift varied between the data sets. Fast scan samples showed no sample drift, whereas slow scan samples had to be corrected for drift. An extreme example of focus shift is shown in Figure 5.4A (basal membrane) and B (inside the cell). In this case the sample has drifted

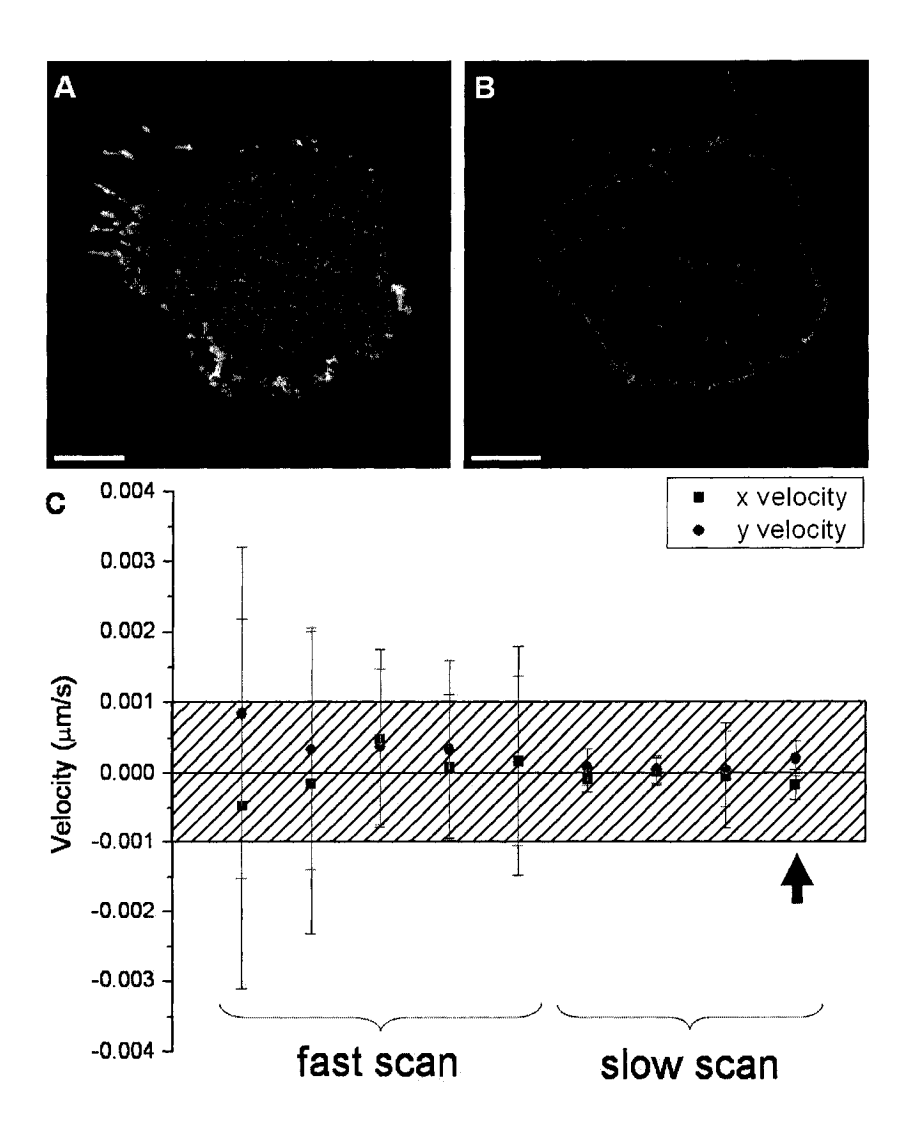


Figure 5.4: First (A) and last (B) frames of a confocal image time series of EGFP labeled EGFR receptor in CHO cells fixed in 4% paraformaldehyde (scale bars are  $5\mu m$ ). This is an extreme example of focal plane drift in z, combined with a small sample drift. C) Average STICS measured velocities for regions inside fixed cells, at different scan speeds. The arrow indicates the average x and y velocity measured for the case illustrated in A and B. The error bars are SD and the shaded region represents the deduced detection limit of  $\pm 0.001 \ \mu m/s$ .

down so the focal plane ends up inside of the cell as can be seen in the latter image (Figure 5.4B). We do not expect focal plane shifts to result in any

apparent velocity of the labeled protein because the intensity changes are only due to motion in the z direction. However, stage and sample motions in x-y will affect the STICS measurement and will set a lower limit on the velocities that can be measured. For the fixed cell experiments the STICS measured x and y velocities were less than 0.001  $\mu m/s$  (see Fig. 5.4C), thus establishing our lowest detection limit at typical confocal microscopy settings and sampling times. The larger errors for the fast scan setting are probably due to our inability to accurately detect a very small sample drift on the shorter time scales and thus correct for it. Longer imaging times allowed us to properly remove the sample drift and thus obtain a detection limit on the order of  $10^{-4}\mu m/s$ .

The fixed cell controls also allow verification that fluorescence photobleaching does not affect the accuracy of the STICS measurements. The bleaching curves for the samples analyzed in Figure 5.4, plotted as the relative intensity normalized to the first frame as a function of time, are shown in Figure 5.5. As expected the bleaching rate is not really dependent on the imaging rate, but rather on the total laser exposure time for the cells. As such, the fast scan samples bleach at a faster rate than the slow scan samples. In all cases, however, the STICS analysis was not affected and returned velocity magnitudes that were zero (within error), consistent with expectations for the fixed cells.

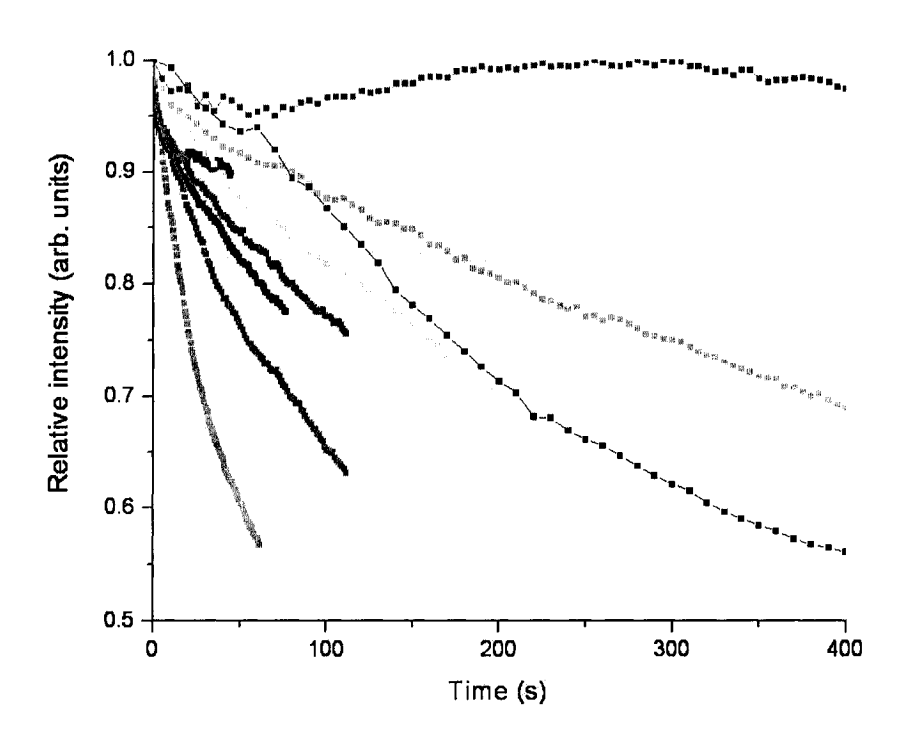


Figure 5.5: Photobleaching curves (mean intensity relative to the first frame mean versus time) for the fixed cell image time series analyzed from Figure 5.4C.

# 5.3.2 Diffusion, Non Directed Flow and Directed Flow in Living Cells

We used STICS to measure diffusion, directed and non-directed transport of EGFP/adhesion proteins expressed in living CHO cells. We first measured  $\alpha$ -actinin/EGFP constructs expressed in CHO-K1 cells plated on fibronectin coated substrates. The protein  $\alpha$ -actinin is a cytoplasmic molecule that binds to the integrins at the membrane and also links to the actin cytoskeleton [3]. We have previously determined that  $\alpha$ -actinin is more mobile in the peripheral regions of the CHO cells where there is active lamellar extension, retraction, and membrane ruffling when the cells are activated on fibronectin [2]. We focused our measurements on such active peripheral areas (see Figure

5.6).

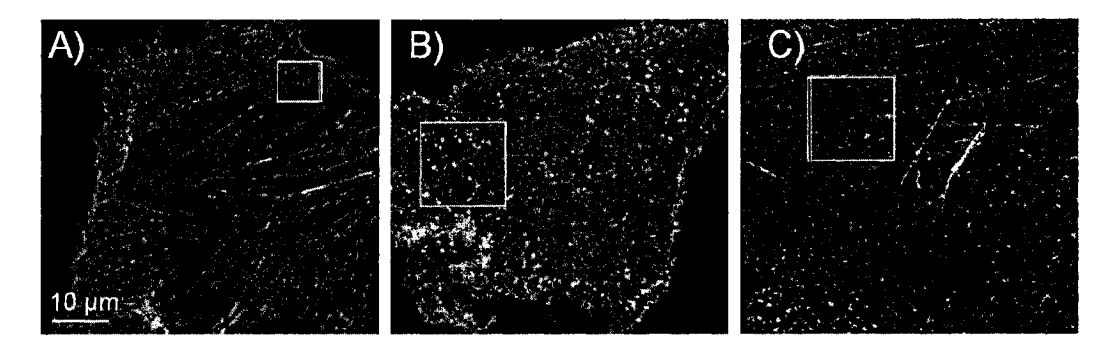


Figure 5.6: Two-photon LSM images of the basal membrane of CHO cells expressing EGFP labeled α-actinin. The cells were plated on fibronectin and imaged at 37°C. The regions analyzed with ICS and STICS are shown as white squares and the STICS analysis results are shown in Figures 5.7, 5.8 and 5.9. A) A 64² pixels region where the temporal autocorrelation function is best fit to a single population diffusion model (Eq. 2.10). B) A 128² pixels region where the temporal autocorrelation function is best fit to a two population flow/diffusion model (Eq. 2.13). C) A 128² pixels region where the temporal autocorrelation function is best fit to a two population flow/diffusion model (Eq. 2.13). All images are 512 by 480 pixels at a resolution of 0.118 μm/pixel, and a total of 180, 360, 120 frames at a temporal resolution of 5, 5 and 15 s/frame for A), B) and C) respectively.

Figure 5.7 shows the ICS and STICS analysis results for a typical  $64 \times 64$  pixels<sup>2</sup> region from the cell periphery (Fig. 5.6A). As is evident from Figure 5.7B, the temporal autocorrelation function can be fit very well by Eq. 2.10, which yields a diffusion coefficient of  $(9 \pm 1)10^{-4} \mu m^2/s$ . We show contour plots of the spatio-temporal correlation functions for different time lags in Figure 5.7A for i) the unmodified image time series (without the immobile population removed) and ii) the filtered image time series (with the immobile population removed). As expected for isotropic diffusion, in both cases the correlation peaks stay centered at zero spatial lags (indicated by the white

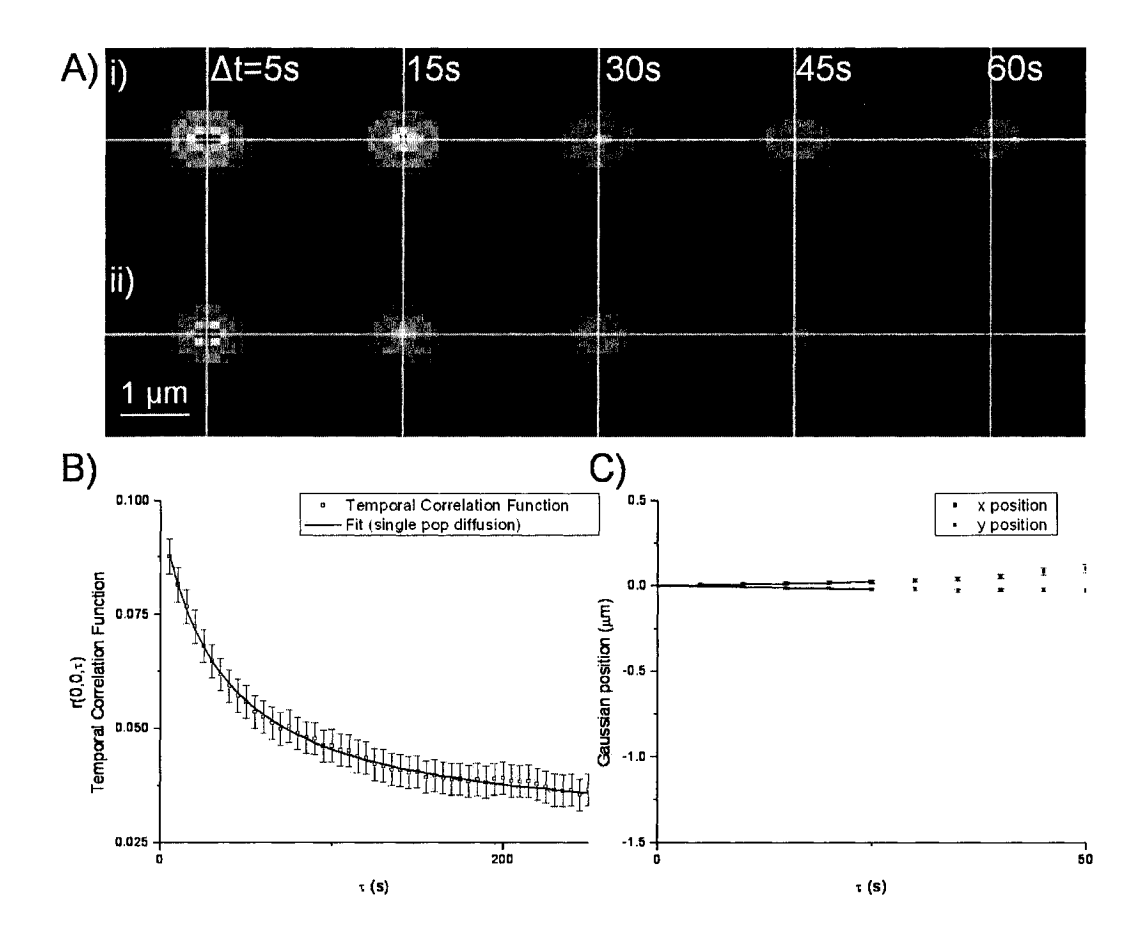


Figure 5.7: In vivo ICS and STICS analysis of protein diffusion in a peripheral basal membrane region of a CHO cell (Fig. 5.6A) expressing EGFP labeled  $\alpha$ -actinin. A) Contour plots of spacetime correlation functions from STICS analysis (Eq. 2.16) as a function of lag time for i) without and ii) with the immobile population filtering. B) A plot of the ICS temporal autocorrelation function and best fit to a single population diffusion model (Eq. 2.10). The recovered diffusion coefficient was  $D = (9 \pm 1)10^{-4} \mu m^2/s$ . C) Peak tracking plot of the STICS correlation peak reveals that it stays centered at zero spatial lags, within the precision of our measurement.

cross-hairs). Fitting for the displacement of the Gaussian yields a very small velocity  $v_{STICS} = (1.2 \pm 0.8)10^{-3} \ \mu m/s$  (from  $v_x = (-0.9 \pm 0.8)10^{-3}$  and  $v_y = (-0.8 \pm 0.7)10^{-3} \ \mu m/s$ , see Figure 5.7C) which cannot be attributed to a very slow concerted flux of the proteins, since these values are on the order

of the detection limit of our measurements, which was determined by applying the STICS analysis to cells fixed in 4% paraformal dehyde (see section 5.3.1). These results illustrate a membrane region exhibiting mainly slow protein diffusion and immobile proteins, and show how the random walk is manifest in both the ICS and STICS analyses. It probably represents  $\alpha$ -actinin that is bound to membrane integrins (that are diffusing or immobile) and not bound to actin as flow was not detected.

The same analyses were applied to a different region from the periphery of another cell (Figure 5.6B) and reveal different protein transport. Figure 5.8 shows our results for a  $128 \times 128$  pixels<sup>2</sup> region in which clusters of  $\alpha$ -actinin are clearly resolved, and these clusters can be observed to flow in a directed fashion on what appear to be defined linear tracks. However, the ICS (Figure 5.8B) and STICS (Fig. 5.8A,C) analyses yield very different values for the flow speed:  $v_{ICS}=(13\pm1)10^{-3}~\mu m/s$  and  $v_{STICS}=(1.1\pm0.7)10^{-3}$  $\mu m/s$  (from  $v_x = (-0.67 \pm 0.02)10^{-3}$  and  $v_y = (-0.9 \pm 0.8)10^{-3} \ \mu m/s$ ). The velocity magnitude from ICS analysis is about 10 times higher than the velocity value measured by STICS. This is due to the fact that STICS only measures the net resultant directed component (here the majority, but not all of the clusters were observed to be traveling to the left and down in the image series), whereas ICS measures an average total flow speed (and a small diffusion coefficient in this case) as it is not sensitive to the direction of flow. Hence the combination of ICS and STICS allows us to distinguish between unidirectional flow (see also Figure 5.9), or directional flow in many random directions as was the case here. Visual tracking of the resolved clusters shows that the directions are mostly random with a slight bias towards the lower

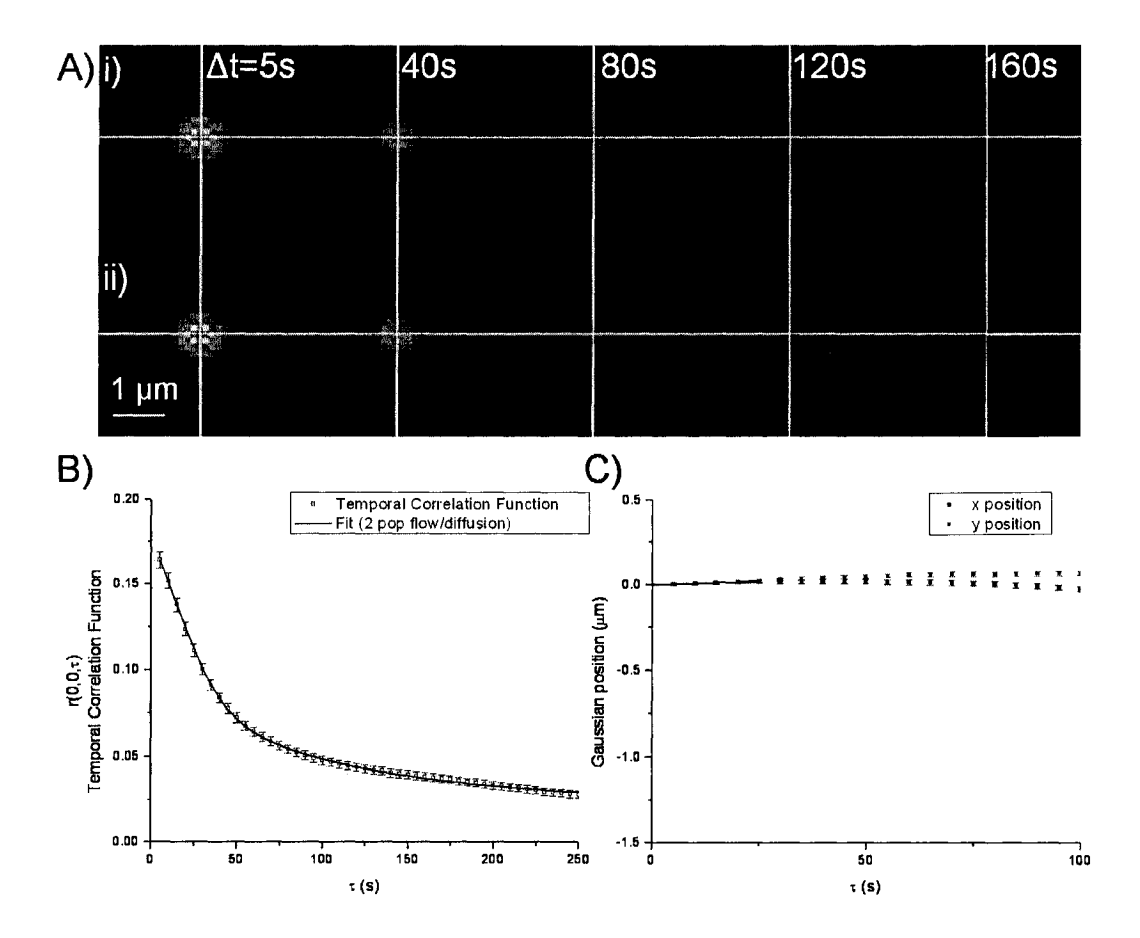


Figure 5.8: In vivo ICS and STICS analysis of protein flux in random directions in a peripheral basal membrane region of a CHO cell (Fig. 5.6B) expressing EGFP labeled  $\alpha$ -actinin. A) Contour plots of space-time correlation functions from STICS analysis as a function of time for i) without and ii) with the immobile population filtering. B) A plot of the ICS temporal autocorrelation function and best fit to a two-population flow/diffusion model (Eq. 2.13). The recovered ICS velocity and diffusion were  $v_{ICS} = (13 \pm 1)10^{-3} \ \mu m/s$  and  $D = (8 \pm 1)10^{-4} \ \mu m^2/s$ . C) Peak tracking plot of the the STICS correlation peak reveals that it stays centered at zero spatial lags, within the precision of our measurement, yielding a very small resultant velocity of  $v_{STICS} = (1.1 \pm 0.7)10^{-3} \ \mu m/s$ .

left of the image. In this case, single particle tracking (SPT) analysis will in principle provide more information about the range of transport [56]. However, it proved difficult to track the clusters with the fluorescence signal to

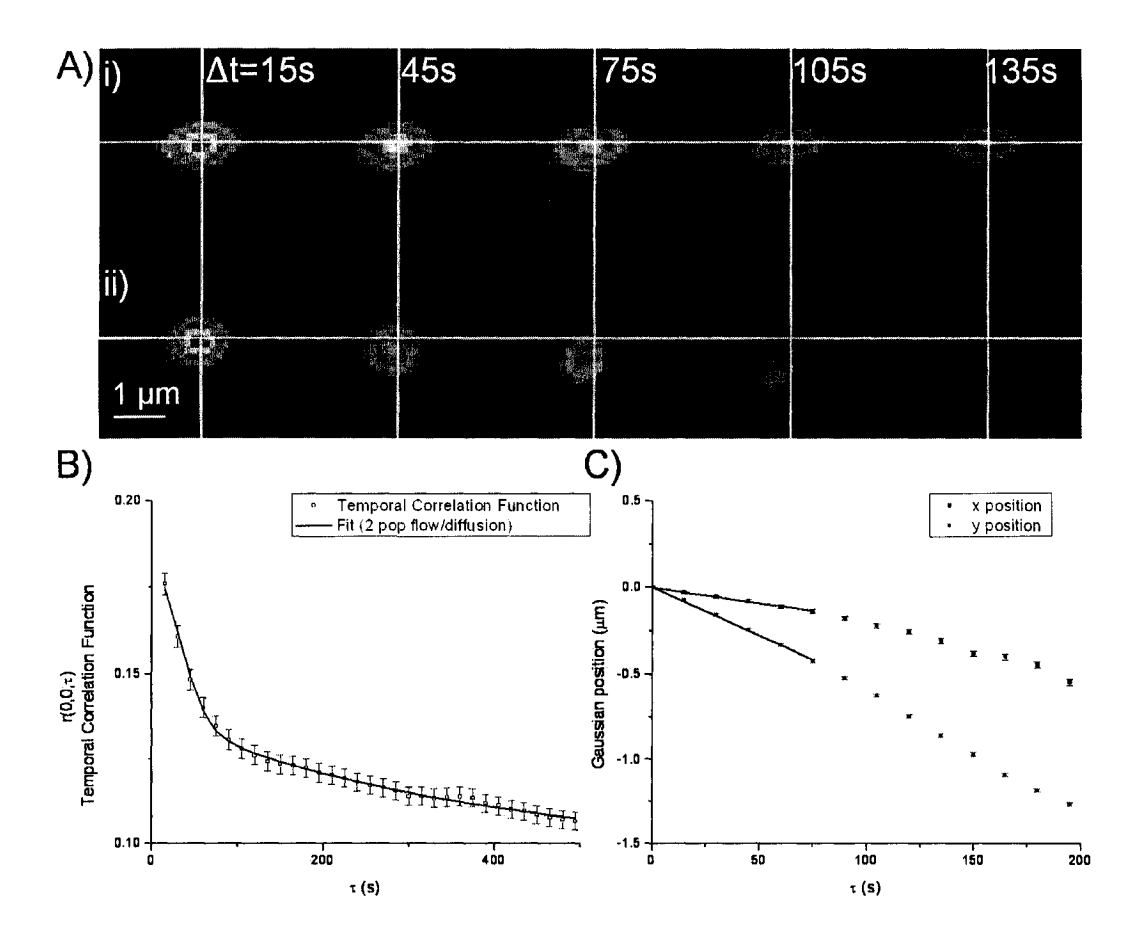


Figure 5.9: In vivo ICS and STICS analysis of directed protein flow in a peripheral basal membrane region of a CHO cell (Fig. 5.6C) expressing EGFP labeled  $\alpha$ -actinin. A) Contour plots of spacetime correlation functions from STICS analysis as a function of time for i) without and ii) with the immobile population filtering. B) A plot of the ICS temporal autocorrelation function and best fit to a two-population flow/diffusion model (Eq. 2.13). The recovered velocity was  $v_{ICS} = (7.7 \pm 0.8)10^{-3} \ \mu m/s$  and a small diffusion coefficient was measured:  $D = (6 \pm 1)10^{-5} \ \mu m^2/s$ . C) Peak tracking plot of the STICS correlation peak (after the immobile population removal) shows a net peak displacement from the zero lags center, yielding velocities of  $v_x = (1.8 \pm 0.3)10^{-3}$  and  $v_y = (5.5 \pm 0.2)10^{-3} \ \mu m/s$ .

noise ratio and for the density of expression of EGFP proteins typical for these transfected cells.

The true advantage of STICS emerges in situations where no bright clusters are clearly resolved (hence SPT would be impossible), but concerted flux of protein can still be detected and quantified by correlation analysis. Figure 5.9 shows results for a 128x128 pixels<sup>2</sup> region of a basal membrane of a CHO cell expressing EGFP labeled  $\alpha$ -actinin (Figure 5.6C). Here the ICS analysis again detects the flow and diffusion of two separate populations (Figure 5.9B) with  $v_{ICS} = (7.7 \pm 0.8) 10^{-3}~\mu m/s$  and a small diffusion coefficient  $D = (6 \pm 1)10^{-5} \ \mu m^2/s$ . The STICS analysis also detects a directional flow (Figure 5.9A,C) with  $v_x = (1.8 \pm 0.3) 10^{-3}$  and  $v_y = (5.5 \pm 0.2) 10^{-3} \ \mu m/s$ . This example illustrates again the importance of removing the immobile population, since the correlation function peak in Figure 5.9A i) is dominated by immobile protein population spatial correlations and thus roughly stays centered at zero spatial lags. However, after the immobile population removal, one can see and track the Gaussian peak clearly moving away from the zero lags center towards the bottom left corner and the residual zero lags centered peak from the diffusing population (Figure 5.9A ii).

# 5.4 STICCS Applied to cells

#### 5.4.1 Fluorescent Microsphere Control Experiments

Fluorescent microsphere samples containing a mixture of non interacting flowing spheres emitting at two different wavelengths (referred to as "red" and "green") were prepared and imaged as a function of time by two-photon laser scanning microscopy (see Materials and Methods) to generate an image series of two independent particle populations. By adding another image series of flowing microspheres to both independent channels in the collected

122

time series, we could effectively introduce an artificial interacting population (i.e. one that appeared in both image series which models different fluorophores being detected at the same pixel locations in the two detection channels). The direction of flow of this "interacting" population added by image processing was set by the user and is thus independent of the direction of flow of the original non-interacting particle populations. A typical overlay image from these image processed time series is shown in Figure 5.10A. It has an equal density of red and green microspheres, with approximately 40% of each population interacting.

These image time series were then analyzed with two-color STICCS, yielding directional flow information for the red and green populations, as well as for the interacting fraction. We can recover the flow directions of the noninteracting red and green microsphere populations to within 8 degrees in the presence of the interacting population, as compared with the recovered flow directions of the original image time series (i.e. analysis performed without the addition of the interacting population). Moreover, we can find the direction of flow of the interacting population to within 5 degrees. Figure 5.10B shows the one to one relationship between the velocity magnitudes (in x and y) for the added population as measured by STICS from its original image time series before addition and the velocity magnitude of the added (interacting) population as measured by STICCS in the dual channel constructed image time series (i.e. in the presence of the non interacting microsphere populations). The data are plotted for several experiments in which the direction of flow of the added interacting population was varied. The magnitudes of the velocities measured by STICS analysis on the dual channel

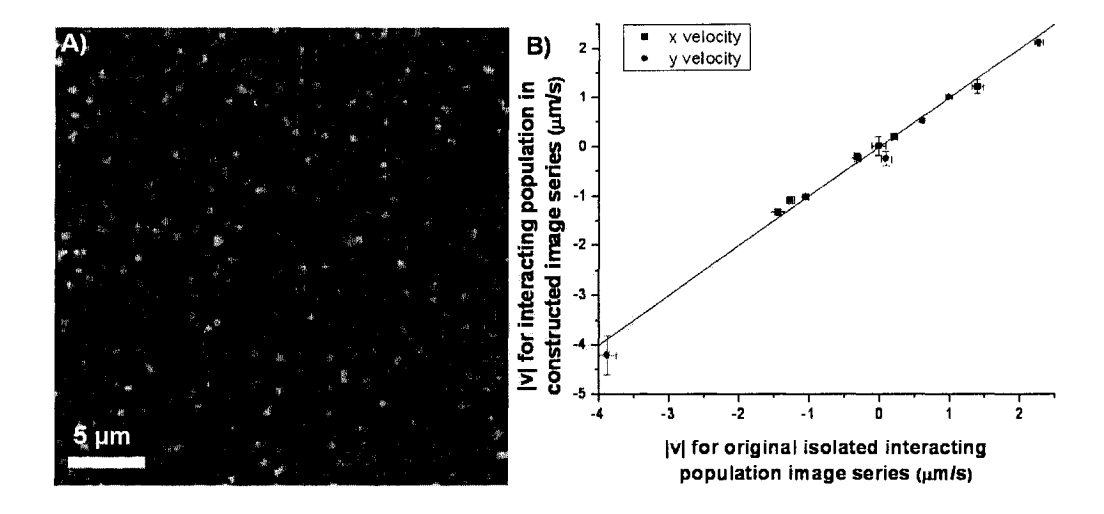


Figure 5.10: A) A composite image of fluorescent microspheres consisting of two different fluorescent particle populations (red and green) and an added "interacting" particle population (yellow). The composite image was made by adding an independent image of fluorescent spheres (our artificial interacting population) to both detection channel images. For each image time series constructed, the velocities of the non interacting populations remained constant whereas the interacting fraction's direction of flow was systematically changed. B) A plot of the interacting population velocity magnitudes in x and y measured by STICCS in the composite image series (i.e. with the added population and the red and green microspheres all present) versus the velocity magnitude of the introduced interacting population measured by STICS in its original image series (i.e. without the red and green particles present).

image time series differ by less than 10% from the original values (as measured separately before the addition of the artificial interacting population); see Tables 5.1 and 5.2. Note that the density of the added interacting particle population was five times lower than the densities of the independent green and red particle populations.

Set	first population		second population	
	(green)		$(\mathrm{red})$	
#	velocity $(\mu m/min)$		velocity $(\mu m/min)$	
	$v_x$	$v_y$	$v_x$	$oxed{v_y}$
1	$0.11 \pm 0.04$	$-1.53\pm0.05$	$0.14 \pm 0.05$	$-1.48\pm0.05$
2	$0.27 \pm 0.05$	$-1.24\pm0.04$	$0.30 \pm 0.03$	$-1.22\pm0.05$
3	$0.03\pm0.01$	$-1.00\pm0.10$	$0.16 \pm 0.03$	$-1.23\pm0.05$
4	$0.03\pm0.06$	$-1.08\pm0.06$	$0.11 \pm 0.09$	$-0.98\pm0.04$
5	$0.02 \pm 0.05$	$-1.27 \pm 0.03$	$0.03 \pm 0.05$	$-1.20\pm0.05$
6	$0.12 \pm 0.02$	$-0.51 \pm 0.05$	$0.17 \pm 0.03$	$-1.63\pm0.05$

**Table 5.1:** STICCS measured parameters for an image time series of flowing microspheres (see Figure 5.10). Shown here are the x and y velocities of the green and red microspheres as recovered by the STICCS analysis. Errors are SD from 4 separate measurements.

Set	isolated interacting		interacting population	
#	population velocity		velocity $(\mu m/min)$	
	$(\mu m/min)$			_
	$v_x$	$v_y$	$v_x$	$v_y$
1	$-0.01\pm0.05$	-3.9±0.1	-0.01±0.09	-4.2±0.2
2	$1.39 \pm 0.04$	$0.09\pm0.04$	$1.21 \pm 0.07$	$-0.25 \pm 0.05$
3	$-1.26\pm0.03$	$2.27 \pm 0.03$	$-1.08\pm0.04$	$2.13\pm0.04$
4	$-1.44 \pm 0.03$	$0.60 \pm 0.01$	$-1.33\pm0.03$	$0.52 \pm 0.03$
5	$-0.31 \pm 0.03$	$-1.05\pm0.02$	$-0.22 \pm 0.05$	$-1.02\pm0.05$
6	$0.21 \pm 0.02$	$0.98 \pm 0.02$	$0.19 \pm 0.02$	$-1.00\pm0.02$

Table 5.2: STICS measured parameters for an image time series of flowing microspheres (see Figure 5.10). The column "isolated interacting population velocity" refers to the STICS analysis results before image addition when applied to the single channel image time series that is subsequently added to the dual channel image time series to create the interacting population. The column "interacting population velocity" refers to the two-color STICCS analysis results after image addition for the co-localized (interacting) population in the composite image. These values should, in theory, be equal to the values in the column "isolated interacting population velocity". Errors are SD from 4 separate measurements.

The STICCS analysis for the single non-interacting populations is influenced by both the fraction that is flowing independently and the movements of the interacting fraction (i.e. there are two directions of flow in these image time series). As long as the overall contribution to the image intensity from the interacting population does not exceed that of the non-interacting population (for example 80% of the population is flowing independently and 20% is interacting), STICS can detect the differences in flow direction between the populations. In situations where this effect becomes dominant (i.e.: equal contribution from interacting and non-interacting species), one can fit two Gaussians to the spatial correlations of Eq. 2.6  $(r_{aa}(\xi, \eta, \tau), a=1 \text{ or a=2})$ to extract the two flow directions. Conversely, the STICCS analysis of the interacting population can also be influenced by the single non-interacting populations if these happen to flow in the same direction and random spatial cross-correlations occur. These effects account for the errors in magnitude and direction of the measured velocities in the constructed image series as compared with the velocities measured from the original image series of the independent microspheres.

# 5.4.2 STICCS Measurement of Concerted Flow of Labeled Proteins in Cells

To verify the STICCS analysis in living cells, we chose epidermal fish keratocytes because they are thought to exhibit internal fluid flow during migration. The cells were electroporated to introduce fluorescent tracer particles in their interior (for full experiments and discussion see section 6.2). In short, these tracers are small and inert so they do not show any interaction with the actin cytoskeleton or other components and are, therefore, expected to move with

any fluid flow within the cell. Hence when we electroporate fish keratocyte with two kinds of tracer particles and image the different emission wavelength, we expect that both of these tracers will show the same transport behavior as they will both reflect fluid flow inside the cell.

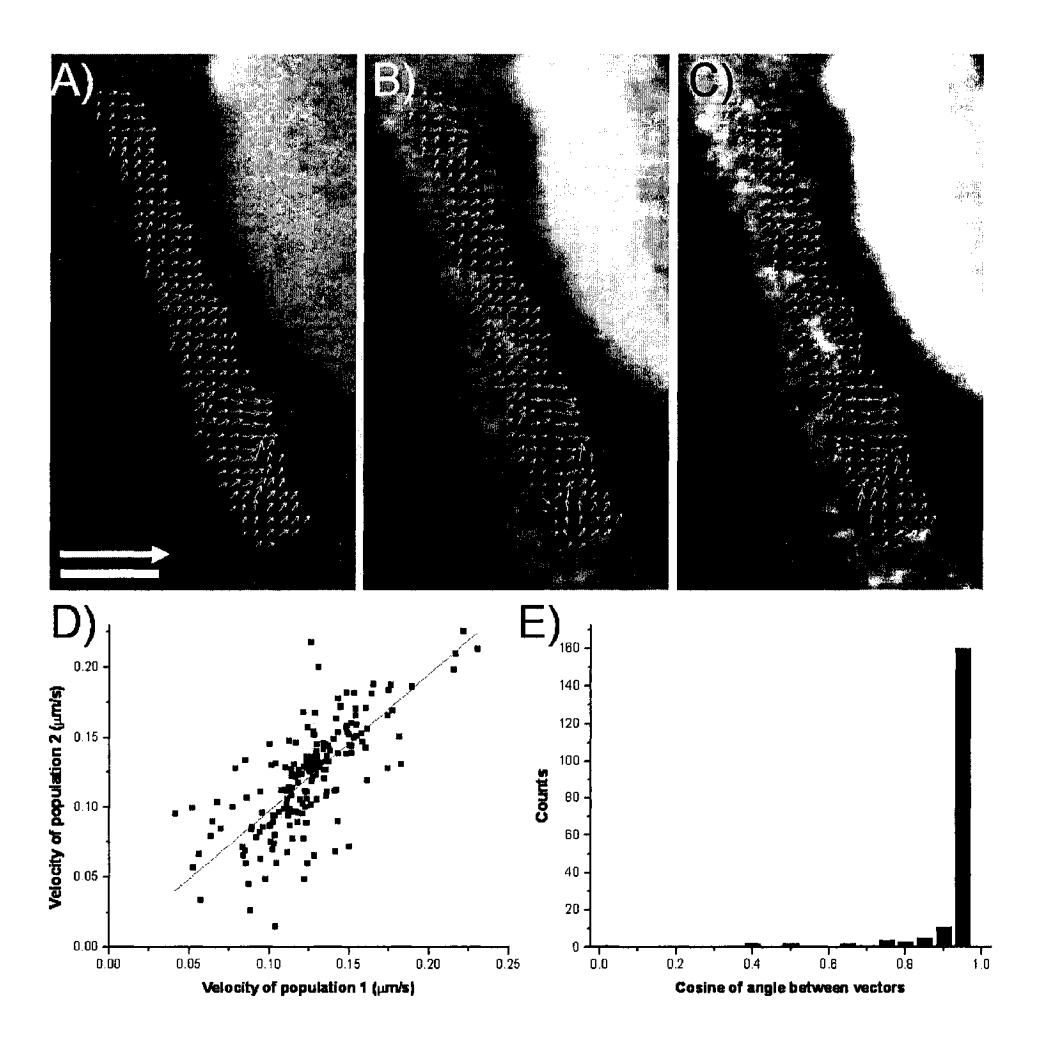


Figure 5.11: STICS measured velocity maps for A) Alexa Fluor 488 B) 655QDs and C) the STICCS measured cross-correlation velocity map. Scale bar is 10 μm, velocity scale vector is 1 μm/s. D) Magnitude and E) directional correlation plots for fluid flow fields measured from the movements of the two different tracers in the same cell.

Using wide-field fluorescence microscopy, we imaged fish keratocytes electroporated with 655QDs (quantum dots with emission at 655nm) and AF488 (Alexa Fluor 488nm), using two channel detection with minimal bleedthrough (less than 1%). The two resulting image series were analyzed individually using STICS to reveal the flow patterns as mapped for each fluorescent tracer. Magnitude and directional correlation analysis (as described in section 3.5) shows that both flow fields are very similar as expected (see Figure 5.11A-B). The magnitude correlation coefficient was  $0.98 \pm 0.06$  and the directional correlation coefficient was  $0.991 \pm 0.002$  (see Figure 5.11D-E), indicative of quasi-identical flow fields. We also performed the magnitude and directional correlation analysis between the AF488 map (Figure 5.11A) and the STICCS measured cross-correlation map (Figure 5.11C), as well as between the 655QD map (Figure 5.11B) and the cross-correlation map to verify that the two channel cross-correlation velocity map was accurate. The former resulted in a magnitude correlation of  $0.93 \pm 0.06$  and a directional correlation of  $0.994 \pm 0.002$ ; while the latter yielded values of  $0.97 \pm 0.08$  and  $0.983 \pm 0.003$ for the same correlation coefficients. These results show that STICCS is able to accurately detect and measure concomitant flow fields of two different labeled tracers in situ.

# 5.5 Chapter Conclusion

Spatio Temporal Image Correlation Spectroscopy provides a unique tool to study protein motion *in situ*. The control measurements performed on chemically fixed cells presented in this chapter indicate that, after background noise removal and drift correction, the velocity detection limits of STICS are

low enough ( $\sim 0.001~\mu m/s$ ) that we can readily measure typical retrograde flow velocities of adhesion proteins and actin in cells ( $\sim 0.01-0.1~\mu m/s$ ). Furthermore, the immobile population removal algorithm was successfully applied to STICS data obtained from living cells in order to remove the contributions of large, static molecular complexes to the spatial correlation function. This permits the use of the STICS analysis even in regions where there is a significant immobile population fraction, and spatially non-uniform distributions of labeled proteins.

ICS is sensitive to flow regardless of the direction, since the temporal correlation measures intensity fluctuations in time irrespective of the (spatial) direction in which particles enter and exit exit the beam focal volume. On the other hand, STICS only registers concerted flow motion, because it yields a directionally weighted net resultant correlation peak due to all flows. By combining both ICS and STICS, we have demonstrated the ability to distinguish between cases of diffusion, flow in random directions and concerted directional flow in living cells. Finally, the cross-correlation applications of STICS and STICCS were tested using control experiments with fluorescent microspheres to generate image time series where we could artificially add an interacting population. These experiments show that we can recover the flow directions of the non-interacting and interacting populations to within a few degrees. STICCS was also applied in situ using two fluorescent tracers introduced into fish epidermal keratocyte, where fluid flow is expected to carry both tracers with the same velocity magnitude and direction. The measured magnitude and directional correlation coefficients show that STICCS can accurately measure perfectly concomitant flow of two fluorescent markers.

# 6 Velocity Mapping applications in living cells

### 6.1 The Molecular Clutch

Cell migration is regulated, in part, by the connection between adhesion components and the actin cytoskeleton. However, the very large number of proteins involved in the linkage from the substratum to actin and their complex network of interactions (see section 1.3) make it difficult to directly assess their role in migration of living cells. In this section, STICS experiments to characterize the protein linkage between integrin and actin, and identify points of slippage or disconnect in this linkage in migrating cells will be described and discussed.

#### 6.1.1 Cell Adhesion Mechanisms

Cell protrusion and adhesion are essential features of cell migration and contribute to many processes such as cancer metastasis, embryonic development, and inflammation, as well as the formation of synaptic connections in the central nervous system [8]. Cell migration results from the integration of several component processes including the formation and stabilization of protrusions and the assembly and disassembly of adhesions [3, 8]. While protrusions are generated by actin polymerization, the protrusion rate can be modulated by the relative rate of retrograde actin flow, which is adhesion dependent [68, 109]. The assembly of adhesions is regulated, in part, by the tension sensed by adhesions, which serve as both signalling centers and traction points for the generation of tension [8, 110]. Therefore, adhesion and protrusion are interconnected, and are controlled by the efficiency of the linkage between actin and the extracellular matrix (ECM). Thus, it is not

surprising that this linkage emerges as a potential site for molecular regulation of protrusion and migration.

Despite its importance, only a few studies have addressed the ECM-actin linkage and its regulation in migrating cells. The role of integrins in the linkage has been studied in retracting regions at the rear of migrating cells [111, 112, 113]. In these regions, the linkage severs between integrin and other adhesion components leaving integrin-containing residual "footprints" on the substratum, often with an accompanying sliding of the remaining adhesion [112, 113, 114]. The amount of integrin in the footprints depends on parameters that contribute to adhesion strength such as the concentration of ECM proteins, the number of integrin receptors, the affinity of integrin for the ECM, as well as calpain activity [111]. These observations suggest that for retracting regions of the cell, the bond between the ECM and integrin is much stronger than that linking integrin to the cytoskeleton [111, 112, 113]. Recently, paxillin was observed to be associated with footprints in focal adhesion kinase (FAK) null cells, suggesting FAK regulates a labile site in the linkage [21]. These observations lead to a hypothesis in which the linkage between the ECM and actin is regulated by changes in interactions among linkage components through the action or modification by signalling molecules such as src, paxillin and focal adhesion kinase (FAK). The challenge, therefore, is to define the nature and regulation of the linkage at the molecular level in migrating cells.

A plethora of in vitro studies point to interactions among integrin, talin, vinculin,  $\alpha$ -actinin, and actin as likely critical elements of the linkage [115,

116, 117]. Adhesion associated signaling components, like FAK, Src, and paxillin, could then regulate the ECM-actin linkage through modifications that result in altered affinities, e.g., phosphorylation or enzymatic cleavage of proteins that comprise the linkage. Such studies would benefit greatly from quantitative estimates of the efficiency of the linkage in situ and the roles of various adhesion components in determining its efficiency and where the points of linkage are actually located. It is difficult to clearly define and characterize the molecular basis of the ECM-integrin-actin linkage in living cells because of the small volume of the cell, the complex spatio-temporal interactions between integrins and adhesion proteins [20] and the diverse kinetic and kinematic behaviors of the cytoskeleton [69].

Recently, there have been significant advances in cellular imaging tools and techniques that allow this problem to be approached via direct measurements inside cells. In situ experiments using chromophore-assisted laser inactivation (CALI) have implicated talin as a critical molecule in the ECM-actin linkage during filopodial extension and retraction [118]. More recently, extensive characterization of actin dynamics using Fluorescent Speckle Microscopy (FSM) [66] has revealed two spatially, kinetically and kinematically distinct actin networks; with the local expansion of the lamella network being a source of persistent cell protrusion [69]. There is also evidence that the actin network is dynamically coupled to adhesions [103, 119] by a biphasic relationship between the retrograde flow of actin and the cell-substratum adhesiveness [103]. Nevertheless, to date, the dynamics of the integrin linkage to actin has not been systematically studied during cell migration.

In this section we apply STICS to determine protein flow velocities throughout the cell and use these measurements to explore how F-actin based motility is regulated by interactions with adhesion components. We will quantify  $\alpha$ -actinin retrograde velocities and compare them to actin retrograde flow, and then apply STICS to generate co-transport maps of actin and a set of adhesion proteins within sub-regions of the basal membrane in doubly transfected cells. The detailed cellular maps of molecular transport allow us to quantify the coupling between adhesion components and actin and thus provide new insight about the mechanistic details of the integrin-actin linkage during cell protrusion and migration.

### 6.1.2 Retrograde Flow

The ubiquity of actin retrograde flow [109] and recent evidence for directed motion of some adhesion proteins [1, 2] suggest that we can study the coupling between the actin cytoskeleton, adhesions and ECM at the molecular level by measuring protein velocities. We transfected mouse embryonic fibroblasts (MEFs) with an  $\alpha$ -actinin-GFP expressing cDNA, and imaged the cells using TIRM (see section 2.3.4), which excites only the molecules within  $\sim$ 100 nm of the coverslip. Even for the few image series where movement of  $\alpha$ -actinin could be seen by eye, the density of labeled protein along actin filaments was too high to perform SPT or FSM measurements.

As described in section 2.6, STICS analysis relies on averaging two dimensional spatial correlation functions calculated from fluorescence intensity fluctuations. Large spatially extended bright fluorescent structures in the image time series will dominate and distort the spatial correlations, making

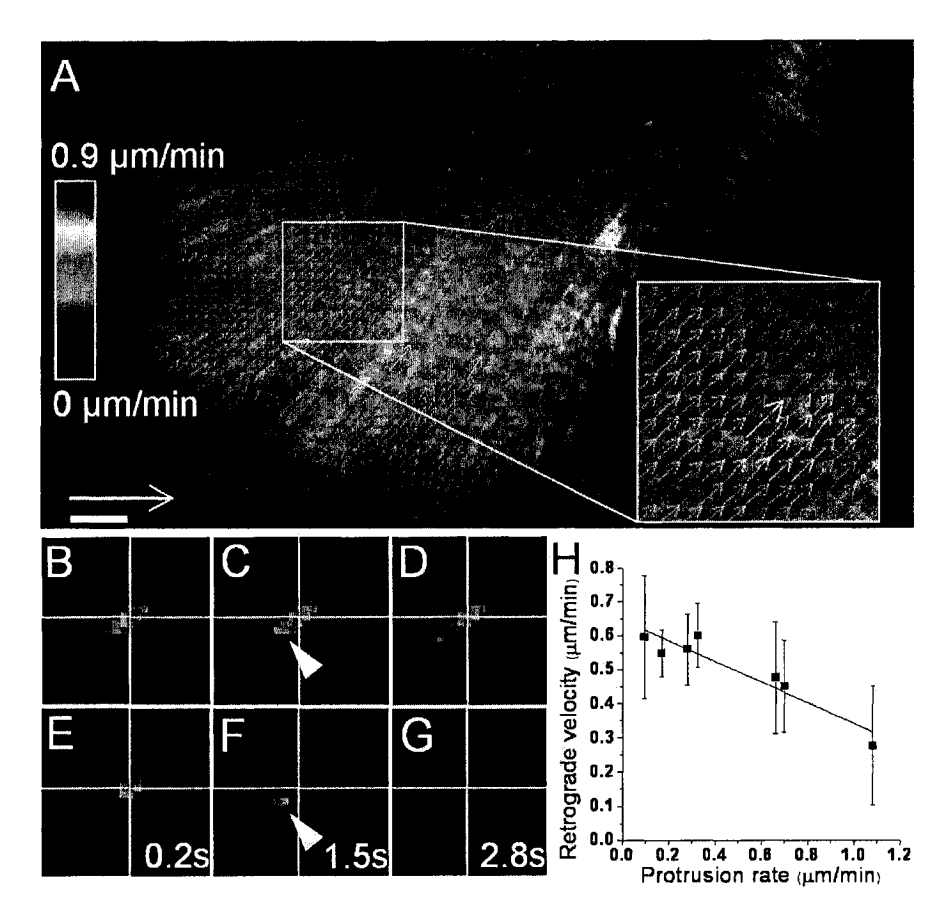


**Figure 6.1:** A) STICS measured velocity map of  $\alpha$ -actinin-GFP in an MEF cell image time series (100 frames, 10 s/frame), color coded for velocity magnitude (spatial scale bar is 5  $\mu$ m, velocity scale vector is 5  $\mu$ m/min). The analysis to generate this map took approximately 10 minutes, using partially overlapping 16×16 pixels<sup>2</sup> boxes. The inset shows an expanded region of the velocity map. STICS correlation flow peak tracking is nearly impossible without immobile population filtering (B-C-D). After immobile population removal (E-F-G), a clear displacement of the flow peak can be observed (white arrow head) and tracked to reveal the direction and magnitude of the velocity. Using this filtering, the contribution of the large static features and other immobile proteins to the correlation function are removed. H) Inverse relationship between cell protrusion rate (measured by kymograph analysis) and STICS measured retrograde velocity for  $\alpha$ -actinin. Error bars are SD.

the tracking of the correlation peak due to flow unfeasible. The  $\alpha$ -actinin organizes along actin filaments which appear as extended filamentous structures in the images and remain visibly static over the imaging periods. We used the immobile filtering algorithm to remove the immobile component which eliminated the perturbing contribution of these bright static spatial structures from the correlation function (see section 2.7). As described before, if the immobile component is not removed, then the flow peak of the correlation function is "buried" under the static spatial correlations of the filament structures (Figure 6.1B-D). However, after the algorithm is applied one can easily see and track the flow peak (see Figure 6.1E-G, lower left quadrant). This algorithm allowed us to map the retrograde movement of  $\alpha$ -actinin along organized actin filament structures.

Forces driven by actin polymerization push the membrane forward generating protrusion [68], while membrane resistance to this pressure combined with myosin activity leads to retrograde actin flow. Using STICS, velocity maps were generated in protruding regions of cells where we found that  $\alpha$ -actinin was undergoing retrograde flow with rates ranging mostly from 0.2 to 0.7  $\mu$ m/min (Figure 6.1A). These rates are comparable to those previously measured for actin [67]. We found an inverse relationship between the  $\alpha$ -actinin retrograde velocities and the cell protrusion rates (measured by kymograph analysis across the moving membrane edge boundary [103, 120]), which is also analogous to what others have seen for actin [121] (Figure 6.1H). The measurement of  $\alpha$ -actinin velocities and an inverse relationship between velocities and protrusion rates comparable to actin validates and establishes

the generality of the STICS method for an arbitrarily expressed fluorescent protein.

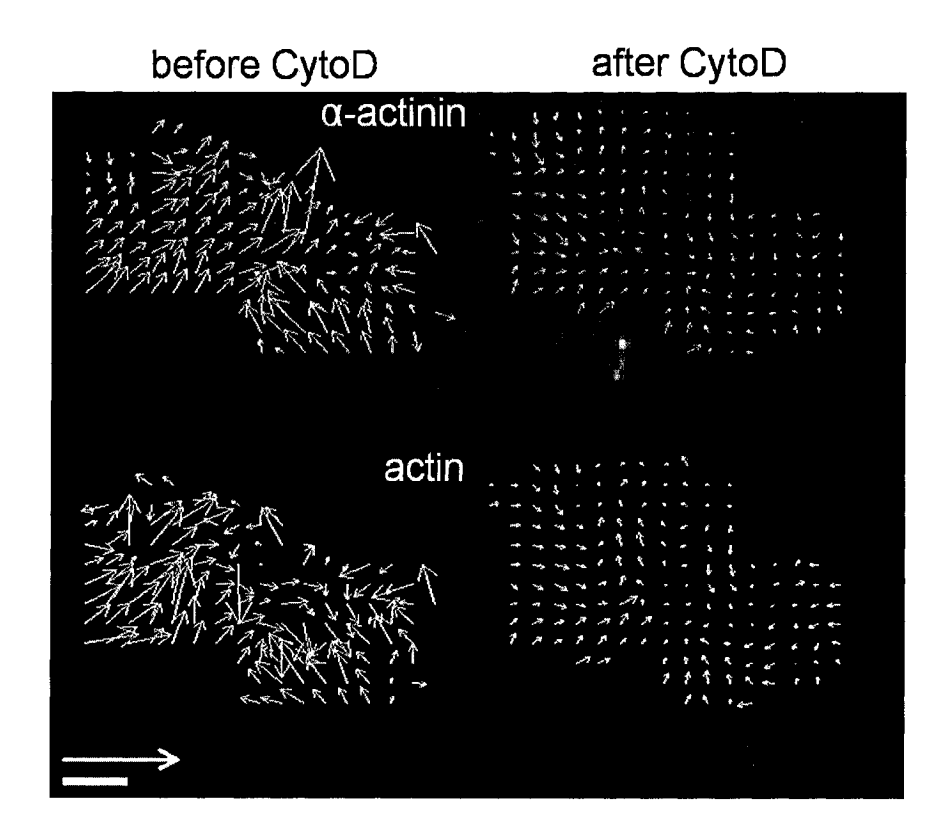


Figure 6.2: Velocity maps of  $\alpha$ -actinin and actin before and after treatment with Cytochalasin D (200 nM). Spatial scale bar is 5  $\mu$ m, velocity scale vector is 1  $\mu$ m/min. The image time series were 200 frames at 5 s/frame.

## 6.1.3 Hidden mobility and velocity perturbations

When analyzing the co-transport of adhesion proteins and actin, two simultaneous cellular velocity maps are generated for image series collected in two detection channels (one for each labeled protein). The absolute values of the protein velocities cannot be directly compared among different cells due to the dependence of the retrograde velocities on the protrusion rate, substrate

adhesiveness and the rate of actin polymerization which varies between cells [121]. Therefore, only velocities relative to the velocity of actin within a given cell contain useful information about the degree of interaction between actin and the adhesion proteins. Moreover, spatial variations in the rates of actin retrograde flow in the lamella dictate that the comparison between flow fields should be done locally. To probe the role of myosin II and actin polymerization in protrusion and their effect on the integrin-actin linkage in the lamella, we focused on the  $\alpha$ -actinin/actin protein pair and performed cellular pharmacological (drug) perturbations to actin polymerization and filament contraction.

Cells were imaged before and after treatment with cytochalasin D (cytoD), which inhibits the polymerization of actin free barbed ends [122] and therefore stops cell protrusion. The velocity maps of  $\alpha$ -actinin and actin computed before and after treatment (see Figure 6.2) revealed that both the actin and the  $\alpha$ -actinin velocities were markedly reduced following cytoD treatment. The average actin velocity decreased from  $0.22 \pm 0.01$  to  $0.063 \pm 0.002 \ \mu\text{m/min}$  and the average  $\alpha$ -actinin velocity from  $0.19 \pm 0.01$  to  $0.058 \pm 0.002 \ \mu\text{m/min}$ , a reduction of a factor of 3 in each case (Figure 6.3A, compare before and after CytoD). Nevertheless, although the mean velocity of both actin and  $\alpha$ -actinin decreased after CytoD treatment, their mobility was still correlated as their relative magnitude (0.98  $\pm$  0.20 before and 1.0  $\pm$  0.3 after treatment) and directional correlation coefficients (0.90  $\pm$  0.03 before and 0.91  $\pm$  0.03 after treatment) remained unaffected (Figure 6.3B, see section 3.5 for the definition of the correlation coefficients).

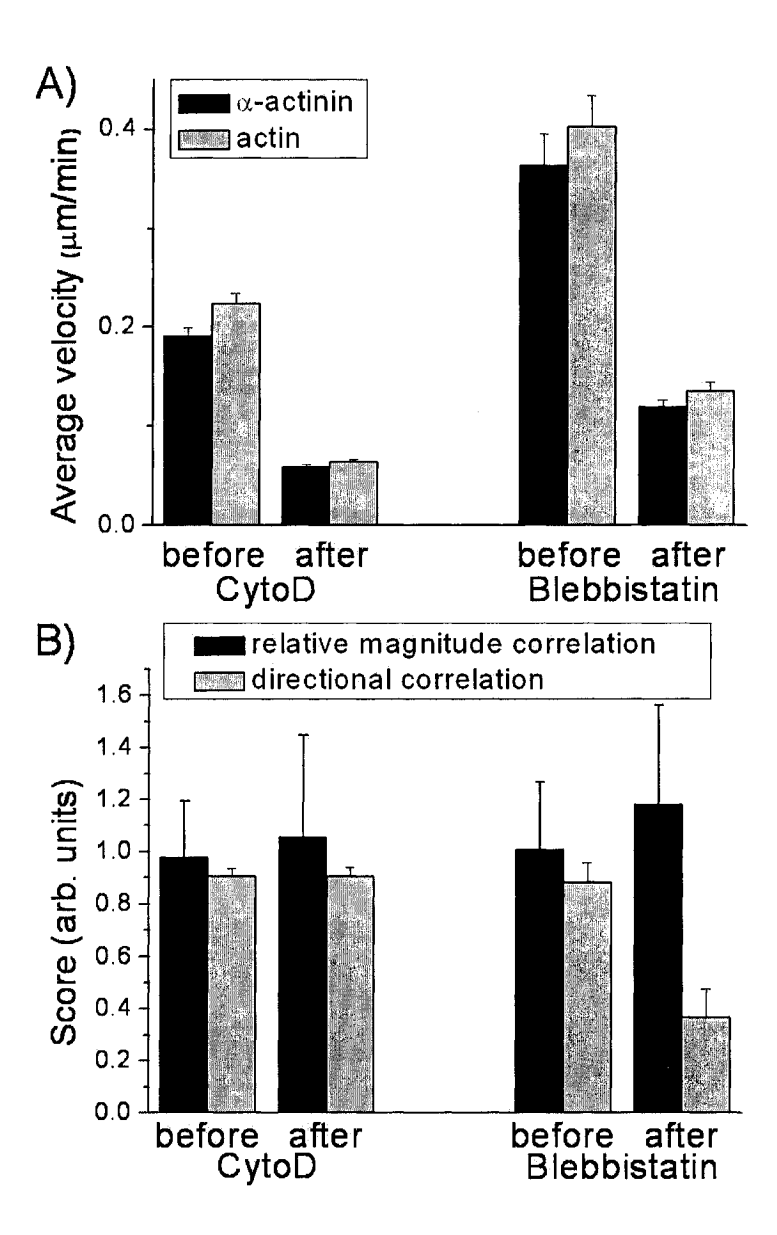


Figure 6.3: A) Average velocities before and after treatment with Cytochalasin D (200 nM) or Blebbistatin (50 μM) for α-actinin and actin (black and grey bars, respectively; error bars are SEM).

B). Relative magnitude and directional correlation coefficients for α-actinin and actin (black and grey bars, respectively) before and after treatment with Cytochalasin D and Blebbistatin.

To examine the role of actin filament contraction in the retrograde protein flow, the ATPase activity of non-muscle myosin II (a motor protein that drives retrograde movement of the actin filaments) was inhibited with blebbistatin [123]. Blebbistatin very rapidly inhibits the retrograde movement of actin and  $\alpha$ -actinin as shown by the STICS analysis. The average actin velocity decreased from  $0.36 \pm 0.03$  to  $0.12 \pm 0.01 \,\mu\text{m/min}$  and the average  $\alpha$ -actinin velocity from  $0.40 \pm 0.03$  to  $0.13 \pm 0.01 \,\mu\text{m/min}$ , again showing a reduction by a factor of 3 in each case (Figure 6.3A). However, in contrast to the cytoD treatment, the directional correlation coefficient between actin and  $\alpha$ -actinin was also significantly reduced across the lamella by the treatment with blebbistatin, decreasing from  $0.88 \pm 0.07$  to  $0.36 \pm 0.10$  (Figure 6.3B). A very small directional correlation coefficient implies that local flow vectors are not aligned in their directions and that the flow fields are decoupled. This suggests that the tension generated by myosin II is likely required to establish or maintain the coupling of actin and  $\alpha$ -actinin.

It is important to note that the image time series of actin and  $\alpha$ -actinin (Figure 6.2) had a very diffuse distribution of labeled proteins (as is often the case for CHO K1 cells plated under migration promoting conditions) with no visibly apparent labeled protein movement and no organized filamentous structures. With this type of protein expression, it would be virtually impossible to perform FSM or SPT, however, STICS analysis easily reveals an underlying directed motion of both proteins.

### 6.1.4 Correlated velocity of actin and adhesion proteins

To investigate the interactions of adhesion-associated molecules with the actin cytoskeleton during protrusion, we co-transfected cells with adhesion proteins labeled with green fluorescent protein (GFP) and actin-monomeric red fluorescent protein (mRFP) expressed at near endogenous levels. We ob-

served patterns of retrograde movement for  $\alpha$ 5-integrin, paxillin, FAK, talin, vinculin (Figure 6.4A-E),  $\alpha$ -actinin (see Figure 6.2, before treatment) and actin (Figure 6.4F-J) in the lamella of migrating cells. Integrin velocities were very slow throughout the lamella; its magnitude correlation relative to actin was only  $0.14 \pm 0.08$  and showed little association with the actin flow direction (directional correlation coefficient of  $0.3 \pm 0.5$ ) consistent with their tight engagement with the ECM (see Figures 6.4A and 6.5). Based on ICS analysis, more than 80% of the integrins were essentially stationary relative to the substrate (data not shown). This is in accord with our earlier measurements where we found the majority of  $\alpha$ 5-integrin to be immobile and supports the notion of a strong interaction with the substratum in the lamella of the cells [2].

STICS velocity measurements of the adhesion proteins were performed in regions of the lamella where there are extensive adhesions by using the immobile removal algorithm to filter out the spatial correlations due to the adhesion structures themselves (Figure 6.4B-E). In contrast to the integrin, the adhesion proteins paxillin (Figure 6.4B), FAK (Figure 6.4C), talin (Figure 6.4D) and vinculin (Figure 6.4E) were highly directionally correlated with the actin flow (Figure 6.4G-J) suggesting a direct or indirect interaction with actin. The adhesion proteins paxillin  $(0.67 \pm 0.06)$ , FAK  $(0.62 \pm 0.10)$ , talin  $(0.72 \pm 0.06)$  and vinculin  $(0.69 \pm 0.13)$  all have intermediate relative velocity magnitudes when compared to actin. On average the velocity of these proteins was approximately 2/3 that of the actin for every region of interest on the velocity maps (Figure 6.5). Relative velocities that are less than unity suggest that we are measuring an adhesion protein population

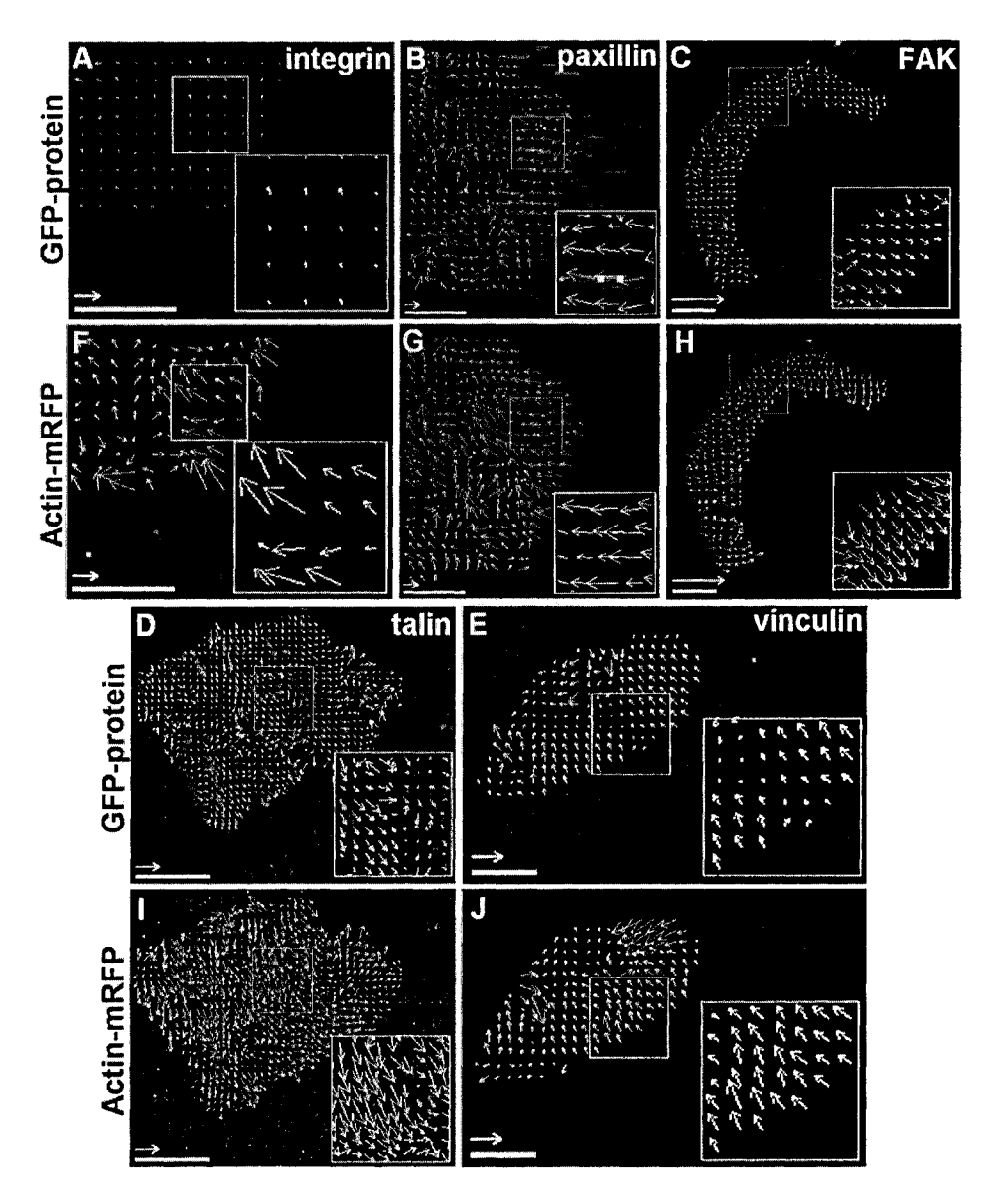


Figure 6.4: Dual detection channel protein STICS velocity maps for cells that were co-transfected with one type of adhesion protein-GFP and actin-mRFP and imaged by TIRM. Velocity maps of GFP conjugated A) integrin (121 frames, 10 s/frame), B) paxillin (121 frames, 5 s/frame), C) FAK (200 frames, 10 s/frame), D) talin (52 frames, 9 s/frame), E) vinculin (176 frames, 10 s/frame), and the corresponding actin-mRFP velocity maps (F-J). Insets are a 2× expansions of the small white box in each image. Spatial scale bars are 5 μm, velocity scale vectors are 1 μm/min.

that is transiently binding and unbinding to the actin. We are effectively averaging over the actin bound and unbound states of the adhesion protein, with the bound protein moving at the same speed as actin (for 70% of the measurement time) and the unbound protein immobile (for 30% of the measurement time). In this situation, averaging over the bound and unbound populations gives a lower apparent velocity correlation with actin. It is important to note that we are able to measure transient binding in this manner because the immobile removal algorithm only filters out contributions from fluorescent components that do not move throughout the entire duration of the image time series analyzed.

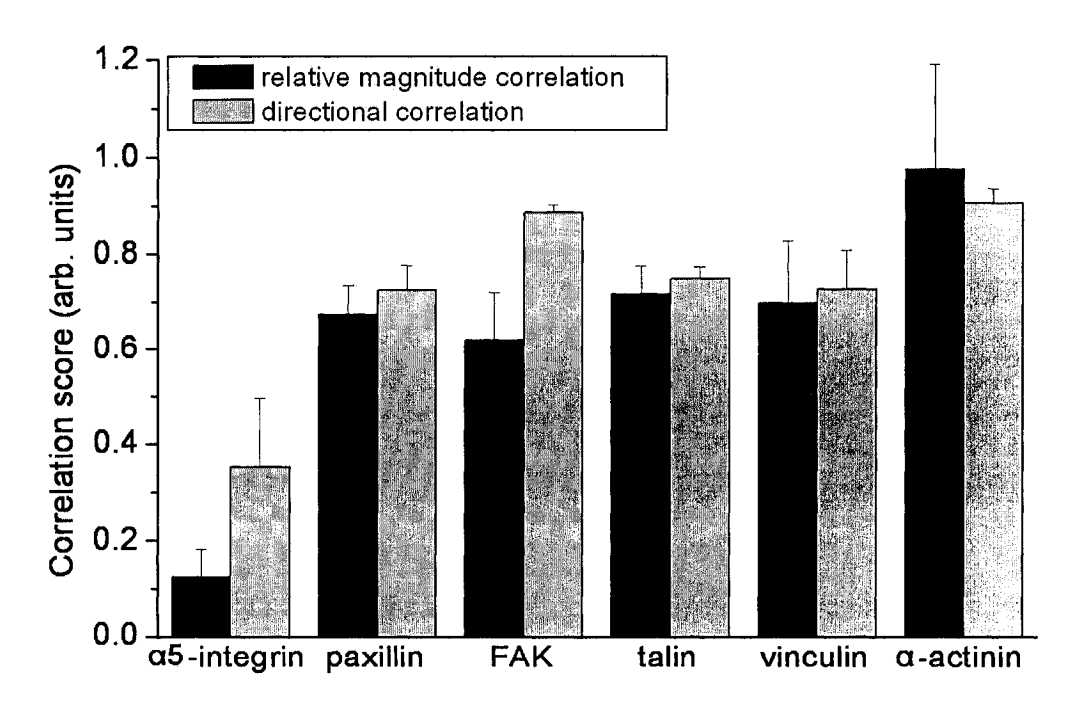


Figure 6.5: Relative magnitude and directional correlation coefficients for the actin/adhesion protein pairs studied by STICS analysis.

The velocities of  $\alpha$ -actinin were the most uniformly and highly correlated with those of actin. These two proteins had nearly identical velocity maps, with a relative magnitude correlation coefficient of  $1.0 \pm 0.2$  and a directional correlation of  $0.91 \pm 0.03$  (Figure 6.5) which is consistent with the tight coupling of  $\alpha$ -actinin to actin as a bundling protein. Nevertheless, to our knowledge this is the first time a correlated velocity between  $\alpha$ -actinin and actin has been observed and quantified in situ.

For paxillin it is interesting to note that the flow vectors correlate highly with the  $\alpha$ -actinin flow direction in regions where there are adhesions (see Figure 6.6), while in other areas of the lamella, its movement is not directionally correlated with  $\alpha$ -actinin and shows vectors pointing in multiple directions. The large randomly oriented white vectors shown in the left part of the lamella for paxillin (see Figure 6.6B) are artifacts and are observed in cases where there is no directed protein motion. In such cases, we are able to distinguish these noise artifacts from vectors due to real protein flows by visual inspection as we can see when the best fit Gaussian peak jumps to a low amplitude background correlation noise peak. Moreover, the directional correlation between  $\alpha$ -actinin and paxillin was  $0.85 \pm 0.03$  and the relative magnitude was  $0.79 \pm 0.10$ , which are similar to actin-paxillin correlation scores. This is expected since  $\alpha$ -actinin and actin are highly correlated. These observations suggest that the directed movement of paxillin is due to its association with actin through  $\alpha$ -actinin, as part of the linkage complex. At the rear of the lamella there is little evidence for directed motion of the adhesion proteins, which is consistent with the reduced number of adhesions and disassembly of actin filaments in this region of the cell (Figure 6.6). The

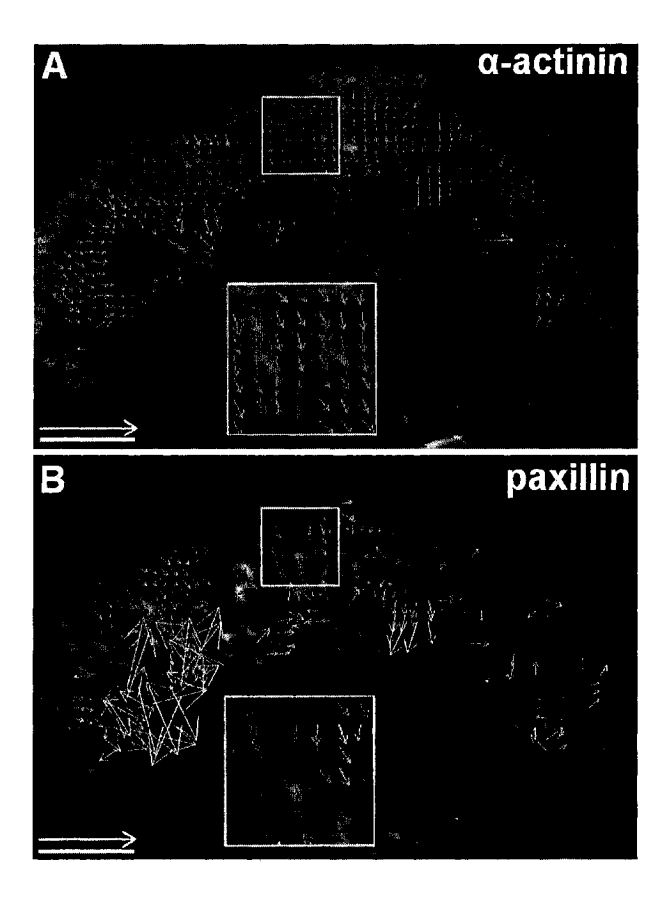


Figure 6.6: Dual detection channel STICS velocity maps for a CHO cell co-transfected with  $\alpha$ -actinin-GFP (A) and paxillin-DsRed (B) and imaged by TIRM (100 frames, 15 s/frame). The large randomly oriented white vectors in the lower left part of the lamella for paxillin are fitting artifacts for cases where there is no detectable protein transport. They appear throughout the rear of the lamella, where there are fewer adhesions and actin filaments are disassembling. Insets are  $2\times$  expansions of the small white boxes in each image. Spatial scale bar is  $5 \mu m$ , velocity scale vector is  $5 \mu m/min$ .

flow maps are also less homogeneous towards the rear of the lamella where there are many more velocity vectors pointing in variable directions. This can be seen for both talin and vinculin with some arrows actually pointing towards the leading edge of the cell (Figure 6.4D, 6.4E).

#### 6.1.5 Discussion

Regulation of the linkage between the ECM and the actin cytoskeleton is critical for cell migration. The linkage is important for regulating the rate of protrusion, protrusion stability and retraction. In addition, the linkage plays a role in adhesion assembly, growth, turnover and the signaling of adhesions by coupling myosin mediated actin filament contraction to adhesions [89, 124, 125]. In this study we have addressed the efficiency of the ECM-actin linkage and identified potential points of regulation. To address the nature of the linkage we have applied our new image correlation method: STICS. Flow velocities for a number of adhesion components ( $\alpha$ 5-integrin,  $\alpha$ -actinin, paxillin, FAK, talin and vinculin) were compared with those of actin to identify which proteins within the linkage are potential sites of regulation via transient decoupling or slippage.

Previous studies have pointed to integrins as the link between the substratum and cytoplasmic adhesion components making the binding between integrin and adhesion components a potential site of decoupling or slippage with actin [111, 112, 114]. At the rear of the cell the strength of integrin binding to the substratum depends on the affinity of the integrin to the ECM, the concentration of fibronectin on the substratum, and the number of integrin receptors [111, 112, 114]. The studies presented here show that the binding of integrin to the substratum is also strong in the lamella of migrating cells where upwards of 80% of the integrin is immobile.

While the integrin movement is not tightly coupled to actin, all four other adhesion components studied here: paxillin, FAK, talin and vinculin

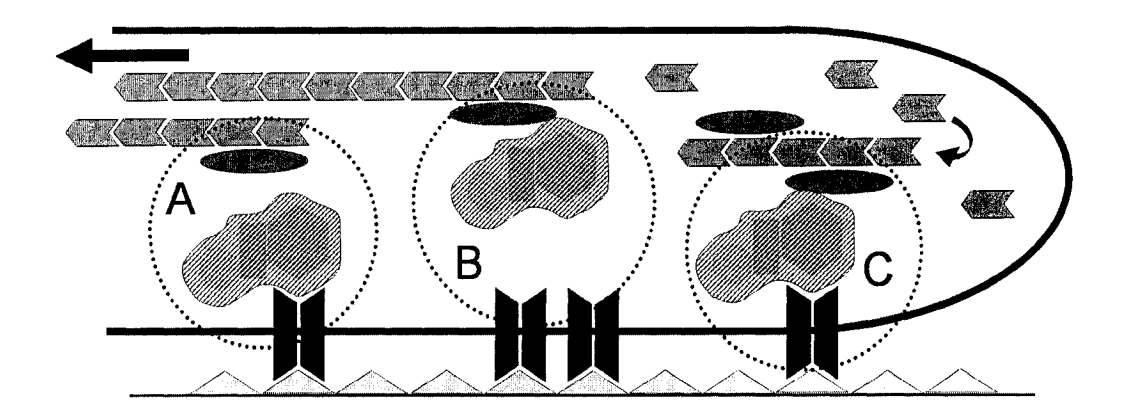


Figure 6.7: Diagramatic model of a protruding lamella illustrating how differential retrograde motion of actin and adhesion proteins can occur by a two-level linkage mechanism. The actin (stippled chevrons) and α-actinin (ovals) are always concomitant. Slippage occurs either A) proximal to α-actinin through its interaction with one of the components of the linkage complex (shaded molecules), or B) proximal to the integrins (trapezoid dimers) perhaps at the talin-integrin linkage. C) Protrusion and cell body translocation can occur through polymerization generated forces and myosin II contraction when both levels of the adhesion complex are engaged.

are. This suggests that there is a significant disconnect between integrin and the cytoplasmic adhesion components. The very similar coupling to actin shown by all four adhesion proteins implies that they all reside in a common complex, likely including additional adhesion proteins, which is more tightly associated with actin than integrin. These adhesion proteins show velocities that are 70% as large as actin suggesting that the linkage complex is bound to actin 70% of the time and to immobilized integrin 30% of the time. Thus, the ECM-actin linkage appears to be regulated at two levels: between the adhesion complex and integrin and between the adhesion complex and actin (see Figure 6.7).

On the first level, there are many potential proteins that link integrin to the actin cytoskeleton, however talin is emerging as a major player in cell motility [126], so it is a likely candidate for a point of slippage, or disconnect. Its presence is essential for force generation [127], integrin activation [128], and the stability of junctions [129]. Although the integrin-talin interaction is relatively weak, it may be highly regulated [130], and many weak interactions may be easier to regulate than a few strong bonds.

On the second level, the binding of the adhesion complex with actin may be regulated via the interaction between  $\alpha$ -actinin and one of its binding partners. Several studies point to  $\alpha$ -actinin as a key protein in tension sensing by adhesions. Studies suggest that the incorporation of  $\alpha$ -actinin into adhesions occurs late in their assembly and the incorporation is coincident with the onset of their retrograde movement, or sliding, when the adhesions are presumably under higher tension [100, 131]. In a similar vein, force dependent strengthening of integrin-cytoskeleton linkages correlates with the incorporation of  $\alpha$ -actinin into adhesions and this incorporation is regulated by FAK dependent phosphorylation on Y12 of  $\alpha$ -actinin [100, 132]. The potential role of  $\alpha$ -actinin in tension sensing, the fact that it is known to bind both vinculin and talin, and the fact that vinculin and talin are thought to comprise a structural linkage between integrin and actin [133, 134] all make  $\alpha$ -actinin a likely candidate for regulation of the ECM actin linkage via its binding to the linkage complex.

It is interesting that the directional correlation of actin and  $\alpha$ -actinin is significantly reduced by inhibition of myosin II activity with blebbistatin.

One possibility is that tension generated by myosin II regulates  $\alpha$ -actininactin binding through tension induced effects on the organization of actin within filaments. Alternatively, it may affect actin organization directly because of a weakened affinity of myosin II for actin, when cells are treated with blebbistatin [135, 136].

These measurements are significant as they represent the first experimental approaches that attempt to discern the nature of the adhesion complex in living cells. These results represent an important application of STICS to a highly significant problem in cell biology and demonstrate the power of quantitative biophysical measurements *in situ*. In the next section, STICS is applied to a different live cell application: mapping fluid flow in migrating keratocytes.

## 6.2 Fluid Flow in Fish Keratocyte

#### 6.2.1 Fluid Flow in Cells

Indirect observations [137, 138, 139] have suggested that fluid intake through aquaporin channels at the leading edge might play an important role in cell motility. The hydrodynamic forces they induce could oppose membrane load and help actin polymerization, and they might influence transport of components of the actin machinery to the leading edge [140]. Cytosolic fluid flow has been well-studied in many systems such as plant cells or amoebae [141] where velocities range from 10 nm/s to 100  $\mu$ m/s. Current techniques for measuring flow in these cells involve imaging and following large organelles

inside the cell, but they are inadequate for measuring fluid flow in cells that have a dense actin meshwork.

In collaboration with the Theriot lab at Stanford University, we devised a technique for measuring fluid flow in the lamella of migrating cells by incorporating fluorescent tracers in the cytosol, imaging and then performing STICS analysis. A requirement for these tracers is that they have minimal non-specific interactions with the actin meshwork or other components of the cytoplasm, in order for their motion to reflect the fluid flow. We chose two sizes of methoxy-polyethylene-glycol (PEG) coated quantum dots (PEG QDs; 655QDs and 545QDs with a diameter of 30.7 nm and 24.5 nm respectively) and green fluorescent protein (GFP, ~4×3 nm L×W) as tracers. The PEG coating on the QDs helps in reducing non-specific interactions both in-vivo [42, 142], and in in-vitro actin networks [143]. It is interesting to note that the measured flow should be independent of tracer size because the Reynolds number is very low at this size scale so all flow is laminar. In such cases, viscous friction dominates and the particles are simply carried by the flow.

### 6.2.2 Fluid Flow Patterns in Keratocytes

Flows were measured by electroporating a high concentration of PEG coated quantum dots in fish keratocytes and imaging those using wide field fluorescence microscopy followed by STICS analysis. Fish keratocytes present a very nice system for the study of cytosolic fluid dynamics in migrating cells. The cell motion is smooth and persistent with almost no change in shape [5, 6], which makes it easy to define a cell frame of reference, and perform analysis in this reference frame. The large and thin ( $\sim$ 40  $\mu$ m  $\times$  200 nm)

lamella of moving keratocytes is an ideal substrate for the two dimensional STICS analysis. Also the essential macromolecular components of the cell motility machinery are present in keratocytes, with distributions and functions similar to other cells [144, 145]. Additionally all of these characteristics make this system particularly amenable to biophysical modeling.

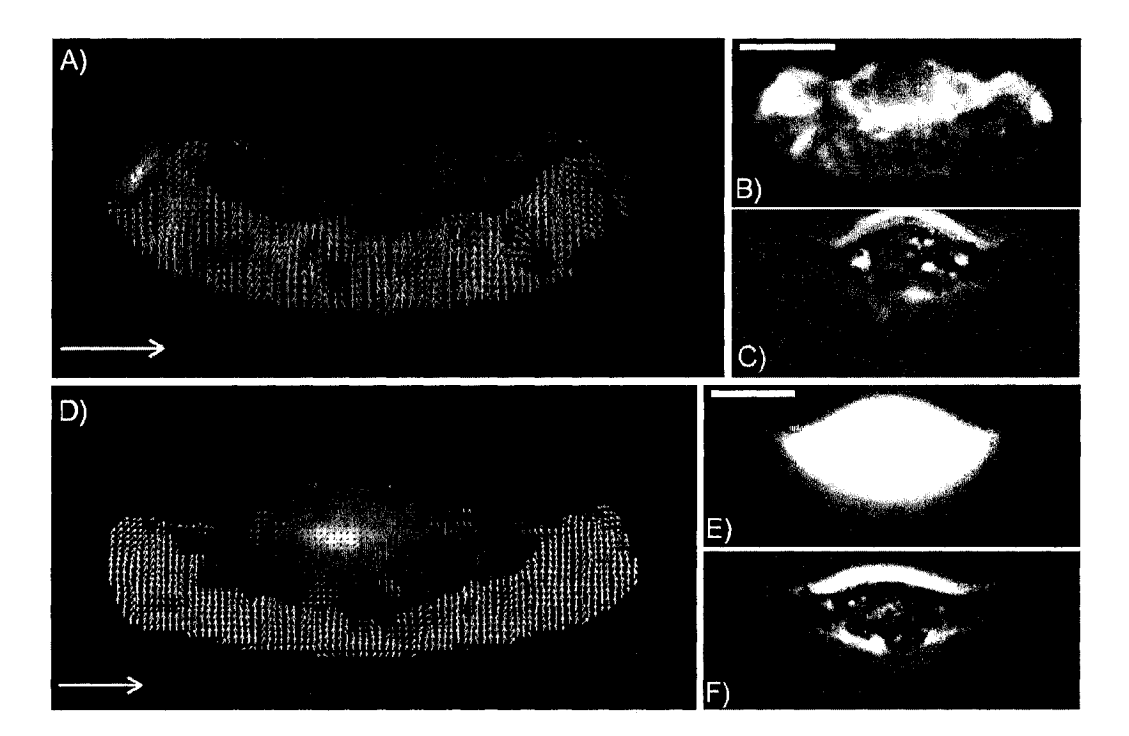


Figure 6.8: STICS velocity map measurements of flow for A) 545 QDs and D) GFP. Panels B) and E) show the fluorescence image; while panels C) and F) show the phase contrast microscopy image. Images are oriented so that all cells are moving downward. Measurements were performed by STICS in the cell frame of reference. Each arrow corresponds to the average flow vector in a 1.8×1.8 μm² region around its center. The magnitude of the flow is indicated by both its size and color. The cell migration speeds are: 0.20 μm/s, 0.14 μm/s for A) and D) respectively. The spatial scale bars are 10 μm, the velocity scale vectors (on A and D) are 1 μm/s.

We performed fluorescence microscopy imaging and then carried out STICS analysis on many regions of the keratocyte lamella to generate velocity maps as shown in Figure 6.8. We found that several general features stood out. In all cells observed (N=59) there was an approximately constant rearward fluid flow away from the leading edge, opposite to the direction of movement with a magnitude that was approximately  $34 \pm 20\%$  of the cell migration speed (Figure 6.9; note that in the lab frame of reference this translates to a net forward flow at  $66 \pm 20\%$  of the cell migration speed). The fluid flow in the end lobes of the cell was usually slower, and exhibited correlation with the angular motion in turning cells. The lobe that was most distant from the center of rotation of the cell exhibited larger retrograde flows, consistent with the interpretation of fluid intake since this lobe is also moving faster (being further away from the center of rotation). We also found there was a correlation between the perpendicular fluid flow and the rotation speed of the cell (Figure 6.10). As the cell is rotating one way, the fluid lags behind, so that in the cell frame of reference we observed a perpendicular fluid flow in the opposite direction.

Moreover, we found that there was no dependence of the measured velocity for fluid flow on the fluorescent tracer size. Independent fits showed that the retrograde flow velocity dependence on the cell speed was the same for the 655 PEG QDs (0.37  $\pm$  12%) and 545 PEG QDs (0.31  $\pm$  23%), and for GFP (0.31  $\pm$  22%) which is almost an order of magnitude smaller in size (see Figure 6.9). This is further evidence that we are indeed measuring fluid flow, and that interactions with the cytoskeleton are an unlikely cause of the

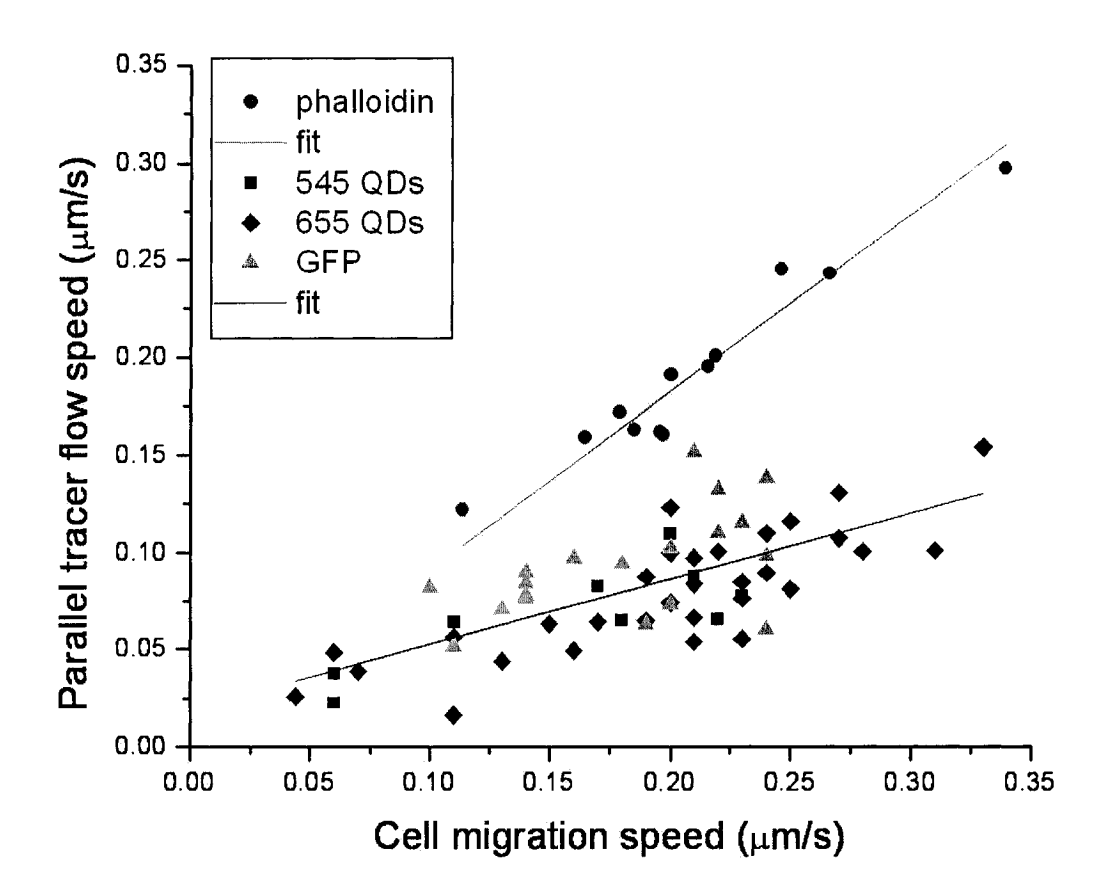


Figure 6.9: STICS was used to measure tracer flow in the cell frame of reference for a population of migrating cells. The flow speed parallel to the direction of cell motion, averaged over the front region of the lamella, is shown for: 655QDs (diamonds, N=31 cells), 545QDs (squares, N=9 cells) and GFP (triangles, N=19 cells), as a function of cell speed. The linear regression fit line corresponds to  $V_{parallel} = 0.34 \times V_{cell} + 0.019$  ( $R^2 = 0.5$ ). The F-actin meshwork flow speeds measured from phalloidin labeled actin (circles, N=12 cells) are shown for comparison ( $V_{parallel} = 0.84 \times V_{cell} + 0.017$ ,  $R^2 = 0.94$ ).

retrograde flow because we would expect this type of interaction to be size and surface chemistry dependent, and would predict a greater velocity for the smaller GFP molecules if this were the case.

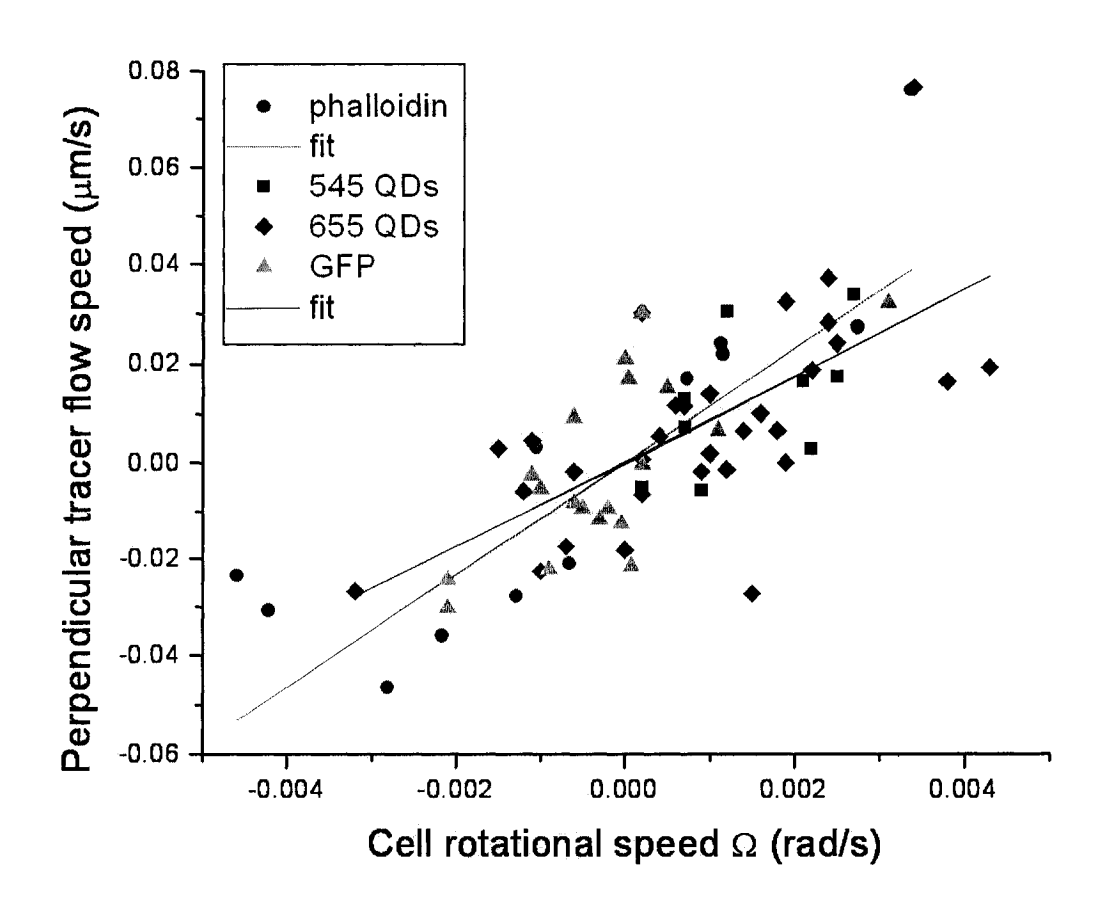


Figure 6.10: STICS was used to measure tracer flow in the cell frame of reference for a population of migrating cells. The flow speed perpendicular to the direction of cell motion, averaged over the front region of the lamella, is shown for: 655QDs (diamonds, N=31 cells), 545QDs (squares, N=9 cells) and GFP (triangles, N=19 cells), as a function of cell speed. The fit line corresponds to  $V_{perpendicular} = 9 \pm 4\mu m/rad \times \Omega$  ( $R^2 = 0.46$ ) where  $\Omega$  is the cell rotational speed. The F-actin meshwork flow (circles, N=12 cells) is shown for comparison ( $V_{perpendicular} = 11 \pm 5\mu m/rad \times \Omega$ ,  $R^2 = 0.73$ ).

We further applied the STICS analysis to generate velocity maps of phalloidin labeled actin filaments. The maps were qualitatively and quantitatively different from the the fluid flow tracer maps within the same cell type. The actin retrograde flow was faster and, as expected, approximately equaled the cell speed [146]. The actin flow pattern was much more coherent and

showed less spatial variations. Taken together, all of these results suggest that the quantum dot or GFP tracer flow measured by STICS reflects the fluid flow in the lamella.

### 6.2.3 Active Flow Model

To account for these results, we collaborated with Prof. Alex Mogilner, a theoretical physicist at UC Davis studying theoretical aspects of cell motility [6, 7, 147, 148, 149]. He developed a simple physical model describing the behavior of the cytosolic fluid in a moving cell along the anterior-posterior direction (Figure 6.11), which accounts for our experimental measurements. The model assumes that actin dependent cell protrusion at the leading edge is limited by membrane resistance, and that the osmotic pressure,  $P_{osm}$ , at the leading edge contributes to the protrusion force. Let  $V_p$  be the actin polymerization speed,  $V_r$  the speed of actin retrograde flow in the lab frame of reference, and  $V_{cell} = V_p - V_r$ , the cell speed. The rate of actin polymerization is slowed by membrane resistance and can be approximately characterized by the following linear force-velocity relation:

$$V_p = V_0 \left( 1 - \frac{P_r - P_{osm}}{P_r^{stall}} \right) \tag{6.1}$$

where  $V_0$  is the free polymerization rate,  $P_r$  is the pressure of the membrane resistance, and  $P_r^{stall}$  is the pressure required to stall protrusion at the leading edge. We further assume that permeability of the membrane is concentrated at the leading edge of the cell, so that the fluid inflow rate is proportional to the pressure difference between the actual osmotic pressure at the leading edge  $P_{osm}$ , and  $P_{osm}^{eq}$ , a constant model parameter defined as the equilibrium

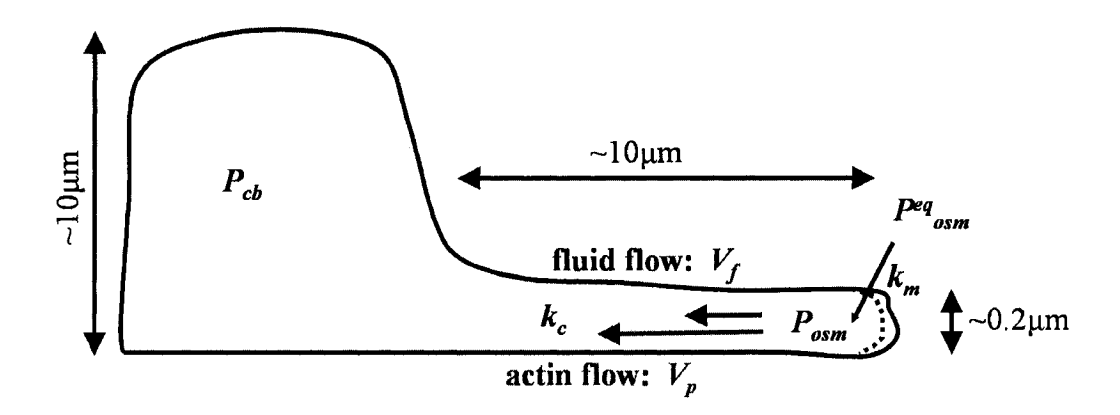


Figure 6.11: A diagramatic physical model showing a cross section of a moving keratocyte in the cell frame of reference. The direction of cell movement is to the right, with the large cell body in the back and a thin lamella at the front. The actin meshwork exhibits retrograde flow (red arrow) with a speed approximately equal to the cell speed. The fluid flow exhibits substantially slower retrograde flow (blue arrow) accompanied by a pressure gradient across the lamella, with P being the pressure at the leading edge and  $P_{cb}$  the pressure in the cell body. The effective pressure difference across the membrane is equal to  $P_{osm}^{eq} - P_{osm}$ . The parameters  $k_m$  and  $k_c$  denote the permeability of the membrane at the leading edge, and the permeability of the actin meshwork, respectively. Model developed by Prof. Alex Mogilner (UC Davis).

osmotic pressure at the leading edge at which the water influx would be zero. With the membrane permeability,  $k_m$  (in units of  $\mu m^3/pN \cdot s$ ), as the proportionality constant [138, 150], the speed of fluid flow into the cell,  $V_f$ , is given by:

$$V_f = k_m (P_{osm}^{eq} - P_{osm}) \tag{6.2}$$

The velocity difference between the actin cytoskeleton and the fluid phase,  $V_p - V_f$ , is proportional to the pressure gradient between the cell body and

the leading edge. This is characterized by the D'Arcy flow equation:

$$V_p - V_f = k' \frac{(P_{cb} - P_{osm})}{L} \tag{6.3}$$

where k' is the hydraulic permeability [138, 150] of the meshwork,  $P_{cb}$  is the pressure in the cell body, and L is the lamellipodial length.

The three equations 6.1, 6.2 and 6.3 constitute a linear system for three unknown variables,  $V_p$ ,  $V_f$  and  $P_{osm}$  as functions of the model parameters  $V_0$ ,  $P_r$ ,  $P_r^{stall}$ ,  $P_{osm}$ ,  $k_m$ ,  $P_{cb}$  and  $k_c = k'/L$ . The solution of this system is consistent with our experimental measurements of fluid flow as a function of cell speed under the assumption that the observed cell-to-cell speed variation is due to variation in the model parameters  $V_0$ ,  $P_r^{stall}$  and  $P_r$ , i.e. it is due to variations in the polymerization rates and membrane resistance between different cells. In this case we obtain the following simple relation:

$$V_f \alpha \frac{k_m}{k_m + k_c} V_{cell} \tag{6.4}$$

which implies that the fluid flow rate is linearly proportional to the observed cell speed, with a proportionality coefficient less than 1. This is in excellent agreement with the data (Figure 6.9). Estimates of the membrane and hydraulic permeabilities ( $k_c \sim 10^{-4} \ \mu m^3/pN \cdot s$  and  $k_m \sim 10^{-4} \ \mu m^3/pN \cdot s$ , see [151]) show that they are of the same order of magnitude, which is consistent with the experimentally measured slope of  $\sim 0.34$  for the linear fits (for which we would need  $k_c \approx 2k_m$ ).

## 6.3 Chapter Conclusion

In this chapter we have applied STICS to study two very different biological systems of interest for cell migration. First, we generated retrograde velocity maps of several adhesion related proteins labeled with GFP and actin-mRFP. We found that the integrins were essentially fixed to the substrate, whereas  $\alpha$ -actinin was always bound to actin and flowed in a retrograde manner that correlated with the actin flow. In between these two extremes lie a group of structural and signalling molecules (FAK, paxillin, vinculin and talin) which have approximately 70% correlation in magnitude and direction with the actin flow. Thus the STICS measurements suggest that these adhesion proteins are part of a linkage complex that dynamically regulates the interactions between the integrins and the actin cytoskeleton. These experiments point to a two level molecular clutch mechanism where the linkage is probably regulated between the integrins and the linkage complex at the talin level, and between the  $\alpha$ -actinin and the linkage complex. Although the molecular clutch hypothesis was first proposed more than a decade ago [109], our measurements represent the first attempts to measure the dynamic aspects of its regulation in situ.

We also applied STICS to the unresolved problem of fluid flow in migrating cells. By introducing various tracer particles (quantum dots or GFP) in the cytosol of moving keratocytes, we were able to map the retrograde flow of fluid in the lamella. The flow was found to be independent of tracer size as expected, and was always approximately 1/3 of cell migration speed, which is in accord with a biophysical model developed by Prof. Alex Mogilner (UC

Davis). Retrograde fluid flow maps of phalloidin-labeled actin showed much faster flow, which were on the order of the cell speed. This is expected [146] and shows a significant difference from our tracer results suggesting that the quantum dot or GFP tracer flow measured by STICS truly reflects the fluid flow in the lamella. These measurements indicate that fluid flow does play a role in cell migration for keratocytes by alleviating the membrane load at the leading edge and favoring actin polymerization, and answers a decades old question by elegant application of quantitative biophysical measurements in living cells.

#### 7 Conclusion and Outlook

Fluorescence microscopy has emerged as a versatile and productive tool in biophysics, most importantly for in vivo studies of living cells. Imaging by confocal, two-photon LSM or TIRM enables direct observation of proteins in their native cellular environment. Applications range from qualitative localization of proteins within the cell to quantitative dynamic studies by SPT or correlation analysis of the image time series. Most of the existing velocity measurement techniques are limited for applications involving determination of protein flow velocities in living cells (Chapter 1). To address this need, we developed STICS as an extension of the intensity fluctuation correlation family of biophysical analysis methods (Chapter 2). By spatio-temporal correlation analysis of intensity fluctuations in fluorescence microscopy image time series, STICS combines the directional information imbedded in the two dimensional spatial correlations with the time dependent transport measured by the temporal correlation. However, in the presence of a large immobile population fraction, the STICS analysis will be dominated by the intensity contribution from the static population. A filtering algorithm was devised which removes the intensity contribution of the immobile species (Chapter 2) by filtering the zero (or low) frequency components in reciprocal space, for every pixel trace in time before running the space-time correlation analysis.

The advantage of the STICS method is the extensive averaging that is done over all pairs of images in the time series analyzed. This allows mapping of velocities even in cells with very low densities of labeled proteins, low signal to noise ratio and with relatively short temporal sampling (Chapter 4). Computer simulations have shown that situations in which the fluorescent molecules photobleach do not significantly affect the STICS analysis, provided that the time scale for bleaching is not much shorter than the characteristic flow time of the particles. The simulations also revealed that STICS is able to perform very well even in poor imaging conditions where the signal to noise ratio is as low as 1, provided that the number of frames is large enough to allow sufficient averaging. The dynamic range of the immobile filtering algorithm was investigated under varying conditions of signal to noise, number of frames sampled and the fraction of the population that is immobile. From these simulations, it was shown that the immobile filtering is best applied when particles move at least one full beam focus diameter during the time of the experiment, thus allowing full relaxation of the dynamic flow process over this time scale. Moreover, removing the immobile and low frequency components in the intensity trace for every pixel using the window filtering algorithm can get rid of slow variations in intensity from unwanted sources without affecting the results of the STICS analysis.

As a final step for characterization of the new method, the STICS analysis was applied in vivo (Chapter 5). We imaged  $\alpha$ -actinin, which organizes along actin filaments in spatially extended structures that perturb the STICS analysis. The immobile filtering algorithm was successful in removing these dominant spatial correlations due to the immobile population, allowing us to map  $\alpha$ -actinin velocities across the lamella in living CHO cells. By analyzing typical cases of diffusion, flow in random directions and concerted flow in vivo, we have further shown that the combination of ICS and STICS can distinguish between these cases, because ICS is sensitive to flow speed irre-

161

spective of particle direction while STICS measures a net resultant velocity vector for the flowing molecules present. The cross-correlation application of STICCS to fluorescent microsphere samples demonstrated the ability of this method to recover protein flow magnitude and direction for both interacting and non-interacting populations, provided the interacting population remains coupled for the duration of the experiment. However, the more general case of the varying protein interactions (where proteins bind and unbind repeatedly), can be treated by analyzing the relative velocity magnitudes at every point in the velocity maps for the two species.

STICS was then applied to the problem of cell migration, which is regulated by several processes involving many different transmembrane, cytosolic and cytoskeletal proteins (Chapter 6). By applying STICS to map out the relative retrograde flow magnitudes of several adhesion related molecules and actin, we were able to identify a complex linking the transmembrane integrins to actin. The integrins were stationary relative to the substrate as expected [2]. On the other hand,  $\alpha$ -actinin was found to be entirely associated with actin, consistent with the tight coupling of  $\alpha$ -actinin to actin as a bundling protein. The protein complex was found to comprise structural proteins such as talin and vinculin, as well as signalling molecules such as paxillin and FAK. We found that the linkage complex is bound to actin 70% of the time and to immobilized integrin 30% of the time. The ECM-actin linkage appears to be regulated at two points of labile linkage: one proximal to the integrins, one proximal to the  $\alpha$ -actinin. Furthermore, perturbation of the actin polymerization using Cytochalasin D did not affect the relative magnitude and directional correlation of  $\alpha$ -actinin, indicating that polymerization does

not play a significant role in regulating the integrin-actin linkage. However, inhibition of myosin II using blebbistatin significantly reduced the coupling between the  $\alpha$ -actinin and actin flows. This might be because the tension generated by myosin II regulates  $\alpha$ -actinin-actin binding through tension induced effects on the organization of actin within filaments. Interestingly,  $\alpha$ -actinin is present only in adhesions that are under tension and this binding is regulated by a FAK dependent tyrosine phosphorylation of  $\alpha$ -actinin [100, 132].

Finally, we used STICS to look at fluid flow in the lamella of epidermal fish keratocytes, which are amongst the fastest migrating cells (Chapter 6). We introduced different fluorescent tracer particles, like PEG coated quantum dots or GFP, in the cytosol of migrating keratocytes and imaged them. Using STICS, we obtained maps of retrograde fluid flow in the lamella of these migrating cells. The flow was found to be independent of tracer size as expected for fluid flow, and the fluid flow speed was always approximately 1/3 of cell migration speed, which is in accord with a model developed by Prof. Alex Mogilner at UC Davis. Moreover, fluid flow maps of phalloidinlabeled actin showed faster retrograde velocities for the cytoskeleton, on the order of the cell speed, which is expected [146] and which are significantly different from the tracer speeds. Taken together, this data suggests that the quantum dot or GFP tracer flow measured by STICS reflects the fluid flow in the lamella. This answers a long standing question about the role of fluid flow in keratocyte migration, as we have demonstrated that fluid flow at the leading edge alleviates the membrane load and favors actin polymerization.

163

Other velocity mapping techniques, such as fluorescent speckle microscopy, have been successful at extracting actin and tubulin flow velocities by tracking single speckles of labeled subunits inside the filaments. The wealth of information on cytoskeletal dynamics provided by speckle microscopy is, however, limited to applications on only actin and tubulin. The STICS technique, on the other hand, has the advantage that it can be applied in a matter of minutes to virtually any fluorescence microscope image time series, to cells that are simply transfected with any type of fluorescently labeled molecule (not just cytoskeletal proteins). It does not require any overly sophisticated sample preparation or imaging instrumentation (such as the specialized labeling needed for FSM). The technique has high resolution, and most importantly it can measure protein motions either at high protein densities, such as in adhesions or along actin filaments, or at very low homogenous protein densities when there are no obvious resolvable structures to track (such as with SPT). In summary, the STICS method is a versatile tool that can be used in many different situations, from protein dynamics to fluid flow, where quantitative information on directed protein motion within the cell is required.

Image correlation techniques have been applied for a decade in various biological systems of interest. Several avenues of possible research open up by combining the STICS analysis with other biophysical approaches. For example, one could use patterned substrates of ECM protein gradients to direct cellular migration, or look at the effect of ECM protein distribution on the adhesion protein interactions and recruitment. One could also use microfluidic devices to deliver drugs quickly and reversibly to migrating cells, and look at

their effect on retrograde flow and protein interactions. Several extensions and refinements to the STICS technique will be needed, particularly ways to improve the temporal resolution (i.e. faster imaging approaches). The results presented in this thesis show that STICS is a powerful method that can be applied in living cells to solve certain problems that require quantitative measurements of protein velocities. As such, it represents a significant contribution to those who toil in the biophysical community seeking to properly arrange the pieces of the puzzle that is life.

## 8 Appendix A: Biohazard Certificate

## McGill University



## APPLICATION TO USE BIOHAZARDOUS MATERIALS'



Projects involving potentially biohazardous materials should not be commenced without approval from the Environmental Safety Office. Submit applications before 1) starting new projects, 2) renewing existing projects, or 3) changing the nature of the biohazardous materials within existing projects.

1. PRINCIPAL INVESTIGATOR: Prof. Paul W. Wiseman	PHONE:	x5354	
DEPARTMENT: Chemistry & Physics	FAX:	x3797	
Dept. of Chemistry 801 Sherbrooke St. West ADDRESS: Montreal, QC H3A 2K6 E-	MAIL: paul.wisc	man@monill ca	
PROJECT TITLE:Image correlation spectroscopy studies of the clustering a	and transport of me	mbrabe receptor	proteins in
living cells. Nanotools for Neuropharmacology, Improved femtosecond lase	er approaches for e		
Probing Synaptic Remodeling with Quantum Dots and Image Correlation S	pectroscopy		
2 ISMED CENTRY Demonstry Assistant of the Assistant of th			
EMERGENCY: Person(s) designated to handle emergencies     Name: Paul Wiseman Phone No: work: (5)	14) 308-5354	home: (514)	487-1783
Name: Phone No: work:	14) 555-555	home:	
I hope ito, work		ijoine.	
NSERC HF	SP NCE	CIHR	
3. FUNDING SOURCE OR AGENCY (specify):		<del></del>	
Grant No.: Not assigned yet Beginning date: April 1, 2004	End date:	March 31, 2	009
Renewal; procedures previously approved without alterations.  Approval End Date:  New funding source: project previously reviewed and approved under an Agency:  Approval End Date:  New project: project not previously reviewed.  Approved project: change in biohazardous materials or procedures.  Work/project involving biohazardous materials in teaching/diagnostics.	azard Application to ano	ther agency O	CELL LINE R OTHER IEWED DETA
CERTIFICATION STATEMENT: The Environmental Safety Office approve certifies with the applicant that the experiment will be in accordance with the "Laboratory Biosafety Guidelines" and in the "McGill Laboratory Biosafety I Containment Level (select one): 1 2 2 2 2 with additional property of the containment Level (select one): 1 2 2 2 3 2 3 2 3 3 2 3 3 3 3 3 3 3 3 3	principles outlined Manual".		
$\mathcal{L}$		7C 11	2006
Principal Investigator or course director:	date:	28 4 <del>                                      </del>	ycer
Approved by: Environmental Safety Office:	date:	28 04 mouth	05
MONATURE		•	A O
	exbita:	31 03 month	<u>```</u> ,;;;
			ű

"as defined in the "McCill Laboratory Biossfery Manual"

514 398 8047

Name	Department	Job Title/Classification	Attended Safe Use of Biological Safety Cabinets seminar? If yes, indicate date of attendance
Ben Hebert	Physics	Graduate Student	Yes May 19, 2004
Santiago Costantino	Physics	Postdoctoral Fellow	Yes May 19, 2004
Nela Durisic	Physics	Graduate Student	Yes May, 2003
David Kolln	Chemistry	Graduate Student	Yes May 19, 2004

#### 6. Briefly describe:

i) the biohazardous material involved (e.g. bacteria, viruses, human tissues, toxins of biological origin) & designated biosafety risk group

Cell Cultures, Standard fibroblast and fibroblast like cell lines NIH-3T3, CHO, MEF, AG1523 and GFP transfectants of these

ii) the procedures involving biohazards
Standard tissue culture protocols, biological safety cabinet, incubator, separate tissue culture room in the laboratory

iii) the protocol for decontaminating spills Bleach

7. Does the protocol present conditions (e.g. handling of large volumes or high concentrations of pathogens) that could increase the hazards?

No

8. Do the specific procedures to be employed involving genetically engineered organisms have a history of safe use? Yes						
		reduce production of biological safety cabine		and aerosols?		
		n this project expose a ner protective measur		earch team to any risk explain.	s that might require	
				nazardous waste, bioh now disposal will be h		
<b>*</b>						

1284 Rel. #3

Thermol'orma

TOTAL P.04 E14 ROD R047 PAGE.04

August 27, 2003

mo Maass Chemistry

335b

22803-2121

# 9 Appendix B: Copyright Permission Form



US/ 44/ 4000 US: 64 INA COLUCTION

# **Biophysical Journal**Copyright Permission Form

In order to obtain copyright permission, please answer the questions below. When you have completed the form you may fax it to (301) 634-7267 or email it as an attachment to bi@biophysics.org. Once your request is processed, it will be sent back to you for your records.

Nume: BENEDICT HEBERT
Address: 3600 UNIVERSITY ST.
DONTHEM QC
HGE 3KR CANADA
Phone: (514) 965-1787
Fax: (574) 398-8434
Email: benedict-hobert @ mail. miglel.ca
I am requesting permission to reprint Figure(s) 13 4,56,7,8 by Banabict Habet (figure numbers) (author names)  SANTINDO SATINTINO, PAUL WILLIAM from the article SATIO-TEMPORAL HUGGE (title)
CONTECTATION SPECTROSCOPY (STICE) THEORY, WARFILMON, AND MILLIAMIN TO PROTEIN VELOCITY MAPPINE IN
in Biophys. J. 2005 86 5 3601-3614 I understand that I am obligated to Living the course (your) (vol.) (leave) (page numbers)
notify the original author(s) and will provide appropriate attribution to the Biophysical Society
and said author(s) for use of these materials.
OFFICE USE ONLY:
Permission granted Alisha Youm Date 5/24/06

## References

[1] B. Hebert, S. Costantino, and P. W. Wiseman. Spatiotemporal image correlation spectroscopy (stics) theory, verification, and application to protein velocity mapping in living cho cells. *Biophys. J.*, 88(5):3601–3614, 2005.

- [2] P. W. Wiseman, C. M. Brown, D. J. Webb, B. Hebert, N. L. Johnson, J. A. Squier, M. H. Ellisman, and A. F. Horwitz. Spatial mapping of integrin interactions and dynamics during cell migration by image correlation microscopy. *J Cell Sci*, 117(23):5521–5534, 2004.
- [3] D. A. Lauffenburger and A. F. Horwitz. Cell migration: a physically integrated molecular process. *Cell*, 84(3):359–69, 1996.
- [4] V.-M. Loitto, T. Forslund, T. Sundqvist, K.-E. Magnusson, and M. Gustafsson. Neutrophil leukocyte motility requires directed water influx. J Leukoc Biol, 71(2):212–222, 2002.
- [5] U. Euteneuer and M. Schliwa. Persistent, directional motility of cells and cytoplasmic fragments in the absence of microtubules. *Nature*, 310(5972):58, 1984.
- [6] H. P. Grimm, A. B. Verkhovsky, A. Mogilner, and J. J. Meister. Analysis of actin dynamics at the leading edge of crawling cells: implications for the shape of keratocyte lamellipodia. *European Biophysics Journal*, 32(6):563, 2003.
- [7] S. Costantino, J. W. D. Comeau, D. L. Kolin, and P. W. Wiseman. Accuracy and dynamic range of spatial image correlation and cross-correlation spectroscopy. *Biophys. J.*, 89(2):1251–1260, 2005.
- [8] A. J. Ridley, M. A. Schwartz, K. Burridge, R. A. Firtel, M. H. Ginsberg, G. Borisy, J. T. Parsons, and A. R. Horwitz. Cell migration: Integrating signals from front to back. *Science*, 302(5651):1704–1709, 2003.
- [9] K. M. Yamada and B. Geiger. Molecular interactions in cell adhesion complexes. *Curr Opin Cell Biol*, 9(1):76–85, 1997.

[10] D. A. Cheresh, J. Leng, and R. L. Klemke. Regulation of cell contraction and membrane ruffling by distinct signals in migratory cells. J. Cell Biol., 146(5):1107–1116, 1999.

- [11] T. D. Pollard. The cytoskeleton, cellular motility and the reductionist agenda. *Nature*, 422(6933):741, 2003.
- [12] A. Hall. Rho gtpases and the actin cytoskeleton. *Science*, 279(5350):509–514, 1998.
- [13] J. Thyberg and S. Moskalewski. Role of microtubules in the organization of the golgi complex. *Experimental Cell Research*, 246(2):263, 1999.
- [14] M. J. C. Hendrix, E. A. Seftor, Y.-W. Chu, K. T. Trevor, and R. E. B. Seftor. Role of intermediate filaments in migration, invasion and metastasis. *Cancer and Metastasis Reviews*, 15(4):507, 1996.
- [15] E. Nogales, S. Grayer Wolf, I. A. Khan, R. F. Luduena, and K. H. Downing. Structure of tubulin at 6.5 a and location of the taxol-binding site. *Nature*, 375(6530):424, 1995.
- [16] R. A. Milligan, M. Whittaker, and D. Safer. Molecular structure of f-actin and location of surface binding sites. *Nature*, 348(6298):217, 1990.
- [17] M. S. Kolodney and R. B. Wysolmerski. Isometric contraction by fibroblasts and endothelial cells in tissue culture: a quantitative study. J. Cell Biol., 117(1):73–82, 1992.
- [18] E. A. O'Toole. Extracellular matrix and keratinocyte migration. Clinical and Experimental Dermatology, 26(6):525–530, 2001.
- [19] M. Shimaoka, J. Takagi, and T. A. Springer. Conformational regulation of integrin structure and function. *Annual Review of Biophysics and Biomolecular Structure*, 31(1):485–516, 2002.
- [20] M. Vicente-Manzanares, D. J. Webb, and A. R. Horwitz. Cell migration at a glance. *J Cell Sci*, 118(21):4917–4919, 2005.

[21] D. J. Webb, K. Donais, L. A. Whitmore, S. M. Thomas, C. E. Turner, J. T. Parsons, and A. F. Horwitz. Fak-src signalling through paxillin, erk and mlck regulates adhesion disassembly. *Nat Cell Biol*, 6(2):154, 2004.

- [22] A. Huttenlocher, R. R. Sandborg, and A. F. Horwitz. Adhesion in cell migration. *Curr Opin Cell Biol*, 7(5):697–706, 1995.
- [23] S. J. Singer and G. L. Nicolson. The fluid mosaic model of the structure of cell membranes. *Science*, 175(4023):720–731, 1972.
- [24] B. N. G. Giepmans, S. R. Adams, M. H. Ellisman, and R. Y. Tsien. The fluorescent toolbox for assessing protein location and function. *Science*, 312(5771):217–224, 2006.
- [25] W. C. W. Chan, D. J. Maxwell, X. Gao, R. E. Bailey, M. Han, and S. Nie. Luminescent quantum dots for multiplexed biological detection and imaging. *Current Opinion in Biotechnology*, 13(1):40–46, 2002.
- [26] F. Yang, L. G. Moss, and G. N. J. Phillips. The molecular structure of green fluorescent protein. *Nature Biotechnology*, 14(1):1246 1251, 1996.
- [27] O. Shimomura, F. H. Johnson, and Y. Saiga. Extraction, purification and properties of aequorin, a bioluminescent protein from the luminous hydromedusan, aequorea. *J. Cell. Comp. Physiol.*, 59:223239, 1962.
- [28] M. Chalfie, T. Yuan, G. Euskirchen, W. W. Ward, and D. C. Prasher. Green fluorescent protein as a marker for gene expression. *Science*, 263(5148):802, 1994.
- [29] J. Zhang, R. E. Campbell, A. Y. Ting, and R. Y. Tsien. Creating new fluorescent probes for cell biology. *Nature Reviews Molecular Cell Biology*, 3(12):906–918, 2002.
- [30] P. L. Felgner, T. R. Gadek, M. Holm, R. Roman, H. W. Chan, M. Wenz, J. P. Northrop, G. M. Ringold, and M. Danielsen. Lipofection: A highly efficient, lipid-mediated dna-transfection procedure. *PNAS*, 84(21):7413-7417, 1987.

[31] S. T. Hess, E. D. Sheets, A. Wagenknecht-Wiesner, and A. A. Heikal. Quantitative analysis of the fluorescence properties of intrinsically fluorescent proteins in living cells. *Biophys. J.*, 85(4):2566–2580, 2003.

- [32] B. Bowen and N. Woodbury. Single-molecule fluorescence lifetime and anisotropy measurements of the red fluorescent protein, dsred, in solutionp. *Photochemistry and Photobiology*, 77(4):362–369, 2003.
- [33] R. Tsien and A. Waggoner. *Handbook of Confocal Fluorescence Microscopy*. Plenum Press, 1995.
- [34] M. E. Dickinson, G. Bearman, S. Tille, R. Lansford, and S. E. Fraser. Multi-spectral imaging and linear unmixing add a whole new dimension to laser scanning fluorescence microscopy. *Biotechniques*, 31(6):1274–1276, 2001.
- [35] X. Michalet, F. F. Pinaud, L. A. Bentolila, J. M. Tsay, S. Doose, J. J. Li, G. Sundaresan, A. M. Wu, S. S. Gambhir, and S. Weiss. Quantum dots for live cells, in vivo imaging, and diagnostics. *Science*, 307(5709):538–544, 2005.
- [36] M. A. Hines and P. Guyot-Sionnest. Synthesis and characterization of strongly luminescing zns-capped cdse nanocrystals. *Journal of Physical Chemistry*, 100(2):468–471, 1996.
- [37] B. O. Dabbousi, J. Rodriguez-Viejo, F. V. Mikulec, J. R. Heine, H. Mattoussi, R. Ober, K. F. Jensen, and M. G. Bawendi. (cdse)zns core-shell quantum dots: Synthesis and characterization of a size series of highly luminescent nanocrystallites. *Journal of Physical Chemistry* B, 101(46):9463–9475, 1997.
- [38] Jr. Bruchez, M., M. Moronne, P. Gin, S. Weiss, and A. P. Alivisatos. Semiconductor nanocrystals as fluorescent biological labels. *Science*, 281(5385):2013–2016, 1998.
- [39] T. D. Lacoste, X. Michalet, F. Pinaud, D. S. Chemla, A. P. Alivisatos, and S. Weiss. Ultrahigh-resolution multicolor colocalization of single fluorescent probes. *PNAS*, 97(17):9461–9466, 2000.

[40] M. Nirmal, B. O. Dabbousi, M. G. Bawendi, J. J. Macklin, J. K. Trautman, T. D. Harris, and L. E. Brus. Fluorescence intermittency in single cadmium selenide nanocrystals. *Nature*, 383(6603):802–804, 1996.

- [41] A. I. Bachir, N. Durisic, B. Hebert, P. Grutter, and P. W. Wiseman. Characterization of blinking dynamics in quantum dot ensembles using image correlation spectroscopy. *Journal of Applied Physics*, 99(6):064503, 2006.
- [42] B. Dubertret, P. Skourides, D. J. Norris, V. Noireaux, A. H. Brivanlou, and A. Libchaber. In vivo imaging of quantum dots encapsulated in phospholipid micelles. *Science*, 298(5599):1759–1762, 2002.
- [43] J. Wong, A. Chilkoti, and V. T. Moy. Direct force measurments of the biotin-streptavidin interaction. *Biomolecular Engineering*, 16:45–55, 1999.
- [44] E. P. Diamandis and T. K. Christopoulos. The biotin-(strept)avidin system: principles and applications in biotechnology. *Clin Chem*, 37(5):625–636, 1991.
- [45] I. Braslavsky, B. Hebert, E. Kartalov, and S. R. Quake. Sequence information can be obtained from single dna molecules. Proceedings of the National Academy of Sciences of the United States of America, 100(7):3960–3964, 2003.
- [46] C. Chamberlain and K. M. Hahn. Watching proteins in the wild: Fluorescence methods to study protein dynamics in living cells. *Traffic*, 1(10):755–762, 2000.
- [47] A. Kusumi, Y. Sako, and M. Yamamoto. Confined lateral diffusion of membrane receptors as studied by single particle tracking (nanovid microscopy) effects of calcium-induced differentiation in cultured epithelial cells. *Biophysical Journal*, 65(5):2021–2040, 1993.
- [48] M. Dahan, S. Levi, C. Luccardini, P. Rostaing, B. Riveau, and A. Triller. Diffusion dynamics of glycine receptors revealed by single-quantum dot tracking. *Science*, 302(5644):442–445, 2003.

[49] R. Yuste. Fluorescence microscopy today. Nat Meth, 2(12):902, 2005.

- [50] D. E. Koppel, F. Morgan, A. E. Cowan, and J. H. Carson. Scanning concentration correlation spectroscopy using the confocal laser microscope. *Biophysical Journal*, 66(2):502–507, 1994.
- [51] N. O. Petersen, P. L. Hddelius, P. W. Wiseman, O. Seger, and K. E. Magnusson. Quantitation of membrane receptor distributions by image correlation spectroscopy: concept and application. *Biophysical Journal*, 65(3):1135–46, 1993.
- [52] D. Gerlich, J. Beaudouin, M. Gebhard, J. Ellenberg, and R. Eils. Four-dimensional imaging and quantitative reconstruction to analyse complex spatiotemporal processes in live cells. *Nat Cell Biol*, 3(9):852, 2001.
- [53] D. E. Koppel, D. Axelrod, J. Schlessinger, E. L. Elson, and W. W. Webb. Dynamics of fluorescence marker concentration as a probe of mobility. *Biophysical Journal*, 16(11):1315–29, 1976.
- [54] T. Meyvis, S. De Smedt, P. Van Oostveldt, and J. Demeester. Fluorescence recovery after photobleaching: A versatile tool for mobility and interaction measurements in pharmaceutical research. *Pharmaceutical Research*, 16(8):1153, 1999.
- [55] E. B. Brown, E. S. Wu, W. Zipfel, and W. W. Webb. Measurement of molecular diffusion in solution by multiphoton fluorescence photobleaching recovery. *Biophys. J.*, 77(5):2837–2849, 1999.
- [56] M. J. Saxton and K. Jacobson. Single-particle tracking applications to membrane dynamics. Annual Review of Biophysics and Biomolecular Structure, 26:373–399, 1997.
- [57] M. J. Saxton. Single-particle tracking: models of directed transport. Biophys. J., 67(5):2110–2119, 1994.
- [58] H. Qian, M. P. Sheetz, and E. L. Elson. Single particle tracking. analysis of diffusion and flow in two-dimensional systems. *Biophysical Journal*, 60(4):910–21, 1991.

[59] C. Dietrich, B. Yang, T. Fujiwara, A. Kusumi, and K. Jacobson. Relationship of lipid rafts to transient confinement zones detected by single particle tracking. *Biophysical Journal*, 82(1):274–284, 2002.

- [60] B. K. P. Horn and B. G. Schunck. Determining optical flow. Artificial Intelligence, 17(1):185–203, 1981.
- [61] S. Das Peddada and R. McDevitt. Least average residual algorithm (lara) for tracking the motion of arctic sea ice. *IEEE Transactions on Geoscience and Remote Sensing*, 34(4):915–925, 1996.
- [62] J. J. Simpson and J. I. Gobat. Robust velocity estimates, stream functions, and simulated lagrangian drifters from sequential spacecraft data. *IEEE Transactions on Geoscience and Remote Sensing*, 32(3):479–493, 1994.
- [63] H. Nogawa, Y. Nakajima, Y. Sato, and S. Tamura. Acquisition of symbolic description from flow fields: A new approach based on a fluid model. *IEEE Transactions on Pattern Analysis and Machine Intelligence*, 19(1):58–63, 1997.
- [64] T. Corpetti, E. Memin, and P. Perez. Dense estimation of fluid flows. *IEEE Transactions on Pattern Analysis and Machine Intelligence*, 24(3), 2002.
- [65] R. P. Wildes, M. J. Amabile, A.-M. Lanzillotto, and T.-S. Leu. Recovering estimates of fluid flow from image sequence data. Computer Vision and Image Understanding, 80(1):246–266, 2000.
- [66] C. M. Waterman-Storer, A. Desai, J. Chloe Bulinski, and E. D. Salmon. Fluorescent speckle microscopy, a method to visualize the dynamics of protein assemblies in living cells. *Current Biology*, 8(22):1227, 1998.
- [67] P. Vallotton, A. Ponti, C. M. Waterman-Storer, E. D. Salmon, and G. Danuser. Recovery, visualization, and analysis of actin and tubulin polymer flow in live cells: A fluorescent speckle microscopy study. *Biophysical Journal*, 85(2):1289–1306, 2003.

[68] C. S. Peskin, G. M. Odell, and G. F. Oster. Cellular motions and thermal fluctuations: the brownian ratchet. *Biophys. J.*, 65(1):316–324, 1993.

- [69] A. Ponti, M. Machacek, S. L. Gupton, C. M. Waterman-Storer, and G. Danuser. Two distinct actin networks drive the protrusion of migrating cells. *Science*, 305(5691):1782–1786, 2004.
- [70] A. Ponti, A. Matov, M. Adams, S. Gupton, C. M. Waterman-Storer, and G. Danuser. Periodic patterns of actin turnover in lamellipodia and lamellae of migrating epithelial cells analyzed by quantitative fluorescent speckle microscopy. *Biophys. J.*, 89(5):3456–3469, 2005.
- [71] D. Magde, E. Elson, and W. W. Webb. Thermodynamic fluctuations in a reacting system: measurement by fluorescence correlation spectroscopy. *Physical Review Letters*, 29(11):705–8, 1972.
- [72] E. L. Elson and D. Magde. Fluorescence correlation spectroscopy. i. conceptual basis and theory. *Biopolymers*, 13(1):1–27, 1974.
- [73] E. L. Elson and W. W. Webb. Concentration correlation spectroscopy: a new biophysical probe based on occupation number fluctuations. *Annual Review of Biophysics and Bioengineering*, 4(00):311–34, 1975.
- [74] N. O. Petersen. Scanning fluorescence correlation spectroscopy. i. theory and simulation of aggregation measurements. *Biophysical Journal*, 49(4):809–15, 1986.
- [75] M. Miike, Y. Kurihara, H. Hashimoto, and K. Koga. Velocity-field measurement by pixel-based temporal mutual-correlation analysis of dynamic image. The transactions of the IECE of Japan, 69(8):877– 882, 1986.
- [76] K. M. Berland, P. T. So, and E. Gratton. Two-photon fluorescence correlation spectroscopy: method and application to the intracellular environment. *Biophysical Journal*, 68(2):694–701, 1995.

[77] K. M. Berland, P. T. C. So, Y. Chen, W. W. Mantulin, and E. Gratton. Scanning two-photon fluctuation correlation spectroscopy: particle counting measurements for detection of molecular aggregation. *Biophysical Journal*, 71(1):410–20, 1996.

- [78] B. Valeur. *Molecular Fluorescence: Principles and Applications*, volume 1. Wiley-VCH, 1 edition, 2001.
- [79] A. Jablonski. ber den mechanismus des photolumineszenz von farbstoffphosphoren. Zeitschrift fur Physik, 94(1):38–46, 1935.
- [80] M. Goeppert Mayer. Elementary processes with two-quantum transitions. *Ann. d. Physik*, 9(273), 1931.
- [81] N. PanchukVoloshina, R. P. Haugland, J. BishopStewart, M. K. Bhalgat, P. J. Millard, F. Mao, W.-Y. Leung, and R. P. Haugland. Alexa dyes, a series of new fluorescent dyes that yield exceptionally bright, photostable conjugates. J. Histochem. Cytochem., 47(9):1179–1188, 1999.
- [82] J. R. Swedlow and M. Platani. Live cell imaging using wide-field microscopy and deconvolution. *Cell Structure and Function*, 27(5):335–341, 2002.
- [83] M. Muller. *Introduction to Confocal Fluorescence Microscopy*, volume 1. Shaker Publishing, Maastricht, 2002.
- [84] G. J. Brakenhoff, P. Blom, and P. Barends. Confocal scanning light microscopy with high aperture lenses. *Journal of Microscopy (Oxford)*, 117(2):219–232, 1979.
- [85] M. Minsky. Memoir on inventing the confocal scanning microscope. *Scanning*, 10(1):128–138, 1988.
- [86] M. Born and E. Wolf. Principles of Optics (6th ed), volume 1. Pergamon Press, Oxford, 1980.
- [87] W. Denk, J. H. Strickler, and W. W. Webb. 2-photon laser scanning fluorescence microscopy. *Science*, 248(4951):73–76, 1990.

[88] D. Axelrod, T. P. Burghardt, and N. L. Thompson. Total internal reflection fluorescence. *Annual Review of Biophysics and Bioengineering*, 13(1):247–268, 1984.

- [89] B. Geiger, A. Bershadsky, R. Pankov, and K. M. Yamada. Transmembrane extracellular matrix-cytoskeleton crosstalk. *Nature Reviews Molecular Cell Biology*, 2(11):793–805, 2001.
- [90] R. D. Vale, T. Funatsu, D. W. Pierce, L. Romberg, Y. Harada, and T. Yanagida. Direct observation of single kinesin molecules moving along microtubules. *Nature*, 380(6573):451, 1996.
- [91] R. M. Dickson, D. J. Norris, Y.-L. Tzeng, and W. E. Moerner. Three-dimensional imaging of single molecules solvated in pores of poly(acrylamide) gels. *Science*, 274(5289):966–968, 1996.
- [92] T. Ha, A. Y. Ting, J. Liang, W. B. Caldwell, A. A. Deniz, D. S. Chemla, P. G. Schultz, and S. Weiss. Single-molecule fluorescence spectroscopy of enzyme conformational dynamics and cleavage mechanism. *Proc.* Natl. Acad. Sci. U. S. A., 96(3):893–898, 1999.
- [93] M. Tokunaga, K. Kitamura, K. Saito, A. H. Iwane, and T. Yanagida. Single molecule imaging of fluorophores and enzymatic reactions achieved by objective-type total internal reflection fluorescence microscopy. *Biochemical and Biophysical Research Communications*, 235(1):47–53, 1997.
- [94] M. F. Paige, E. J. Bierneld, and W. E. Moerner. A comparison of through-the-objective total internal reflection microscopy and epifluorescence microscopy for single-molecule fluorescence imaging. *Single Molecules*, 2(3):191–201, 2001.
- [95] W. P. Ambrose, P. M. Goodwin, and J. P. Nolan. Single-molecule detection with total internal reflection excitation: Comparing signal-to-background and total signals in different geometries. *Cytometry*, 36(3):224–231, 1999.

[96] R. Rigler, U. Mets, J. Widengren, and P. Kask. Fluorescence correlation spectroscopy with high count rate and low background: analysis of translational diffusion. *European Biophysics Journal*, 22(3):169–75, 1993.

- [97] P. W. Wiseman and N. O. Petersen. Image correlation spectroscopy. ii. optimization for ultrasensitive detection of preexisting platelet-derived growth factor-beta receptor oligomers on intact cells. *Biophysical Journal*, 76(2):963–77, 1999.
- [98] N. L. Thompson. Fluorescence correlation spectroscopy. In J. R. Lakowicz, editor, Topics in fluorescence spectroscopy, Volume 1: Techniques, volume 1, pages 337–78. Plenum Press, New York, 1991.
- [99] D. Magde, W. W. Webb, and E. L. Elson. Fluorescence correlation spectroscopy. iii. uniform translation and laminar flow. *Biopolymers*, 17:361–376, 1978.
- [100] C. M. Laukaitis, D. J. Webb, K. Donais, and A. F. Horwitz. Differential dynamics of alpha5 integrin, paxillin, and alpha-actinin during formation and disassembly of adhesions in migrating cells. J. Cell Biol., 153(7):1427–1440, 2001.
- [101] J. Kolega. Effects of mechanical tension on protrusive activity and microfilament and intermediate filament organization in an epidermal epithelium moving in culture. J. Cell Biol., 102(4):1400–1411, 1986.
- [102] M. N. Teruel, T. A. Blanpied, K. Shen, G. J. Augustine, and T. Meyer. A versatile microporation technique for the transfection of cultured cns neurons. *Journal of Neuroscience Methods*, 93(1):37, 1999.
- [103] P. Vallotton, G. Danuser, S. Bohnet, J. Meister, and A. B. Verkhovsky. Tracking retrograde flow in keratocytes: News from the front. *Mol Biol Cell*, 16(2):1223–1231, 2005.
- [104] B. Efron. Bootstrap methods: Another look at the jackknife. *The Annals of Statistics*, 7(1):1–26, 1979.

[105] J.-E. Shea and C. L. Brooks Iii. From folding theories to folding proteins: A review and assessment of simulation studies of protein folding and unfolding. *Annual Review of Physical Chemistry*, 52(1):499–535, 2001.

- [106] S. Iyengar. Computer Modeling and Simulations of Complex Biological Systems, volume 1. CRC-Press LLC, Boca Raton, 1 edition, 1998.
- [107] A. Wells. Egf receptor. The International Journal of Biochemistry and Cell Biology, 31(6):637, 1999.
- [108] M. Edidin, Y. Zagyansky, and T. J. Lardner. Measurement of membrane protein lateral diffusion in single cells. *Science*, 191(4226):466–468, 1976.
- [109] T. Mitchison and M. Kirschner. Cytoskeletal dynamics and nerve growth. *Neuron*, 1(9):761–772, 1988.
- [110] E. Crowley and A. F. Horwitz. Tyrosine phosphorylation and cytoskeletal tension regulate the release of fibroblast adhesions. *J. Cell Biol.*, 131(2):525–537, 1995.
- [111] S. P. Palecek, A. Huttenlocher, A. F. Horwitz, and D. A. Lauffenburger. Physical and biochemical regulation of integrin release during rear detachment of migrating cells. *J Cell Sci*, 111(7):929–40, 1998.
- [112] S. P. Palecek, C. E. Schmidt, D. A. Lauffenburger, and A. F. Horwitz. Integrin dynamics on the tail region of migrating fibroblasts. *J Cell Sci*, 109(5):941–52, 1996.
- [113] C. M. Regen and A. F. Horwitz. Dynamics of beta 1 integrin-mediated adhesive contacts in motile fibroblasts. *J Cell Biol.*, 119:1347–1359, 1992.
- [114] A. R. Horwitz and J. T. Parsons. Cell migration–movin' on. *Science*, 286(5442):1102–3, 1999.
- [115] K. Burridge and P. Mangeat. An interaction between vinculin and talin. *Nature*, 308(5961):744, 1984.

[116] A. Horwitz, K. Duggan, C. Buck, M. C. Beckerle, and K. Burridge. Interaction of plasma membrane fibronectin receptor with talin - a transmembrane linkage. *Nature*, 320(6062):531, 1986.

- [117] M. Sato, W. H. Schwarz, and T. D. Pollard. Dependence of the mechanical properties of actin/alpha-actinin gels on deformation rate. *Nature*, 325(6107):828, 1987.
- [118] A. M. Sydor, A. L. Su, F. S. Wang, A. Xu, and D. G. Jay. Talin and vinculin play distinct roles in filopodial motility in the neuronal growth cone. J. Cell Biol., 134(5):1197–1207, 1996.
- [119] C. Jurado, J. R. Haserick, and J. Lee. Slipping or gripping? fluorescent speckle microscopy in fish keratocytes reveals two different mechanisms for generating a retrograde flow of actin. *Mol Biol Cell*, 16(1):507–518, 2005.
- [120] G. Giannone, B. J. Dubin-Thaler, H.-G. Dobereiner, N. Kieffer, A. R. Bresnick, and M. P. Sheetz. Periodic lamellipodial contractions correlate with rearward actin waves. *Cell*, 116(3):431, 2004.
- [121] C.-H. Lin and P. Forscher. Growth cone advance is inversely proportional to retrograde f-actin flow. *Neuron*, 14:763–771, 1995.
- [122] P. Sampath and T. D. Pollard. Effects of cytochalasin, phalloidin and ph on the elongation of actin filaments. *Biochemistry*, 30(7):1973–1980, 1991.
- [123] A. F. Straight, A. Cheung, J. Limouze, I. Chen, N. J. Westwood, J. R. Sellers, and T. J. Mitchison. Dissecting temporal and spatial control of cytokinesis with a myosin ii inhibitor. *Science*, 299(5613):1743–1747, 2003.
- [124] B. Geiger and A. Bershadsky. Assembly and mechanosensory function of focal contacts. *Current Opinion in Cell Biology*, 13(5):584, 2001.
- [125] B. Geiger and A. Bershadsky. Exploring the neighborhood: Adhesion-coupled cell mechanosensors. *Cell*, 110(2):139, 2002.

[126] A. Nayal, D. J. Webb, and A. F. Horwitz. Talin: an emerging focal point of adhesion dynamics. *Current Opinion in Cell Biology*, 16(1):94, 2004.

- [127] G. Jiang, G. Giannone, D. R. Critchley, E. Fukumoto, and M. P. Sheetz. Two-piconewton slip bond between fibronectin and the cytoskeleton depends on talin. *Nature*, 424(6946):334, 2003.
- [128] D. A. Calderwood, R. Zent, R. Grant, D. J. G. Rees, R. O. Hynes, and M. H. Ginsberg. The talin head domain binds to integrin beta subunit cytoplasmic tails and regulates integrin activation. *J. Biol. Chem.*, 274(40):28071–28074, 1999.
- [129] V. Martel, C. Racaud-Sultan, S. Dupe, C. Marie, F. Paulhe, A. Galmiche, M. R. Block, and C. Albiges-Rizo. Conformation, localization, and integrin binding of talin depend on its interaction with phosphoinositides. *J. Biol. Chem.*, 276(24):21217–21227, 2001.
- [130] B. Ratnikov, C. Ptak, J. Han, J. Shabanowitz, D. F. Hunt, and M. H. Ginsberg. Talin phosphorylation sites mapped by mass spectrometry. J Cell Sci, 118(21r):4921–4923, 2005.
- [131] P. Roy, Z. Rajfur, P. Pomorski, and K. Jacobson. Microscope-based techniques to study cell adhesion and migration. *Nature Cell Biology*, 4(4):E91–6, 2002.
- [132] G. von Wichert, B. Haimovich, G.-S. Feng, and M. P. Sheetz. Force-dependent integrin-cytoskeleton linkage formation requires downregulation of focal complex dynamics by shp2. EMBO J., 22(19):5023–5035, 2003.
- [133] D. R. Critchley. Cytoskeletal proteins talin and vinculin in integrin-mediated adhesion. *Biochemical Society transactions*, 32(1):831–836, 2004.
- [134] J. J. Otto. Detection of vinculin-binding proteins with an 125i-vinculin gel overlay technique. *J. Cell Biol.*, 97(4):1283–1287, 1983.

[135] M. Kovacs, J. Toth, C. Hetenyi, A. Malnasi-Csizmadia, and J. R. Sellers. Mechanism of blebbistatin inhibition of myosin ii. *J. Biol. Chem.*, 279(34):35557–35563, 2004.

- [136] B. Ramamurthy, C. M. Yengo, A. F. Straight, T. J. Mitchison, and H. L. Sweeney. Kinetic mechanism of blebbistatin inhibition of nonmuscle myosin iib. *Biochemistry*, 43(46):14832–14839, 2004.
- [137] G. F. Oster and A. S. Perelson. The physics of cell motility. *Journal of Cell Science Supplement*, 8(1):35–54, 1987.
- [138] G. T. Charras, J. C. Yarrow, M. A. Horton, L. Mahadevan, and T. J. Mitchison. Non-equilibration of hydrostatic pressure in blebbing cells. *Nature*, 435(7040):365, 2005.
- [139] S. Saadoun, M. C. Papadopoulos, M. Hara-Chikuma, and A. S. Verkman. Impairment of angiogenesis and cell migration by targeted aquaporin-1 gene disruption. *Nature*, 434(7034):786, 2005.
- [140] D. Zicha, I. M. Dobbie, M. R. Holt, J. Monypenny, D. Y. H. Soong, C. Gray, and G. A. Dunn. Rapid actin transport during cell protrusion. *Science*, 300(5616):142–145, 2003.
- [141] R. D. Allen and N. S. Allen. Cytoplasmic streaming in amoeboid movement. *Annual Review of Biophysics and Bioengineering*, 7(1):469–495, 1978.
- [142] B. Ballou, B. C. Lagerholm, L. A. Ernst, M. P. Bruchez, and A. S. Waggoner. Noninvasive imaging of quantum dots in mice. *Bioconjugate Chem.*, 15(1):79–86, 2004.
- [143] M. T. Valentine, Z. E. Perlman, M. L. Gardel, J. H. Shin, P. Matsudaira, T. J. Mitchison, and D. A. Weitz. Colloid surface chemistry critically affects multiple particle tracking measurements of biomaterials. *Biophys. J.*, 86(6):4004–4014, 2004.
- [144] T. M. Svitkina and G. G. Borisy. Arp2/3 complex and actin depolymerizing factor/cofilin in dendritic organization and treadmilling of actin filament array in lamellipodia. *J. Cell Biol.*, 145(5):1009–1026, 1999.

[145] J. Lee and K. Jacobson. The composition and dynamics of cell-substratum adhesions in locomoting fish keratocytes. *Journal of Cell Science*, 110(22):2833–2844, 1997.

- [146] J. A. Theriot and T. J. Mitchison. Actin microfilament dynamics in locomoting cells. *Nature*, 352(6331):126, 1991.
- [147] I. L. Novak, B. M. Slepchenko, A. Mogilner, and L. Loew. Cooperativity between cell contractility and adhesion. *Physical Review Letters*, 93(26):268109, 2004.
- [148] S. Bohnet, R. Ananthakrishnan, A. Mogilner, J.-J. Meister, and A. B. Verkhovsky. Weak force stalls protrusion at the leading edge of the lamellipodium. *Biophys. J.*, 90(5):1810–1820, 2006.
- [149] A. Mogilner. On the edge: modeling protrusion. Current Opinion in Cell Biology, 18(1):32, 2006.
- [150] K. Olbrich, W. Rawicz, D. Needham, and E. Evans. Water permeability and mechanical strength of polyunsaturated lipid bilayers. *Biophys. J.*, 79(1):321–327, 2000.
- [151] K. Keren, B. Hebert, P. T. Yam, C. A. Wilson, P. W. Wiseman, A. Mogilner, and J. A. Theriot. Intracellular fluid flow in rapidly moving cells. unpublished.